

Investigating the Evolution of Surface Features on Saturn's Moon Titan

LAUREN SCHURMEIER

B.S., University of California Santa Cruz, 2011

THESIS

Submitted as partial fulfillment of the requirements
for the degree of Doctor of Philosophy in Earth and Environmental Sciences in the
Graduate College of the University of Illinois at Chicago, 2018
Chicago, Illinois

Defense Committee:

Andrew Dombard (Chair and Advisor, Earth and Environmental Sciences, UIC)

Roy Plotnick (Earth and Environmental Sciences, UIC)

Jani Radebaugh (Department Geological Sciences, Brigham Young University)

Stefany Sit (Earth and Environmental Sciences, UIC)

Carol Stein (Earth and Environmental Sciences, UIC)

DEDICATION

This work is dedicated to all my loved ones who helped me grow into a scientist but didn't get to live to see this day.

To my mother, Jessie Lucas-Acosta, who bought me every space-related book, cheered me on in every competition, and always believed in me the most.

To my grandfather, Harris "Bud" Schurmeier, who got us to the Moon and then well past Neptune, and has always inspired me to do more.

To my father, Alan Schurmeier, for encouraging my creativity.

To my grandmother Bettye Jo Schurmeier, for raising such a strong and loving family.

To my stepfather Tony Acosta, who could always be counted on for his silliness and support.

ACKNOWLEDGEMENTS

This work would not have been possible without the help of Andrew Dombard, my mentor and advisor. I want to thank Andrew for always being a source of knowledge, encouragement and positivity, and for helping me go further and farther.

I also want to thank:

Jack Kolpin for his endless support and love.

My brother, Brenden, the nicest person I know.

Saman Karimi and Jon Kay, for teaching me so much.

Illinois Space Grand Consortium, for funding my life's passion.

Dr. Steve Hauck for sharing access to his server at Case Western Reserve University.

Stefany Sit, my mentor and friend, for taking me under her wing, trusting me, and inspiring confidence in myself.

Jani, Roy, Carol, and Kathy for their guidance and advice throughout this process.

Finally, all of my family and friends for patiently listening to my endless ramblings about planets and rocks. I hope they know that I am just getting started.

CONTRIBUTIONS OF AUTHORS

As part of this work, I have prepared chapters II, III, and IV to represent manuscripts that I am the primary author of and have done the modeling, mapping, and analysis. Chapter II has been published in the journal *Icarus* in 2017, and chapters III and IV have been formatted in preparation for submission in the journal *Icarus*. Dr. Andrew Dombard mentored me through this process of research and contributed to all three manuscripts. Dr. Jani Radebaugh (Brigham Young University) aided in the interpretation of results for chapters III and IV and will be a coauthor on the two future manuscripts. Dr. Michael Malaska (NASA - Jet Propulsion Laboratory) aided in the interpretation of remotely sensed NASA datasets for chapter IV and will be a coauthor on the future manuscript.

TABLE OF CONTENTS

CHAPTER	PAGE
DEDICATION	ii
ACKNOWLEDGMENTS	iii
CONTRIBUTIONS OF AUTHORS.....	iv
TABLE OF CONTENTS	v
LIST OF FIGURES	vii
LIST OF TABLES	iv
SUMMARY	x
LIST OF ABBREVIATIONS AND NOMENCLATURE	xiii
 I. INTRODUCTION	 1
A. Introduction	1
B. Works Cited	5
 II. CRATER RELAXATION ON TITAN AIDED BY LOW THERMAL CONDUCTIVITY	 7
A. Abstract	8
B. Introduction	9
1. Background	9
2. What Could Make Titan's Craters Shallow?	14
C. Estimating the Thermal Conductivity of Titan	19
D. Methods	22
1. Dune Field Effective Surface Temperature Simulation	23
2. Crater Relaxation Simulation with the Aid of Aeolian Infill	25
E. Results	32
F. Discussion	38
G. Conclusions	44
H. Works Cited	46
 III. INVESTIGATING THE SUPPORT OF TITAN'S LARGE MOUNTAIN PLATEAUS BY AIRY ISOSTASY	 51
A. Abstract	52
B. Introduction	54
C. Methods	58
1. Airy Isostasy Finite Element Modeling	61
D. Results	66
E. Discussion	72
F. Conclusions	80
G. Works Cited	82

IV. AN INTRUSIVE ORIGIN FOR RADIAL LABYRINTH TERRAINS ON TITAN IMPLIES A WATER-ICE RICH CRUST	85
A. Abstract	86
B. Introduction	88
C. Observations of Labyrinths.....	92
1. Description of the Labyrinths	94
2. Measurements.....	100
D. Models of Formation and Mechanics.....	101
1. Diapiric Upwelling	102
2. Intrusive Cryovolcanism	103
E. Discussion	110
F. Conclusions	114
G. Works Cited.....	116
V. APPENDICES	120
A. Chapter II: thermal file example for crater relaxation	120
B. Chapter II: mechanical file example for crater relaxation	128
C. Chapter II: example subroutine file for crater relaxation	136
D. Chapter III: mountain shape approximation as a Gaussian.....	140
E. Chapter III: Data comparing the actual mountain root and an isostatic root	141
F. Chapter III: example mountain subroutine file of water ice	142
G. Chapter III: thermal file example 1 layer mountain	146
H. Chapter III: mechanical file example 1 layer mountain.....	153
I. Chapter III: thermal file example 2 layer mountain	160
J. Chapter III: mechanical file example 2 layer mountain.....	166
K. Chapter III: example mountain subroutine file of methane clathrate hydrate.....	172
L. Chapter IV: domed Labyrinth measurements (diameter and spacing)	176
M. Chapter IV: lithospheric strength envelope equations.....	177
N. Statements about permission to reprint the previously published chapter II.....	177
VI. Curriculum Vitae	179

LIST OF FIGURES

CHAPTER	PAGE
CHAPTER I	
1. Scaled size comparison of Titan, Earth, and the Moon	2
CHAPTER II	
1. Depth/Diameter plot of fresh craters with diameters over 25 km on Callisto and Ganymede from Schenk (2002). Titan's craters are the labeled circles	11
2. Locations of Titan's craters	15
3. Cassini SAR images of Soi, Afekan, Sinlap, and dune-filled probable craters.....	17
4. Example dune field simulation with the final temperature values.....	24
5. Schematic of the modeled crater filled with dunes (and their thermal effects).....	28
6. Example of a volume calculation to find the time in which relaxation is complete.....	30
7. Results of crater relaxation times for different relative volumes of sand infill	34
8. Crater Relaxation times for different volumes of sand infill using three grain sizes....	37
CHAPTER III	
1. Interpolated topographic map of Titan with four labeled topographic rises	55
2. Three end-member forms of large-scale topographic support	55
3. SAR images of the mountain plateaus at locations A and D	59
4. Schematic showing the modeled Airy isostatic mountain.....	62
5. Viscoelastic evolution of the pleateaus at two heat flows (4 and 6.6 mW m ⁻²) and an initial height of 600 m	67
6. Comparison of the simulated root topography and the ideal profiles of a root in isostatic equilibrium with the surface topography at two heat flows	67
7. Viscoelastic evolution of the pleateaus at two heat flows (4 and 6.6 m W m ⁻²) and an initial height of 1 km	69
8. Normalized comparison of simulations with initial surface heights of 600 m and 1 km for the 200 km wide pleateau at 4 mW m ⁻²	69
9. A comparison of the viscoelastic evolution of the two pleateaus with and without bouyant support for two heat flows	70
10. Comparison of the evolution of the 200 km plateau in an water ice mesh, a methane clathrate hydrate mesh, and an water ice mesh with an increased surface temperature of 110 K	71
11. Profile of differential stress at depth over time under the simulated 350 km wide plateau at 4 mW m ⁻²	73
12. A SAR image of a possible third large mountain plateau	76
13. Possible evidence of a cryovolcanic caledar and flow at loaction D	78

LIST OF FIGURES (CONTINUED)

CHAPTER IV

1. SAR image of the region of interest and locations of the domed Labyrinths	93
2. Radial Labyrinth terrain Anbus (feature A) and SARTopo topographic profiles.....	95
3. Center SAR image of features C-F	96
4. SAR image of features G and H.....	99
5. Uplift and formation sequence of radial Labyrinth terrains.....	104
6. Schematic of a lithospheric strength envelope used to find the BDT (brittle-ductile transistion) of a planetary ice shell.....	106
7. Titan's lithospheric strength envelope	109

LIST OF TABLES

CHAPTER	PAGE
CHAPTER II	
1. Crater locations, and actual and modeled dimensions.	12

SUMMARY

With its rugged topography, sand seas of linear dunes, impact craters, and other exogenic processes, including aeolian, lacustrine, and fluvial, Saturn's moon Titan is thought to be more similar to our planet Earth than many other planets or icy satellites. It is unclear, however, if Titan's surface is also shaped by endogenic processes, such as: cryovolcanism (water/ice volcanism), viscous relaxation, tectonism, and diapirism. I study the evolution of three specific types of surface features to understand better the relative importance of endogenic and exogenic processes in shaping the Titan that we see today.

First, I investigate why Titan's existing impact craters are anomalously shallow and mainly found in the dry equatorial region filled with sand seas. Compared to similar-sized icy satellites, Titan's craters are anomalously shallow. I test whether Titan's equatorial craters can be shallowed by topographic relaxation using the Marc Mentat finite element package. I find that the craters cannot relax under normal conditions, but will relax when filled with large amounts of low thermal conductivity sand from nearby sand seas. Thus, the equatorial craters on Titan are shallow due to a combination of endogenic and exogenic processes. I hypothesize that craters are not found outside the equatorial sand seas, because at higher latitudes the craters experience a greater degree of erosion from methane rain, an exogenic process.

Second, I investigate how the several large, organic-rich mountainous plateaus (a type of Labyrinth terrain) are supported and formed on Titan. All large-scale topographic features require a mechanism of support. On Earth, large mountains are supported by Airy isostasy.

On Titan, the roots of mountains would need to be very large to provide buoyant support because of the small density contrast between the outer ice shell and the subsurface ocean. I model the long-term viscoelastic evolution of the mountain plateaus and mountain roots using the finite element method. I find that they cannot be supported by Airy isostasy, nor formed through crustal thickening (tectonics), because the lower portions of the ice shell and root are too warm and weak to transfer significant support to the surface. Instead, to build these would require either a lower density material intruded into the surrounding lithosphere (i.e., Pratt isostasy), or the mountain load was placed on the lithosphere, both of which could form through cryovolcanism (an endogenic process). Additionally, I identify putative morphological evidence for extrusive cryovolcanism at one plateau location.

Third, I investigate how the medium-sized, organic-rich, dome-shaped topography (Labyrinth terrains) formed. These features are circular, topographically elevated, clustered, and significantly more eroded than the surrounding terrains (Undifferentiated Plains). Morphologically, they appear to be uplifted Undifferentiated Plains, and have been hypothesized to have formed through either diapirism or intrusive cryovolcanism (endogenic processes). I use scaling relationships based on diapirs and intrusive volcanic laccoliths on other planetary bodies to choose the most plausible formation mechanism. I find that their size and spacing is not consistent with diapirism, but is consistent with an intrusive cryovolcanic laccolith forming at the base of Titan's lithosphere. I create a suite of lithospheric strength envelopes and find that the intrusion depth predicted based on the scale of the Labyrinths matches the expected brittle-ductile transition for Titan's ice shell when composed of water ice, not methane clathrate.

Overall, I find that these three types of surface features indicate that both exogenic and endogenic processes are important contributors to shaping the Titan that we see today, and that cryovolcanism may be more prevalent on Titan than previously thought.

LIST OF ABBREVIATIONS AND NOMENCLATURE

Aeolian	of or caused by the wind.
BDT	Brittle - Ductile Transition. The transition depth at which rocks change from brittle to ductile behavior in a planetary interior.
Clathrate Hydrate	a compound in which molecules of one component (a gas, such as methane) are physically trapped within the crystal structure of another (water ice).
Cryovolcanism	volcano that erupts volatiles such as water, ammonia or methane instead of molten rock.
Diapir	a domed rock formation in which a core of rock has moved upward to pierce the overlying strata.
Endogenic	formed or occurring beneath the surface of a planetary body.
Exogenic	formed or occurring at or above a surface of a planetary body.
Extrusive	relating to or denoting rock that has been extruded at the Earth's surface as lava or other volcanic deposits.
Fluvial	of or found in a river.
Intrusive	igneous rock formed from magma forced into older rocks at depths within the Earth's crust, which then slowly solidifies below the Earth's surface.
Isostasy	a general equilibrium of the forces tending to elevate or depress a planet's lithosphere.
Labyrinth Terrain	a geomorphic unit on Titan characterized as highly dissected plateaus and remnant ridges with a high relative valley density, medium to low radar backscatter in Cassini SAR data, and a radar emissivity that suggests that it is organic-rich.
Lacustrine	relating to or associated with lakes.
Laccolith	a mass of igneous rock, typically lens-shaped, that has been intruded between rock strata causing uplift in the shape of a dome.

Lithosphere	the rigid outer layer of a planetary body.
Organic Molecules	are molecules usually composed of carbon atoms in rings or long chains, to which are attached other atoms of such elements as hydrogen, oxygen, and nitrogen.
Photochemical Reaction	a chemical reaction caused by absorption of light.
Radarclinometry	technique for estimating heights of landforms in SAR images.
SAR	Synthetic Aperture RADAR
SARTopo	topography data estimated from overlapping Cassini SAR image swaths.
Sill	a generally tabular sheet of igneous rock intruded between and parallel with the existing strata.
Tholin	heteropolymer molecules formed by solar ultraviolet irradiation of simple organic compounds such as methane or ethane, often in combination with nitrogen.
Undifferentiated Plains	a geomorphic unit on Titan characterized as relatively featureless expanses of terrains on Titan that appear radar-dark and fairly uniform in Cassini SAR data, and are thought to be organic rich sedimentary plains.
Viscoelastic	materials that exhibit both viscous and elastic characteristics when undergoing deformation.

CHAPTER I

I. INTRODUCTION

Titan is in many ways the most similar planetary body to Earth. Titan is the largest moon of Saturn, slightly larger than the planet Mercury, and about 1.4x the size of our Moon (Fig. 1). Saturn orbits over 9.5 times the distance between the Earth and the Sun, and therefore the surface of Titan is quite cold (94 K average surface temperature). At this low temperature, its volatile-rich outer portions are capped by a thick crust (~100 km) that is composed mainly of water ice, or methane clathrate hydrate (in contrast to the silicate crust capping terrestrial worlds) and likely overlies a liquid water ocean (Sohl, 2003). In stark contrast to the airless surfaces of all other moons and small bodies in the solar system, Titan's surface is covered by a thick, hazy atmosphere and is dominated by more diverse processes, like the Earth.

Indeed, Titan's most striking feature is its massive orange atmosphere (Fig. 1). The atmosphere is similar to the Earth in composition (mainly of nitrogen but with a few percent methane) and size (Titan's is ~1.2x more massive). The orange color arises from photochemical reactions between nitrogen and methane that result in the production of a plethora of organic molecules of varying complexity, termed "tholins" (Khare et al., 1984), that form orange haze layers opaque to visible light. The hazes veil a world filled with vast sand seas of thousands of long, linear dunes (Lorenz et al., 2006; Radebaugh, 2013), mountainous regions of varying size, composition, and morphology (Cook-Hallett et al., 2015; Liu et al., 2016a; Lorenz et al., 2013; Mitri et al., 2010; Radebaugh et al., 2007), clouds

that precipitate liquid methane (Turtle et al., 2011), river channels (Burr et al., 2013), lakes and seas of liquid methane and ethane in the polar regions (Stofan et al., 2007), sparse and curiously shallow impact craters (Neish et al., 2013), and possibly even cryovolcanoes, or volcanoes made of erupted water (Lopes et al., 2013).

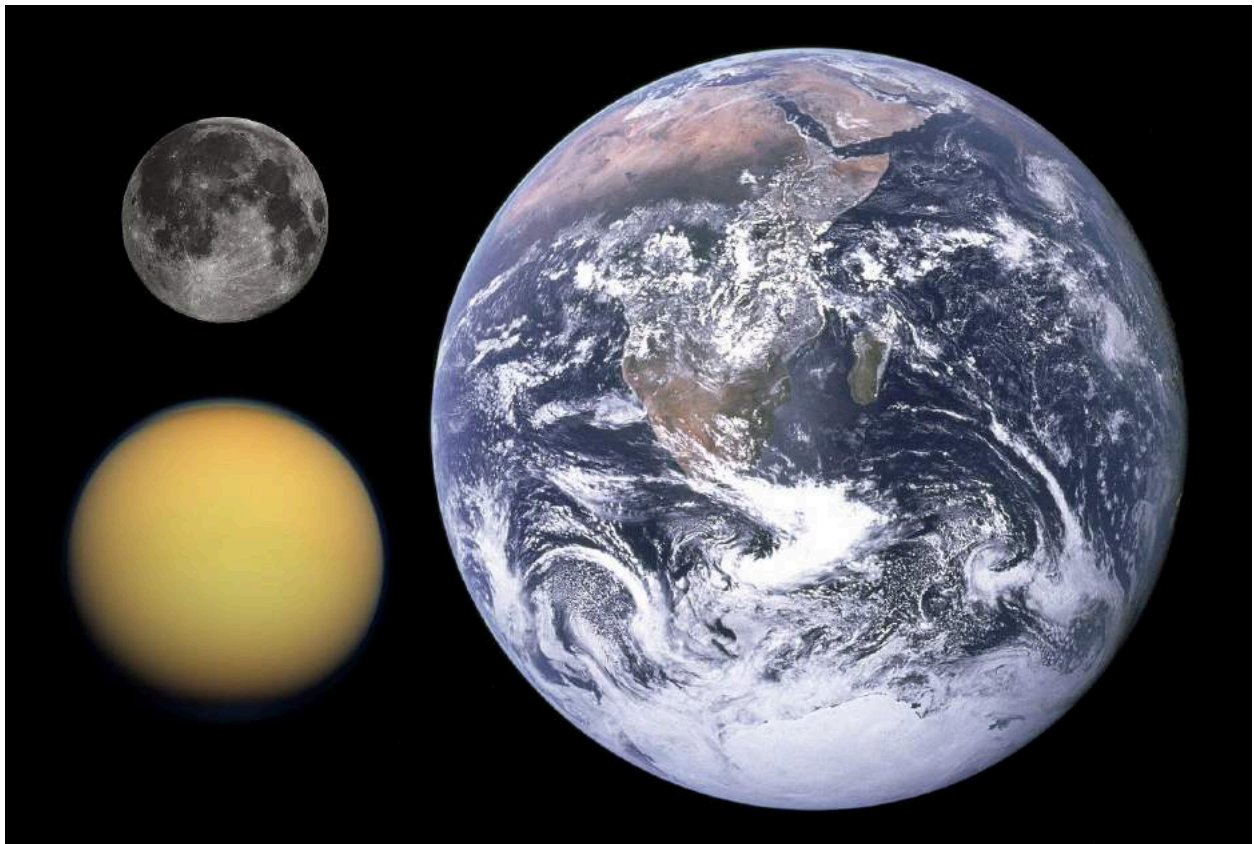


Figure 1: Scaled size comparison of Titan (bottom left), Earth (left) and the Moon (top left). Note the opaque orange color of Titan's atmosphere. Image is publicly available from Wikipedia commons, mosaicking the following images: Apollo 17 Picture of the Whole Earth (Source NASA), telescopic image of the full Moon (source: Gregory H. Revera), and the image of Titan (source: NASA/JPL/Space Science Institute).

The presence of many of these features, including but not limited to: the variety of mountain types, the atmospheric haze that must be replenished (due to its photochemical removal), and the lack of craters in general suggest that many processes are at work changing Titan's surface through time. Current debate within Titan research asks, is Titan shaped by both endogenic processes (cryovolcanism, tectonics, diapirism, topographic relaxation) and exogenic processes (impact craters, aeolian, and hydrological processes) like the Earth, or is Titan unique in the solar system for being an internally quiescent world shaped mainly by extraterrestrial (impacts), atmospheric, and fluvial processes (Lopes et al., 2013; Moore et al., 2014; Moore and Pappalardo, 2011)?

I study the evolution of specific surface features on Titan to understand better the relative importance of endogenic and exogenic processes in shaping the Titan that we see today. First, I investigate why Titan's existing impact craters are anomalously shallow using finite element modeling. Second, I investigate how several large mountainous plateaus are supported and formed on Titan, again using finite element modeling. Third, I investigate how the medium-size, organic-rich, dome-shaped topography (Labyrinth terrains) formed. All three projects are interrelated. The impact craters may be removed due to aeolian sand infill or fluvial erosion (both exogenic process), topographic relaxation (an endogenic process), or some combination. In addition, the large, isolated mountainous plateaus on Titan require a mechanism of support (either buoyancy, lithospheric strength, or some combination). I determine the relative importance of these modes and attempt to tie these results to an assessment of the formation mechanisms of these mountains. Finally, understanding the cause of the uplift of the dome-shaped Labyrinth Terrains clustered in the northern mid-

latitudes provides insight into a unique region of Titan that could be sedimentary, diapiric, or cryovolcanic, again telling us the importance and timing of endogenic and exogenic processes on Titan. Together, these projects will help improve our understanding of the complex history of Titan.

A. Works Cited

- Burr, D.M., Taylor Perron, J., Lamb, M.P., Irwin, R.P., Collins, G.C., Howard, A.D., Sklar, L.S., Moore, J.M., Ádámkovics, M., Baker, V.R., Drummond, S. a., Black, B. a., 2013. Fluvial features on Titan: Insights from morphology and modeling. *Bull. Geol. Soc. Am.* 125, 299-321. doi:10.1130/B30612.1
- Cook-Hallett, C., Barnes, J.W., Kattenhorn, S.A., Hurford, T., Radebaugh, J., Stiles, B., Beuthe, M., 2015. Global contraction/expansion and polar lithospheric thinning on Titan from patterns of tectonism. *J. Geophys. Res. E Planets* 120, 1220-1236. doi:10.1002/2014JE004645
- Khare, B.N., Sagan, C., Thompson, W.R., Arakawa, E.T., Suits, F., Callcott, T. a, Williams, M.W., Shrader, S., Ogino, H., Willingham, T.O., Nagy, B., 1984. The organic aerosols of Titan. *Adv. Space Res.* 4, 59-68. doi:10.1016/0273-1177(84)90545-3
- Liu, Z.Y.C., Radebaugh, J., Harris, R. a., Christiansen, E.H., Neish, C.D., Kirk, R.L., Lorenz, R.D., 2016. The tectonics of Titan: Global structural mapping from Cassini RADAR. *Icarus* 270, 14-29. doi:10.1016/j.icarus.2015.11.021
- Lopes, R.M.C., Kirk, R.L., Mitchell, K.L., Legall, a., Barnes, J.W., Hayes, a., Kargel, J., Wye, L., Radebaugh, J., Stofan, E.R., Janssen, M. a., Neish, C.D., Wall, S.D., Wood, C. a., Lunine, J.I., Malaska, M.J., 2013. Cryovolcanism on Titan: New results from Cassini RADAR and VIMS. *J. Geophys. Res. E Planets* 118, 416-435. doi:10.1002/jgre.20062
- Lorenz, R.D., Stiles, B.W., Aharonson, O., Lucas, A., Hayes, A.G., Kirk, R.L., Zebker, H. a., Turtle, E.P., Neish, C.D., Stofan, E.R., Barnes, J.W., 2013. A global topographic map of Titan. *Icarus* 225, 367-377. doi:10.1016/j.icarus.2013.04.002
- Lorenz, R.D., Wall, S., Radebaugh, J., Boubin, G., Reffet, E., Janssen, M., Stofan, E., Lopes, R., Kirk, R., Elachi, C., Lunine, J., Mitchell, K., Paganelli, F., Soderblom, L., Wood, C., Wye, L., Zebker, H., Anderson, Y., Ostro, S., Allison, M., Boehmer, R., Callahan, P., Encrenaz, P., Ori, G.G., Francescetti, G., Gim, Y., Hamilton, G., Hensley, S., Johnson, W., Kelleher, K., Muhleman, D., Picardi, G., Posa, F., Roth, L., Seu, R., Shaffer, S., Stiles, B., Vetrella, S., Flamini, E., West, R., 2006. The sand seas of Titan: Cassini RADAR observations of longitudinal dunes. *Science* 312, 724-727. doi:10.1126/science.1123257
- Mitri, G., Bland, M.T., Showman, A.P., Radebaugh, J., Stiles, B., Lopes, R.M.C., Lunine, J.I., Pappalardo, R.T., 2010. Mountains on Titan: Modeling and observations. *J. Geophys. Res. E Planets* 115, 1-15. doi:10.1029/2010JE003592
- Moore, J.M., Howard, A.D., Morgan, A.M., Howard, A.D., Morgan, A.M., 2014. *Journal of Geophysical Research : Planets to its climate evolution* 1-18. doi:10.1002/2014JE004608.Received

- Moore, J.M., Pappalardo, R.T., 2011. Titan: An exogenic world? *Icarus* 212, 790-806.
doi:10.1016/j.icarus.2011.01.019
- Neish, C.D., Kirk, R.L., Lorenz, R.D., Bray, V.J., Schenk, P., Stiles, B.W., Turtle, E., Mitchell, K., Hayes, a., 2013. Crater topography on Titan: Implications for landscape evolution. *Icarus* 223, 82-90. doi:10.1016/j.icarus.2012.11.030
- Radebaugh, J., 2013. Dunes on Saturn's moon Titan as revealed by the Cassini Mission. *Aeolian Res.* 11, 23-41. doi:10.1016/j.aeolia.2013.07.001
- Radebaugh, J., Lopes, R.M.C., Lunine, J.I., Kirk, R.L., Wall, S.D., Stofan, E.R., Lorenz, R.D., 2007. Mountains on Titan observed by Cassini Radar. *Icarus* 192, 77-91.
doi:10.1016/j.icarus.2007.06.020
- Sohl, F., 2003. Interior structure models and tidal Love numbers of Titan. *J. Geophys. Res.* 108, 1-13. doi:10.1029/2003JE002044
- Stofan, E.R., Elachi, C., Lunine, J.I., Lorenz, R.D., Stiles, B., Mitchell, K.L., Ostro, S., Soderblom, L., Wood, C., Zebker, H., Wall, S., Janssen, M., Kirk, R., Lopes, R., Paganelli, F., Radebaugh, J., Wye, L., Anderson, Y., Allison, M., Boehmer, R., Callahan, P., Encrenaz, P., Flamini, E., Francescetti, G., Gim, Y., Hamilton, G., Hensley, S., Johnson, W.T.K., Kelleher, K., Muhleman, D., Paillou, P., Picardi, G., Posa, F., Roth, L., Seu, R., Shaffer, S., Vetrella, S., West, R., 2007. The lakes of Titan. *Nature* 445, 61-64. doi:10.1038/nature05438
- Turtle, E.P., Perry, J.E., Hayes, a G., Lorenz, R.D., Barnes, J.W., McEwen, a S., West, R. a, Del Genio, a D., Barbara, J.M., Lunine, J.I., Schaller, E.L., Ray, T.L., Lopes, R.M.C., Stofan, E.R., 2011. Rapid and extensive surface changes near Titan's equator: evidence of April showers. *Science* 331, 1414-1417. doi:10.1126/science.1201063

CHAPTER II

CRATER RELAXATION ON TITAN AIDED BY LOW

THERMAL CONDUCTIVITY SAND INFILL

Chapter II has been published in the journal Icarus as:

Crater Relaxation on Titan Aided by Low Thermal Conductivity Sand Infill
Lauren R. Schurmeier, Andrew J. Dombard

Department of Earth and Environmental Sciences, University of Illinois at Chicago, 845 W.
Taylor St., Chicago, IL, United States

Icarus 305 (2018) 314-323

Received 24 May 2017; accepted 26 October 2017; available online 8 November 2017

A. Abstract

Titan's few impact craters are currently many hundreds of meters shallower than the depths expected. Assuming these craters initially had depths equal to that of similar-sized fresh craters on Ganymede and Callisto (moons of similar size, composition, and target lithology), then some process has shallowed them over time. Since nearly all of Titan's recognized craters are located within the arid equatorial sand seas of organic-rich dunes, where rain is infrequent, and atmospheric sedimentation is expected to be low, it has been suggested that aeolian infill plays a major role in shallowing the craters. Topographic relaxation at Titan's current heat flow was previously assumed to be an unimportant process on Titan due to its low surface temperature (94 K). However, our estimate of the thermal conductivity of Titan's organic-rich sand is remarkably low ($0.025 \text{ W m}^{-1} \text{ K}^{-1}$), and when in thick deposits, will result in a thermal blanketing effect that can aid relaxation. Here, we simulate the relaxation of Titan's craters Afekan, Soi, and Sinlap including thermal effects of various amounts of sand inside and around Titan's craters. We find that the combination of aeolian infill and subsequent relaxation can produce the current crater depths in a geologically reasonable period of time using Titan's current heat flow. Instead of needing to fill completely the missing volume with 100% sand, only ~62%, ~71%, and ~97%, of the volume need be sand at the current basal heat flux for Afekan, Soi, and Sinlap, respectively. We conclude that both processes are likely at work shallowing these craters, and this finding contributes to why Titan overall lacks impact craters in the arid equatorial regions.

B. Introduction

1. Background

Unlike most moons in our solar system, Saturn's moon Titan has very few impact craters identified on its surface. Only a few hundred crater candidates have been identified on Titan, of which only 11 have been officially recognized and named as craters (Buratti et al., 2012; Lorenz et al., 2007; Neish et al., 2013; Neish and Lorenz, 2012; Wood et al., 2010). Since impact cratering is among the most common geologic processes in the solar system, the number of impact craters on a planetary body can be used to indicate the relative extent of surface modification that it experienced. Surfaces dominated by impact craters are likely little modified, ancient surfaces, while low crater counts, such as on Titan, suggest that significant modification has occurred to remove craters. Indeed, Titan has many signs of surface modification processes: fluvial features with various morphologies are found across the globe (Burr et al., 2013; Langhans et al., 2012), there are hundreds of lakes and a few large seas that are constrained to the polar regions (Stofan et al., 2007; Lorenz et al., 2014), many mountains and mountain chains have been identified (Liu et al., 2016a; Radebaugh et al., 2007), the photochemically produced atmospheric haze of organic molecules continually snows to the surface (Tomasko et al., 2005), and there are vast sand seas of thousands of kilometers long linear dunes in the equatorial region (Lorenz et al., 2006; Radebaugh, 2013; Savage et al., 2014).

Aside from being surprisingly crater-poor, Titan's surface is also abnormal in that the identified craters are hundreds of meters shallower than expected. Neish et al. (2013) used

SARTopo (Synthetic Aperture RADAR-derived Topography; see Stiles et al., 2009) data to create topographic profiles of the named craters Ksa, Momoy, Sinlap, Soi, Hano, Afekan, Menrva, and two “probable” unnamed craters identified by Wood et al. (2010). Soi and the two probable craters did not have topographic profiles that resembled impact craters despite their morphological similarity to impact craters in SAR imagery. They might not be craters or may have had their topographies completely obliterated by some process or combination of processes (see Introduction Part B). For the rest, Neish et al. (2013) measured the crater depths using the SARTopo topographic profiles for all of the craters except for Momoy, for which they used autostereo where the depths are estimated by comparing the foreshortening of the near and far walls, assuming a perfectly symmetric profile across the crater.

The depths of these craters (Fig. 1) are significantly shallower when compared to similar-sized fresh craters on Ganymede and Callisto (Schenk 2002). This observation is surprising because Ganymede and Callisto have a similar target rock (water ice) and gravitational acceleration (T: 1.35 m s^{-2} , G: 1.4 m s^{-2} , C: 1.3 m s^{-2}), and reasonably similar average impact velocities to Titan (T: 10.5 km s^{-1} , G: 20 km s^{-1} , C: 15 km s^{-1}), so impact crater morphology on all three bodies is expected to be very similar. Instead, Titan’s craters are shallowed by many hundreds of meters compared to their expected depths, which we define as the average of the depths expected for similar-size craters on Ganymede and Callisto (Schenk 2002) (see Table 1).

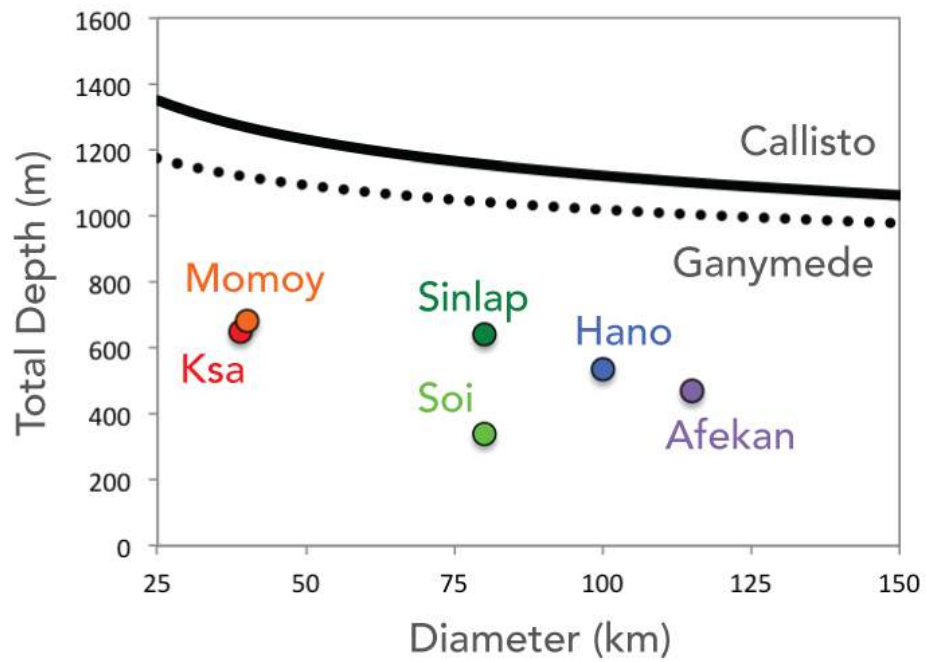


Figure 1: Depth/Diameter plot of fresh craters with diameters over 25 km on Callisto and Ganymede from Schenk (2002). Titan's craters are the labeled circles.

Table 1: Crater locations, and actual and modeled dimensions.

Crater	Latitude (°N), Longitude (°W)	Diameter Measured (km)	Diameter Modeled (km)	Current Rim Height (m)	Current Actual Depth (m)	Current Total Depth (m)	Expected Initial Total Depth (m)	Total Depth Difference (m)	Relative Total Depth
Ksa	14, 65	39 ± 2	NA	180	470	650	1,200	550	0.46
Momoy	11, 44	$40 \pm 1^*$	NA	--	--	680*	1,200	520	0.43
Soi	4, 140	78 ± 2	80	340**	0**	340**	1,100	760	0.69
Sinlap	11, 16	82 ± 2	80	340	300	640	1,100	460	0.42
Hano	40, 345	100 ± 5	NA	250	290	540	1,060	520	0.50
Afekan	25, 200	115 ± 5	110	270	200	470	1,060	590	0.55

Crater rim height, actual depth, and total depth are average values measured from the two sides of the SARTopo crater profiles. The expected depth is the average of the depths expected for similar-size craters on Ganymede and Callisto using depth-diameter relationships for fresh craters over 25 km in diameter from Schenk (2002). Relative total depth is defined as $R(D) = 1 - d_t(D) - d_e(D)$, where $d_t(D)$ is the current total depth of the Titan crater and $d_e(D)$ is the expected depth.

*Momoy's current total depth and diameter were determined by Neish et al. (2013) using autostereo, but the apparent depth and rim heights could not be measured.

**Soi's current topographic profile is so unclear that we could not measure the rim height and apparent diameter with confidence. We choose to use the same rim height as Sinlap, and choose the final apparent depth to be zero because it is essentially at the level of the background topography.

We use the topographic profiles of the craters Ksa, Momoy, Soi, Sinlap, Hano, and Afekan from Neish et al. (2013) to measure the total crater depth (top of rim to bottom of crater), apparent crater depth (depth referenced to background terrain), and rim height at each side of the crater profiles, and found the average values. In general, these topographic profiles do not cross the centers of the craters; however, morphologically, sand infill suggests a relatively flat crater floor (see below). We cannot currently confirm that these craters have completely flat floors because each crater only has one topographic profile; however, it would appear that this one profile is likely representative. In one case (Sinlap), Neish et al. (2013) found that the SARTopo depth estimates agreed well with the estimated depth from another technique, “autostereo” (which uses differences in the foreshortening of the near and far crater walls to estimate depths), implying that Sinlap has a relatively flat floor. In comparison with their expected depths, Titan’s craters are shallowed by 460 to 760 m, and have relative total depths of between 0.42 and 0.69. The smallest craters, Ksa (diameter 39 ± 2 km) and Momoy (40 ± 1 km) fall short of the expected depth by similar amounts, 550 m and 510 m, respectively. Soi (78 ± 2 km) and Sinlap (82 ± 2 km) have nearly the same diameter within error, but they have experienced very different amounts of shallowing. Sinlap is shallowed by only 460 m, a relative total depth of 0.42, while Soi on the other hand has lost nearly all of its apparent depth, 760 m and has a relative total depth of 0.69. The largest craters Hano (100 ± 5 km) and Afekan (115 ± 5) currently fall short by comparable amounts, 520 m (relative total depth of 0.50) and 590 m (0.55), respectively. Surprisingly, all of the craters are currently at least 460 m shallower than expected.

2. What could make Titan's craters shallow?

Titan's craters initially should have had a similar depth to fresh craters on Ganymede and Callisto, and over time, one or more unknown processes has shallowed them. What could be responsible for hundreds of meters of shallowing? Initially suggested by Neish et al. (2013), the four most plausible mechanisms include: erosion and deposition by rain and rivers, direct atmospheric sedimentation of haze particles, aeolian infill of dune material, and topographic relaxation.

Erosion and deposition by rain and rivers is thought to be a less significant process for these craters specifically, simply because of where the craters are located (Fig. 2). They are all (except Hano) located within Titan's equatorial region ($\pm 30^\circ$ latitude) where global circulation models, Huygens lander data, and cloud observations predict it to be more arid and rainstorms to be infrequent (Mitchell, 2008; Rannou et al., 2006; Tokano, 2011; Tomasko et al., 2005; Turtle et al., 2011). Crater degradation through fluvial processes was modeled for some of Titan's craters through the use of a landscape evolution model (Neish et al., 2016). They found that it can modify craters to the point where they would be unrecognizable by an orbiting spacecraft given enough time and a large enough erosion rate. However, the rate of erosion depends on the latitude of the crater. Erosion by rain may not be as important in the arid dune regions near the equator (where these craters are), but could perhaps be much more important at higher latitudes where rainfall is more prevalent. While rivers are seen at all latitudes, including near the Huygens landing site at 10° S, they are notably scarce in the dune fields where most of these craters are located (Langhans et al., 2012). In general, dunes

appear to cross-cut rivers, suggesting that dune movement is more recent than fluvial activity. With the exception of Menrva (which we are not studying), none of these craters are incised in SAR imagery, but smaller-scale (and therefore unrecognizable in SAR imagery) fluvial erosion may exist. Altogether, these observations suggest that fluvial erosion may only contribute to crater shallowing during infrequent rainstorms, but is likely not solely responsible for the shallowing of the craters being studied.

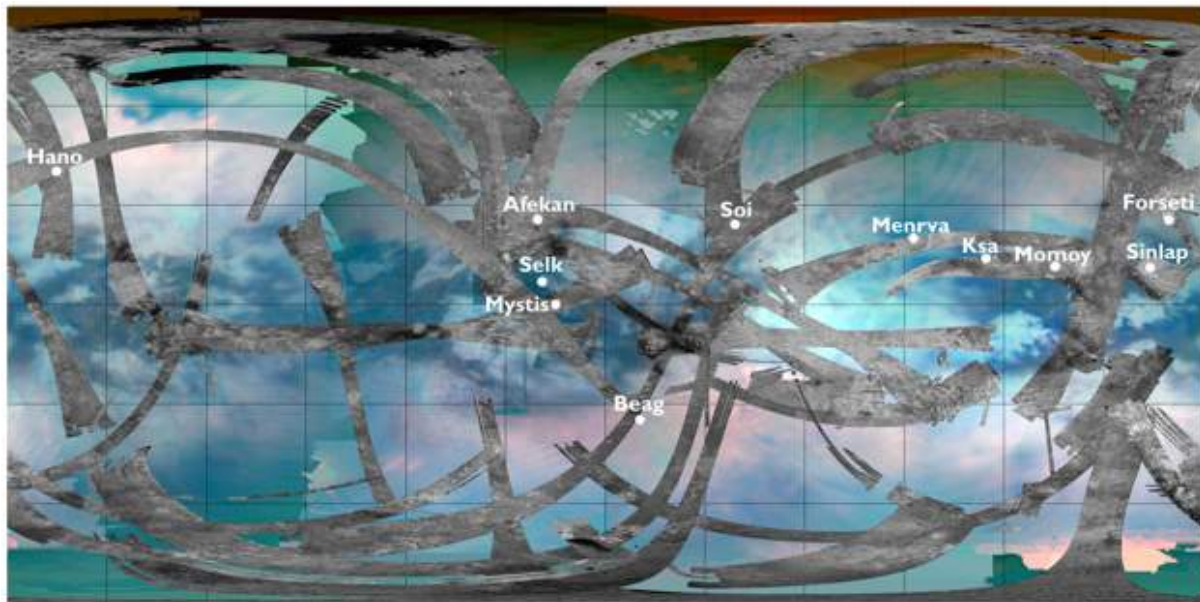


Figure 2: Global mosaic of false color spectral images from *Cassini* VIMS. Dark colors correlate with organic-rich sand seas, and light blue regions are more ice-rich. Swaths of synthetic aperture radar images are overlaid on the VIMS mosaic. Circles indicate the locations of the named craters.

Over time, the craters may have shallowed as they filled with the organic molecules that formed photochemically in the atmospheric haze layers and snowed to the surface (Cable et al., 2012), a phenomenon positively identified not only in the upper haze layers but also during the descent of the Huygens probe (Tomasko et al., 2005). As topographic low points, craters could trap and retain these fine particles. However, photochemical models suggest that the most abundant solid produced photochemically in Titan's atmosphere, acetylene, only has a sedimentation rate of order 10 m/Gyr uniformly distributed over Titan (Toublanc, et al. 1995). It is therefore unlikely that direct atmospheric sedimentation alone could shallow all of these craters by many hundreds of meters within the craters' lifetimes.

Conversely, the aeolian infill theory suggests that these craters have been filled with organic-rich sand from the nearby sand seas. Indeed, nearly all of the craters considered here (except Hano) are found within the equatorial region where there is an abundance of sand available in the surrounding sand seas (Fig. 2). In SAR imagery, it is evident that nearly all of the named craters are found adjacent to, surrounded by, and perhaps even filled with dunes and dune material (Fig. 3 A-C). Some unconfirmed crater-like shapes are found completely surrounded by and immersed with long linear dunes (Fig. 3D). These observations strongly implicate that dune infill has occurred in some crater-like features on Titan. As noted before, craters are inherently topographic lows, so it is certainly conceivable that large amounts of dune material saltated and fell within the crater bowl with no means of escape. On Earth, the 2.5 km diameter impact crater Roter Kamm in the Namib Sand Sea appears to have been filled with up to 500 m of sand from the adjacent dunes in the last ~3.7 Myr (Fudali, 1973; Radebaugh et al., 2010). It exemplifies that craters can in fact fill with large

amounts of sand; however, this crater is an order of magnitude smaller than the large, shallow craters on Titan.

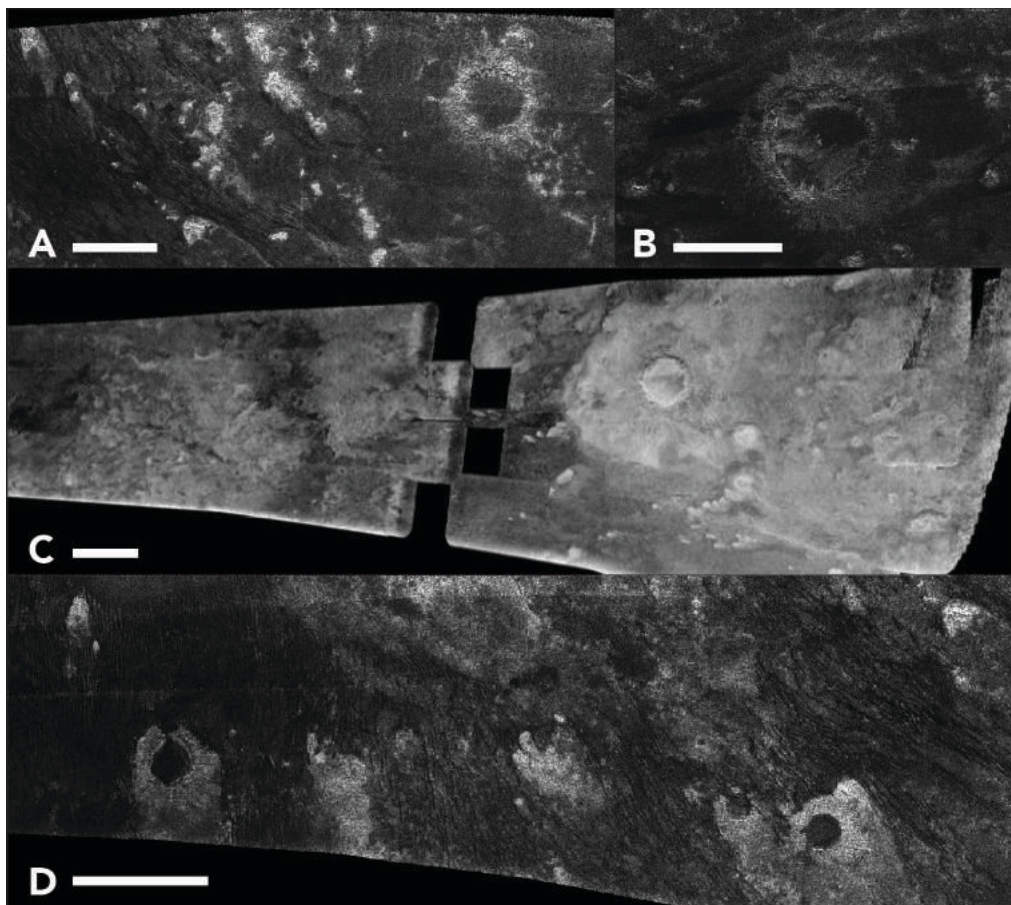


Figure 3: Cassini SAR images: A) Soi B) Afekan C) Sinlap D) Dune-filled probable craters. Scale bars are ~100 km. The darkest regions within each image are likely dunes or dune material. At these resolutions, individual dunes are difficult to resolve, but can be seen more easily in some places where they wrap around obstacles.

The fourth option, topographic relaxation has been assumed to be an unimportant process on Titan because of its low surface temperature of 94 K (Neish et al. 2013). Here, we will test this assumption. We speculate that an accumulation of low thermal conductivity, aeolian material could actually raise the effective surface temperature of the craters. The insulating effect of Titan's organic-rich sand could result in warming and topographic relaxation over time. The combination of sand infill and subsequent topographic relaxation may be a more realistic solution to the problem of the 460-760 m of unexplained depth change (approximately 1,000 - 3,000 km³ of volume change) seen in Titan's craters, rather than simply filling the craters with that much sand alone.

C. Estimating the Thermal Conductivity of Titan Sand

Titan's equatorial sand seas are thought to be composed of a mixture of simple to more complex hydrocarbons (Clark et al., 2010; Soderblom et al., 2007) that formed photochemically in the atmosphere and agglomerated into sand-sized particles (Janssen et al., 2015), instead of eroded ice-rich crustal materials as may have been assumed. The unique composition of Titan's sand is noteworthy because while most planetary surface materials such as rocks and ice have thermal conductivities between 1 and 7 W m⁻¹ K⁻¹, organics have thermal conductivities that are as much as an order of magnitude lower. For example, a study of 55 different coal samples -which are innately organic-rich- from the U.S. found that their thermal conductivities ranged from 0.22 to 0.55 W m⁻¹ K⁻¹, with a mean of 0.33 W m⁻¹ K⁻¹. The highest thermal conductivities corresponded with more mature anthracite coals, which they attribute to the initiation of graphitization (Herrin and Deming, 1996), a process that we do not expect to occur on Titan. A review of coal samples from England and Germany found similar thermal conductivities between 0.20 to 0.26 W m⁻¹ K⁻¹ (Clendenin et al., 1949). Likewise, the organic matter in soil has a thermal conductivity of 0.25 W m⁻¹ K⁻¹ (Farouki, 1981). Lastly, the thermal conductivity of benzene, an organic molecule identified in laboratory Titan tholins (Khare et al., 1984) and remotely in Titan's dunes (Clark et al., 2010), has also been studied, although at much higher pressures (Ross et al. 1979). Extrapolating their results to lower pressures, the thermal conductivity of benzene on Titan is likely similar to that of coals. Using this information, we estimate that the thermal conductivity of a solid sample of mixed organics to be ~0.25 W m⁻¹ K⁻¹.

We expect that Titan sand will have an even lower thermal conductivity because it is not simply a block of compressed organic material like coal but instead is a collection of individual sand particles intermixed with Titan's atmosphere. The optimum saltation diameter for sand on Titan is predicted to be a medium sand size, somewhere between 0.2-0.6 mm (Lorenz, 2014). The particulate nature of this medium-size sand will reduce the thermal conductivity even further, just as the thermal conductivity of quartz is reduced when in the form of sand. The thermal conductivity of quartz is 6 and 10 $\text{W m}^{-1} \text{K}^{-1}$ through its directions of minimum and maximum conductivity respectively (Diment and Pratt, 1988). Dry, medium-sized sand has a thermal conductivity between 0.27 and 0.4 $\text{W m}^{-1} \text{K}^{-1}$ for porosities between 0.35 and 0.4 (Chen, 2008; Hamdhan and Clarke, 2010; Yun and Santamarina, 2008). Therefore, the thermal conductivity of a medium-sized quartz sand is between 1/30 and 1/20 of the thermal conductivity of solid quartz (using the average initial value 8 $\text{W m}^{-1} \text{K}^{-1}$). The drop in thermal conductivity of organics when in the form of well-sorted, medium, spherical sand has not been studied; however, granular coal of size 0-1 mm has been studied at 50 °C. The original coal and the granulated coal in this study have thermal conductivities of 0.25 $\text{W m}^{-1} \text{K}^{-1}$ and 0.13 $\text{W m}^{-1} \text{K}^{-1}$ respectively (Clendenin et al., 1949). Although the decrease in thermal conductivity was only about 1/2 for the granulated coal, we expect that the actual decrease will be greater for Titan sand. The sand is presumed to be well-sorted and well-rounded because of aeolian processing. Round, uniformly sorted sands will have a lower thermal conductivity than granulated materials of a greater range of sizes and roundnesses because of the decrease in interparticle contacts and increase in porosity (Yun and Santamarina, 2008). Consequently, we estimate that the drop in thermal conductivity from

solid organics to well-rounded, medium-sized sand will be 1/10. This reduction agrees with the estimated decrease in the thermal conductivity of lunar megabreccia compared to unbroken lunar rock, which is between 1/10 and 1/100 due to the varying porosity of angular lunar rock fragments (Warren, 2011; Warren and Rasmussen, 1987). With this in mind, we estimate that Titan's sand will have a low thermal conductivity of $\sim 0.025 \text{ W m}^{-1} \text{ K}^{-1}$, consistent with the findings of Janssen et al. (2016) but excluding the effects of compaction at depth, which is expected to be minor due to the low gravity on Titan.

The low thermal conductivity of Titan's organic, medium-sized sand will enable it to act as an insulating layer on the surface. The amount of surface warming is proportional to the thickness of the insulating sand layer and inversely proportional to the thermal conductivity of the layer, in accordance with Fourier's law of heat conduction. As the thickness of sand grows, assuming all else is constant, the effective surface temperature will increase. We believe that the sand in and around Titan's craters has a low enough thermal conductivity that it will effectively warm the icy surface of the craters and aid in topographic relaxation, a process that is strongly controlled here by surface temperature.

D. Methods

Our aim is to determine if we can reproduce the current shallow depths of some of Titan's named craters. We choose to investigate the largest named craters with topographic profiles available because larger craters relax more easily than smaller craters. Therefore, we exclude Ksa and Momoy from the present study. We also exclude the largest crater Menrva (diameter ~ 450 km) because the initial depth of such a large crater is less well constrained (cf. Schenk 2002). Additionally, Hano is not investigated because it is not located near obvious sand seas, and its interpretation as a crater is equivocal. Instead, we focus on the craters Sinlap, Soi, and Afekan, which happen to show the least, most, and an intermediate amount of shallowing, respectively.

Initially, we considered a uniform increase in effective surface temperature, which might arise from a blanket of sand of uniform thickness (Schurmeier and Dombard 2014). The thickness of sand deposits, however, will be spatially variable, a scenario we consider here. Differences in the amount of dune infill in the crater bowl and the proximity of nearby dunes to the crater rim are investigated.

1. Dune Field Effective Surface Temperature Simulation

The location of nearby dunes influences the surrounding surface temperature profile around the crater. It will not yield a constant effect because of variable dune thickness and interdune spaces that are relatively sand-free. The horizontal scale of the dunes (hundreds of meters), however, is orders of magnitude smaller than the craters, so we seek to determine an effective increase in surface temperature appropriate to study the relaxing craters. To determine this effective surface temperature produced by the dune field, we use the commercially available MSC Marc-Mentat finite element package (<http://www.mscsoftware.com>). We produce planar meshes that crosscut linear dunes with surrounding interdune spaces to simulate their thermal effects at depth in a water ice crust. The physical surface is held at 94 K, and we find the thermally conductive equilibrium temperature under the dunes using our estimated conductivity of Titan's sand. Dunes are assumed to have isosceles triangular shapes through their cross-section (linear dunes are typically symmetrical in cross-section) with maximum measured dune heights of 120-180 m, and widths and spacing (empty, essentially sand-free interdune areas) from globally averaged measurements along with measurements specifically in the vicinities of the craters being studied (Savage et al., 2014). We investigate different permutations of dune widths, interdune widths, maximum dune heights, and number of dunes and find the equilibrium temperature at depth for each simulation. An example simulation is shown in the Fig. 4. The subsurface equilibrium temperatures achieved in the various simulations ranged from around

98 K to 102 K. Thus, we determine a temperature of 100 K is most representative of the effective surface temperature under a typical Titan dune field near these craters.

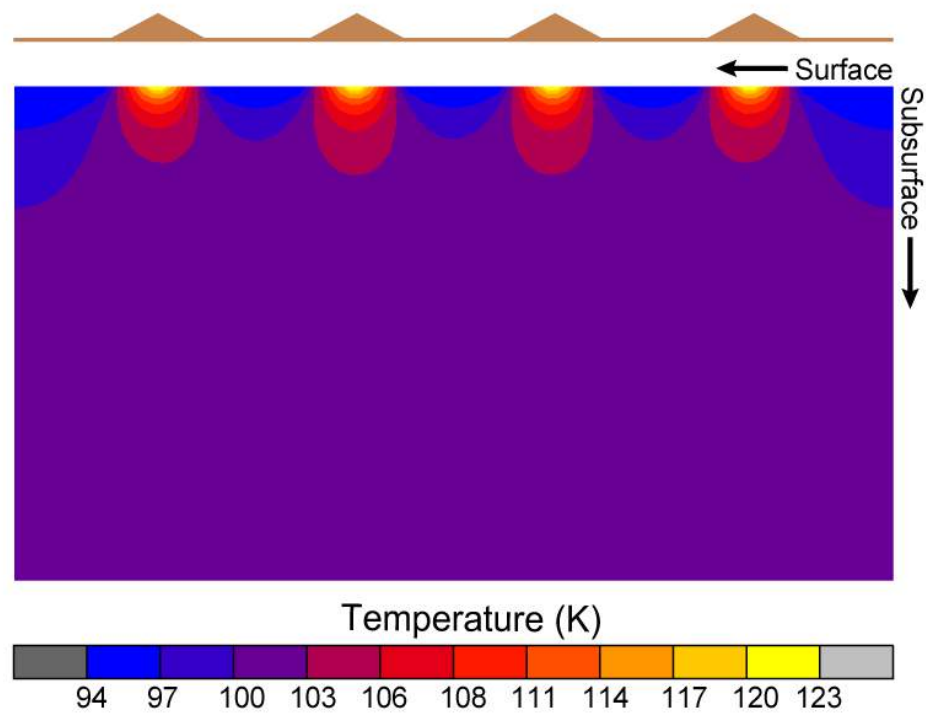


Figure 4: Example simulation with the final temperature values, and a schematic representation of the dune locations shown above.

2. Crater Relaxation Simulation with the Aid of Aeolian Infill

We again use the Marc-Mentat finite element package to simulate the relaxation of Sinlap, Soi, and Afekan, following the methods of Dombard and McKinnon (2006) and using physical properties relevant to Titan. The craters are modeled as a planar, axisymmetric mesh with a simulation space of 5 x 5 crater radii. The mesh elements are concentrated near the surface, where most of the deformation occurs. We use a simplified initial crater shape with the bowl approximated by a fourth-order polynomial, and the ejecta falls off from the rim with the third power of crater radius from 1 to 2 radii (Melosh, 1989, p. 90). To determine the initial unrelaxed crater depth (i.e., the “expected depth”), we employ the depth (d)-diameter (D) equations determined by Schenk (2002) for fresh craters on Ganymede ($d=1.63D^{0.102}$) and Callisto ($d=2.08D^{0.134}$) and average the values (all three satellites are icy worlds with similar surface gravity). We use the topographic profiles from Neish et al. (2013) to measure each crater’s rim height and apparent depth. Since the rim heights of Soi’s topographic profile are difficult to identify with confidence, we use the same initial crater shape for both Sinlap and Soi’s simulations using the measurements from Sinlap’s topographic profile. Craters with similar diameters should have similar initial shapes.

For each crater, we run a suite of steady-state thermal simulations at different effective surface temperatures, zero heat flux on the sides, and a basal heat flux of 4 mWm^{-2} , the expected current heat flux on Titan based on assumptions of the abundance Titan’s radioactive elements (Sohl, 2003). In the mesh, we assume the thermal conductivity of water ice (Petrenko and Whitworth, 1999). Effective surface temperatures are varied spatially to

emulate an increase in sand thickness across the mesh surface. Sand-free regions are set to Titan's current surface temperature of 94 K. Nearby dune-covered regions outside the crater bowl are set to the equilibrium temperature at depth most representative for under dune fields (100 K). The approximate distance of the adjacent dune field to the rims of the craters are measured from SAR imagery. We find both minimum and maximum distances to the dunes and run both for comparison. The extent of the dune fields ranges from near the rim (Soi), on the periphery of the continuous ejecta blanket (Afekan), and off the blanket (Sinlap). We set the effective surface temperature to 100 K from the starting distance of the dune field out to the end of the mesh.

To calculate the increase in effective surface temperature (ΔT) within the bowl, we select a maximum infill thickness and assume that the infill is flat (see Fig. 5). Using the sand thickness (h) at each location within the bowl (found by subtracting from the assumed crater bowl shape), we calculate the increase in effective surface temperature using the estimated thermal conductivity of the sand (k) and the heat flow (q), where:

$$\Delta T = qh/k \quad \text{and} \quad T_{\text{surface}} = \Delta T + 94 \text{ K}$$

These effective surface temperatures are then applied in the basin. The temperature increase due to sand infill can be substantial; for example, 50 m of sand results in a temperature change of 8 K (surface temperature of 102 K), while 500 m of sand results in a temperature change of 80 K (174 K).

Once the thermal state is determined, we perform a mechanical simulation to track the evolution of the surface topography. We assume uniform material properties through the mesh, using a viscoelastic rheology, a mass density of 950 kg m^{-3} , and a gravitational

acceleration of 1.35 m s^{-2} . For the elastic response, we use the properties of water ice from Gammon et al. (1983) and the ductile creep flow laws of Goldsby and Kohlstedt (2001). The grain-boundary sliding and grain-boundary diffusion creep mechanisms are sensitive to the ice grain size. We assume a grain size of 1 mm, but explore the effects of changing the grain size by an order of magnitude, a range consistent with glacial ice on Earth (cf. Dombard and McKinnon, 2006). The nominal values of Young's modulus and Poisson's ratio are 9.332 GPa and 0.325, respectively; however with this value of Poisson's ratio, the materials are compressible and will undergo gravitational self-compaction. Since the elastic response to relaxation is primarily one of lithospheric flexure, we can set the Poisson's ratio near its incompressible limit of $\frac{1}{2}$ and then scale the nominal Young's modulus in order to keep the flexural rigidity constant (for validation of this approach, see Dombard et al., 2007; Karimi et al., 2016). We implement full large-strain deformation with a formalism that enforces constant dilatation across each element, which prevents numerical errors that can arise in the simulation of nearly incompressible behavior (e.g., ductile creep). Time stepping is automatically controlled to resolve the minimum viscoelastic Maxwell time in the mesh by a factor of 4 or greater. To keep the run times reasonable, we implement a minimum viscosity in the mesh of 10^{18} Pa s . Viscosity values below this cut-off are only realized in the warm, deep mesh, separated from the relaxation flow field nearer the surface, and we have confirmed our results are not sensitive to this cut-off value. In the mesh, we apply free-slip boundary conditions to the side edges, which restrict normal displacements but permits transverse displacements, and we lock the nodes along the base in both vertical and horizontal directions.

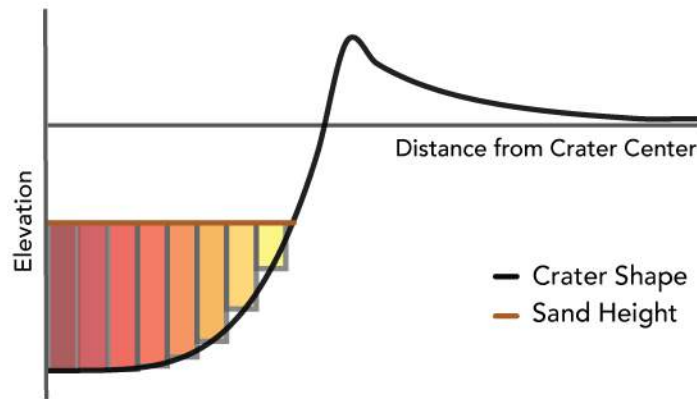


Figure 5: Schematic of the modeled crater shape (black curve), which is axisymmetric around the crater center. For each amount of sand infill, we assume a flat sand surface (brown line). The effective surface temperature increase at each mesh element within the crater is calculated using the thickness of sand over each element, the basal heat flow, and our estimated sand thermal conductivity. Thicker amounts of sand result in greater temperature increase (indicated by warmer colors).

Notably, we do not explicitly include the mechanical effects of the sand layers, assuming that they are thin and weak enough to contribute negligibly to the lithosphere's strength profile. We do apply a boundary condition along the crater bowl surface to simulate the pressure effect of the weight of the overlying sand. Each element with appreciable sand above it is assigned a hydrostatic pressure ($P = \rho gh$), depending on the thickness of the material above it, h (see Fig. 5), Titan's gravitational acceleration ($g = 1.352 \text{ m s}^{-2}$), and the density of Titan sand, ρ . While the density of Titan sand has not been directly measured, there are some constraints on the density of the aerosols from which the sand most likely originates. Hörst and Tolbert (2013) performed a comprehensive study of the size, number

density, and particle density of laboratory Titan aerosol analogs for CH₄ concentrations from 0.01% to 10% using two different energy sources, spark discharge and UV. They found that the aerosols ranged in size from ~15 – 56 nm and an effective density that ranges from ~400 – 1,100 kg m⁻³. An earlier study by Trainer et al. (2006) estimated a similar effective density of ~800 kg m⁻³. Titan sands are much larger and are expected to be aggregates of these aerosols. Individual sand particles will likely have a density within this range; however, a stack of sand will include considerable void space between the sand particles and therefore have a lower bulk density. The porosity of most terrestrial aeolian sands ranges from around 30% to 50% (Pye and Tsoar, 1990; Atkins and McBride 1992). Consequently, the bulk density of the sand should be within the range of 200 kg m⁻³ to 770 kg m⁻³. In our simulations, we bracket this range, employing values of 200 kg m⁻³ and 800 kg m⁻³.

Each simulation thus assumes an initial amount of sand infill, with a flat surface, under which the icy surface topography is progressively relaxing. We aim to find the time when the sand infill has induced relaxation enough to shallow the crater from the expected fresh shape to the current shape. We calculate this evolution as a volume change (V_c) between the initial and current shapes of the crater basin. This volume change thus equals the sum of volume of sand infill (V_s) plus any volume change caused by relaxation (V_r). At each time step in the simulations, the crater has a different topographic profile. We use this profile and the initial crater profile to find the relaxed volume (V_r) using a sum of cylindrical rings between the two curves (see Fig. 6). For each simulation, the sand volume is constant, but we assume the sand is mobile enough to maintain a flat surface. The time needed to relax a crater to its current depth thus occurs when $V_c - V_s = V_r$. Since crater shapes are exported in specified time steps,

it is unlikely that the volume change due to relaxation (V_r) will exactly equal $V_c - V_s$. Therefore, we find the times when $V_r - (V_c - V_s)$ is just above zero and just below, then use a linear interpolation to find the relaxation time and express this possible range of times as error bars in our results.

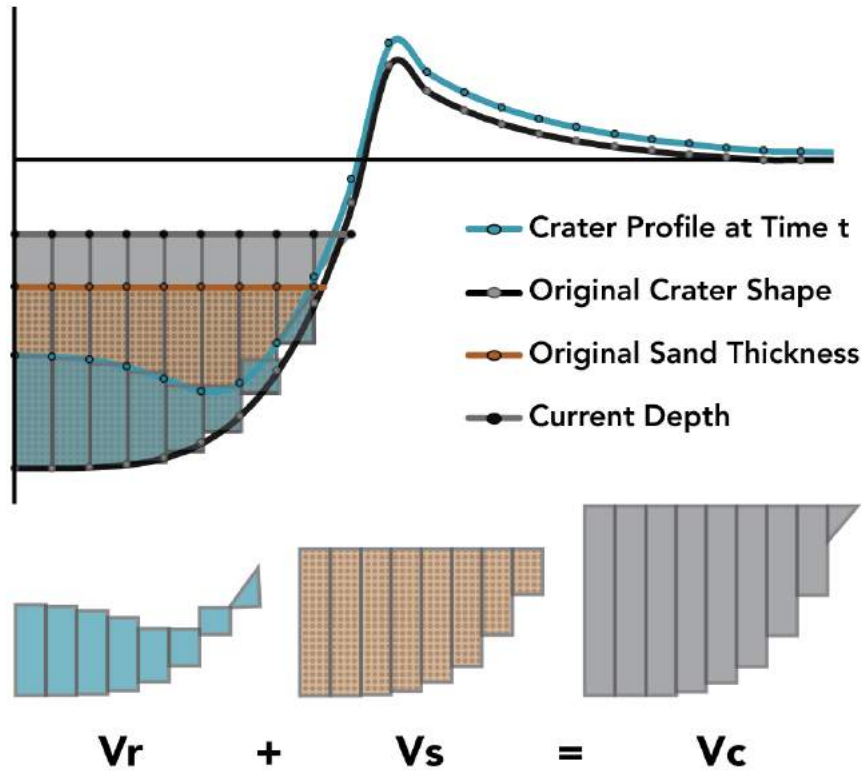


Figure 6: Example of a volume calculation for Afekan. Relaxation is complete when the volume relaxed (V_r) is equal to the difference in volume between the total volume change (V_c) and the volume of sand (V_s).

We use this relaxation time to determine if it is likely that relaxation occurred for these craters, or if sand infill alone is more likely and no significant relaxation occurred (i.e., relaxation takes too long). The crater retention age on Titan is poorly constrained (Neish and Lorenz, 2012), but could be 200 Myr using the Artemieva and Lunine (2005) model or 1 Gyr using the Korycansky and Zahnle (2005) model. However, these cannot be upper and lower estimates due to the factor of four uncertainty in the absolute cratering rate. The dunes on Titan are estimated to have a maximum age of 730 Myr old (Rodriguez et al., 2014), so we choose to use this as an upper limit on the amount of time that these craters could relax due to sand infill.

These results therefore determine if Titan's dunes can induce viscoelastic flow within Titan's icy crust underneath the craters and the dune fields, or if the shallowing of the craters is merely surficial exogenic processes. Additionally, this work provides new estimates on the amount of sand present within these large craters, which contributes to the inventory of organics across Titan's surface.

E. Results

Titan's craters Sinlap, Soi, and Afekan are currently 460 m, 760 m, and 590 m shallower, respectively, than expected. At Titan's current surface temperature of 94 K, none of the three craters could relax to their current depths in less than the maximum simulation runtime of 4 Gyr. For example, the largest crater in the study, Afekan, only uplifted a mere 70 m in 4 Gyr using the current surface temperature. Thus, in order for significant relaxation to occur, it would seem that very low thermal conductivity sand is required to raise the surface temperature.

The effect of the adjacent dune fields on crater relaxation appears to be minimal. We find that the average effective temperature produced at depth under Titan's dune fields is about 100 K, and simulations using this far-field surface temperature are negligibly different from simulations just using a surface temperature of 94 K across the whole domain. We therefore only show the results of the simulations with a minimum distance from the crater rim to the start of the dune field. The amount of aeolian infill within the crater, however, greatly affects the amount of time required for the crater to relax to its current depth. The reason is twofold. First, any amount of sand introduced will obviously result in a shallower measured crater depth. This factor not only raises the apparent crater floor, but it also reduces the amount of uplift required to relax the crater to its current depth, which in turn requires less time to achieve. Second, increasing the thickness of Titan's sand infill results in a linear increase in the effective surface temperature within the crater bowl in proportion to the thermal conductivity. Warmer temperatures aid relaxation.

To determine what effect the amount of sand infill has on relaxation, we determine the amount of time required for each crater to relax to its current depth, under different amounts of sand infill. We plot this time versus the percent relative sand volume infill, which is defined as:

$$\text{Percent Relative Sand Volume Infill} \equiv R = (V_s)/(V_c) 100\%,$$

where V_s is the volume of sand in the crater bowl, and V_c is the depth change required to get from the expected depth to the current depth. By this definition, 0% means that the crater has no sand infill and all of the depth change is due to topographic relaxation alone (which our results show is not plausible), and 100% indicates that the crater is completely filled with sand and no relaxation is required.

The simulations show that at a basal heat flow of 4 mW m^{-2} and an ice grain size of 1 mm, and the lower limit of our estimated sand density, 200 kg m^{-3} , all three craters can topographically relax when mostly filled with low thermal conductivity sand (Fig. 7). In this figure, we show the time needed for relaxation to complete the shallowing of the craters for a given percentage of sand fill. Take the case of Afekan. When the crater is nearly filled with sand, the time needed to complete the relaxation is short because not much relaxation is required and because the thermal effect of the sand is high. In fact for the highest sand volumes, times are short enough ($< 100 \text{ Myr}$) that we would need to consider the diffusion of the thermal anomaly into the interior (we will return to this point below). For lower sand infill amounts, the time to complete the shallowing via relaxation rises precipitously, again because more relaxation is required and the thermal effect that would speed relaxation is reduced. Indeed for relative sand volumes less than $\sim 57\%$, the requisite time for relaxation to

complete the shallowing of Afekan becomes untenable (billion year time scales) because the age of the dunes is expected to be 730 Myr (Rodriguez et al., 2014). Sinlap would only relax in less than this time limit for relative sand infill volumes over ~95%, while Soi can relax to its current depth for relative sand infill volumes over ~70%.

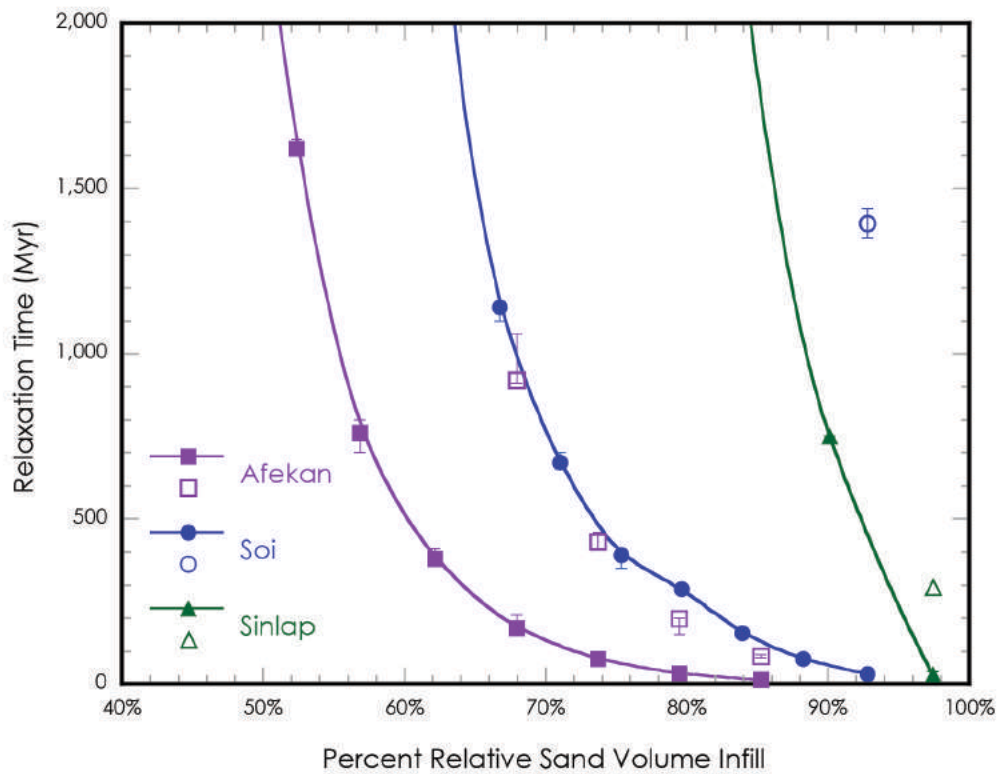


Figure 7: Crater relaxation times (the time required to relax the remaining volume) for different relative volumes of sand infill to reach the current crater depth for Afekan, Soi, and Sinlap using two sand densities (solid symbols for a density of 200 kg m^{-3} and open symbols for a density of 800 kg m^{-3}).

Using our maximum estimated sand density of 800 kg m^{-3} , all three craters require greater amounts of time to relax to their current state. In the case of Soi, which requires the greatest amount of total depth change and thus a greater amount of sand infill and relaxation, relaxation could not occur in a reasonable amount of time. Sinlap does relax at this sand density, but only in a reasonable amount of time for relative sand infill volume percentages over 97% (the greatest effective surface temperature applied for Sinlap). Hence, relaxation is not very important for Sinlap and Soi at the maximum sand density. Afekan reaches its current shallow depth through both infill and relaxation in reasonable amounts of time with relative sand infill volume percentages over ~70%. These two sand densities are considered to be maximum and minimum values, and therefore the actual amount of relaxation is likely somewhere in between.

Thus, Titan's craters should not be shallow due to sand infill alone, and topographic relaxation likely also plays a role. Afekan, Soi, and Sinlap could have relative sand infill percentages as low as ~62%, ~71%, and ~97%, respectively, while only needing to relax the remaining depths in a few hundred million years, assuming a sand density of 200 kg m^{-3} . These values are lower bounds. Placing upper bounds is convoluted, however, as the amount of sand infill is convoluted with the age of the dunes. For example, if the dunes are old (up to the maximum inferred age), then the relaxation process has more time to operate and thus less sand infill is needed. Conversely, if the dunes are old and if the craters were filled with more sand than indicated, relaxation would shallow to their current depth relatively quickly. These craters would still continue to relax, however, and therefore should be even shallower than observed. In any event, we can specify minimum volumes of sand; Afekan, Sinlap, and

Soi may only require $1.9 \times 10^3 \text{ km}^3$, $9 \times 10^2 \text{ km}^3$, and $1.5 \times 10^3 \text{ km}^3$ of sand infill respectively, instead of needing $3 \times 10^3 \text{ km}^3$, $1 \times 10^3 \text{ km}^3$, and $2 \times 10^3 \text{ km}^3$ if completely filled with sand. These changes in sand volumes are small compared to Titan's global sand inventory, (Arnold et al., 2014). so the impact of this work lies in understanding the processes by which Titan erases its craters.

Additionally, the grain size of the water ice in the simulation affects the relaxation times significantly. We find that increasing or decreasing the grain size by an order of magnitude resulted in a direct change in the required relaxation time for a given amount of sand infill by around an order of magnitude (Fig. 8). This finding means that if the grain size is an order of magnitude smaller on Titan (0.1 mm, which is reasonable), relaxation is greatly accelerated, and these craters would need even less sand infill by some tens of volume percent. At this grain size, relaxation may be significant. In contrast, if the ice grain size is larger (10 mm, again reasonable), relaxation would be slowed, and more sand infill would be required, again by some tens of volume percent. Overall, this shows that crater relaxation can occur in Titan's craters, but aeolian infill is still the main cause of the shallowness.

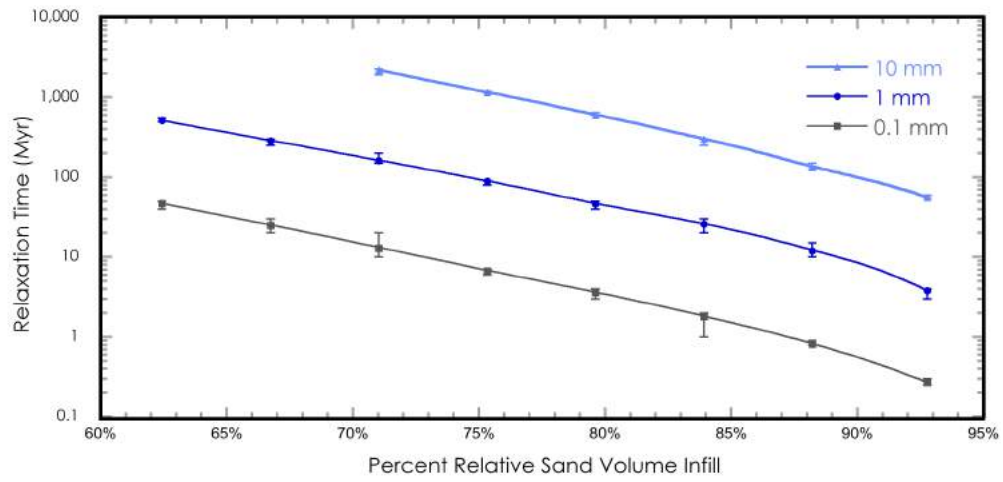


Figure 8: Crater relaxation times for different relative volumes of sand infill in SoI using three grain sizes: 10 mm, 1 mm, and 0.1 mm, with no added pressure effects.

F. Discussion

The current total depths of Sinlap, Soi, and Afekan are 58%, 30% and 44% of their expected depths compared to similar-size craters on Ganymede and Callisto. It was previously hypothesized that the cause of that shallowness is simply aeolian infill of sand from nearby dune fields. We have shown that solely aeolian infill plausibly, if not likely, is not the only cause because that much sand will encourage topographic relaxation due to the sand's low thermal conductivity. Instead of filling Sinlap, Soi, or Afekan's missing crater volume with 100% sand (about 1,000 km³, 2,000 km³, and 3,000 km³, respectively), these craters may only need relative sand infill percentages of ~97%, ~71%, and ~62%, which in turn warms the subsurface beneath the crater and results in topographic relaxation under the current expected heat flow (4 mW/m²). While the heat flow could have changed over time, the expected heat flow at the maximum age of the dunes, 730 Myr (Rodriguez et al., 2014) was likely around 5 mW/m², which would only accelerate relaxation. The potential for some degree of relaxation reduces the necessity of sand mobility on Titan. Conceptually, the differences in aeolian infill volume are important because it may be more physically realistic to fill these craters with these lesser sand infill amounts over the age of the sand seas. Further investigation of the mechanisms and timescales of aeolian infilling of craters is needed to confirm this conclusion.

While our results are simply meant to investigate if topographic relaxation is an important mechanism that shallows Titan's craters, there are caveats. For instance, the weight of the sand infill partially reduces the topographic stresses that drive relaxation. As a thought

experiment, consider a crater completely filled with sand the same density of ice. There would be no topographic stresses in this case, and no relaxation. Likely densities of the sand infill, however, are lower than ice, but the effect can still be profound. At the higher end of the density range (800 kg m^{-3}), the added weight effectively negates the need for any relaxation for Sinlap and Soi. Afekan relaxes, however, so our primary conclusion (that relaxation can be a factor in the shallowing of Titan's craters) still holds.

Next is the temporal aspect. Our simulations assume a thermal steady state; however realistically, the craters need time to fill with sand, and the adjacent dunes will move. The movement of the adjacent dunes should have little effect on crater relaxation because their contribution to the temperature increase is small. The crater bowl however, will warm over time as the sand layer thickens. This fill time is currently unconstrained, with only an upper age estimated for the dunes (Rodriguez et al., 2014).

One aspect of this process that we can quantify is how long it will take for the perturbation in effective surface temperature to diffuse into the interior. We perform a transient thermal simulation of the largest crater (Afekan) that starts with the heat flow in equilibrium with a sand-free surface temperature (94 K), but then adds the prescribed effective surface temperature perturbation. We then track how long it takes for the ice at depth to warm, assuming a diffusivity of ice that combines the conductivity (Petrenko and Whitworth, 1999) with the specific heat and density (see Klinger, 1981). We confirm that the relaxation flow field beneath a crater reaches about one crater radius deep, and the results of this transient simulation show thermal equilibration at these depths over time scales of tens of

millions of years. While possible, it is implausible that Titan's sands and dunes are that young, thereby justifying our general use of a steady state thermal profile.

A corollary is that if the craters fill with sand over time scales longer than this diffusion time scale of tens of millions of years, then the warming of the interior will follow the changing surface temperature with minimal lag time. Consequently since the emplacement time of the sand infill is unconstrained, all of our relaxation times are minimum relaxation times starting at when the crater is filled with that relative infill thickness. The actual time it takes these craters to relax will be greater. Considering that many of our simulations (such as those with higher relative sand infill thicknesses) take relatively little time compared to the maximum age of the dunes, this increase in relaxation time does not change our conclusion that sand infill aids relaxation and helps produce the current shallow depths of Titan's craters. Similarly, sand thicknesses in a relaxing crater will change as the sand re-adjusts to the new shape; we estimate that the effect on the change in surface temperature could be up to several tens of percent. This change would affect our final simulated numbers, but it will not change our primary conclusion that relaxation is a factor on the shallowing of Titan's craters, because in order for this change to be important, significant relaxation would have needed to occur.

Second, all of our calculations are dependent on the thermal conductivity of Titan sand, which we have estimated but has not yet been measured at Titan conditions. If the thermal conductivity is lower than estimated, less sand would be required to reach the same effective surface temperature within the crater bowl. However, because there is less sand, the relative sand infill will decrease, and more relaxation will be required to reach the current

depth. That is, relaxation becomes an even more important factor. Higher thermal conductivities (such as might happen from Titan's relatively high density atmosphere filling pore spaces) would require greater sand infill thickness to reach the same effective surface temperature, but require less uplift from crater relaxation. Simulations of Afekan that use a doubled sand conductivity show less relaxation, increasing the sand infill from 60-70% to 80-90%. Thus, the conclusion that relaxation is a factor in the shallowing of Titan's craters again holds.

Another unknown factor is the ages of the craters. Based on SAR imagery, some craters look older and more degraded than others. By visual inspection, the order of increasing relative degradation in the craters being studied is Sinlap, Afekan, then Soi. Soi and Sinlap are often compared because of their similar diameters. Despite sharing the same diameter, Soi looks much more degraded, has no obvious ejecta, and has a topographic profile that no longer resembles a crater. If they were initially similar shapes, Soi requires much more relaxation, erosion, infill, or any combination of the three processes to have shallowed to nearly nothing compared to Sinlap. Because of the greater depth change required, we find that Soi requires the greatest amount of sand infill to relax to its current depth. Perhaps Soi was present longer than Sinlap, long before the appearance of the dunes. If Soi was present longer, it may have been more degraded by other forces (wind and fluids), allowing dunes to more easily climb the ejecta and rim remnants than at the more pristine crater, Sinlap. Soi may have filled much more easily with sand, allowing not only a thicker sand layer, but also as we have shown here, more relaxation. Afekan may have also been more degraded than Sinlap, and dunes could more easily climb and accumulate within the

crater. Evidence for this hypothesis is seen in SAR imagery. Large linear dunes are present closer to and in greater sand volumes to Soi and Afekan than at Sinlap (Arnold et al., 2014). The amount of sand present within the crater or the amount of time that it was filled with sand are both factors that control the depth of the crater.

A final, but obvious, caveat is that this method is only applicable to craters filled with low thermal conductivity sand. The crater Hano is nearly the same size as Afekan in diameter and only slightly deeper than Afekan in depth, but it does not appear to be located in a sand sea. It is unlikely that it would be filled with large amounts of sand without the presence of nearby dunes. Some other mechanism has shallowed Hano, or Hano is not an impact crater. If it is a crater, the most likely cause is erosion by rain and rivers. At 40° N latitude, it is not within the drier equatorial region of Titan, so the erosion by rain may be more important. Perhaps this hypothesis is why the majority of identified impact craters are within the dry equatorial region. Outside the dry region, seasonal rains and fluvial/lacustrine processes may have been responsible for crater degradation and removal. Within the equatorial region, crater shapes may be more easily identified because infrequent rain has not completely eroded the most identifiable crater feature in imagery, the rim. Over time, these craters became surrounded by and filled with dunes. This process either buried them if they were small or eroded enough to begin with, or initiated crater relaxation in the larger craters. Signs of this process are seen in SAR imagery. Within the equatorial regions, there are many examples of medium-size crater-like rims filled with and surrounded by dunes (i.e., Fig. 3D) (Wood et al. 2010). These craters are much smaller and could more easily fill completely with sand than larger craters, because they require less volume of sand to be completely filled

and because of shorter rims that the sand must climb. We suggest that Titan lacks impact craters overall because of pluvial degradation in the high latitudes, but while some pluvial and fluvial erosion may have occurred, the dominant processes in the low latitudes are aeolian infill aided by topographic relaxation. Current data cannot clearly discriminate between the two theories: sand infill alone or sand and relaxation together. Future missions with ground penetrating radar instruments (similar to the Mars SHARAD) could look within the sandy crater interiors for reflectors that show signs of relaxation, such as significantly shallower depths than expected to the icy crater floor and upbowed floors of the crater center (e.g., Dombard and McKinnon, 2006).

G. Conclusions

Titan currently only has a handful of recognized craters on its surface, unlike nearly every other moon in our solar system, and much more akin to our planet Earth. These craters are currently many hundreds of meters shallower than the depths expected for similar-size fresh craters on Ganymede and Callisto, moons of similar size, composition, and target lithology (Neish et al., 2013). If these craters were initially the same depth as fresh craters on Ganymede or Callisto, some process has modified and shallowed them over time. Since all of Titan's recognized craters (with the exception of Hano) are located within the arid equatorial sand seas and are surrounded by long linear dunes, aeolian infill likely plays a major role in shallowing the craters. However, due to the unique thermal properties of Titan's organic-rich sand, we find that not all of the missing depth must be explained by sand infill alone, but also by topographic relaxation. Our estimated thermal conductivity of Titan's sand, $0.025 \text{ W m}^{-1} \text{ K}^{-1}$, is notably low compared to non-porous ice and silicates ($1 - 7 \text{ W m}^{-1} \text{ K}^{-1}$), and when in thick deposits, will result in a thermal blanketing effect. Craters surrounded by and filled with this sand will have increased effective surface temperatures directly proportional to the thickness of the sand layers. Increased surface temperatures can lead to topographic relaxation of the crater into a shallower shape.

We find that the combination of aeolian infill of low thermal conductivity sand and subsequent topographic relaxation can produce the current crater depths of Sinlap, Soi, and Afekan in a geologically reasonable period of time. The location of adjacent dunes does not have a significant influence on relaxation and crater depth. The amount of aeolian infill,

however, has a major influence on the amount of time needed to relax the craters to their current depth. We have shown that at the current basal heat flux, instead of needing to fill completely the missing volume with only sand, Afekan, Soi, and Sinlap could have relative sand infill percentages as low as ~62%, ~71%, and ~97%, respectively, while only needing to relax the remaining depths in a few hundred million years, assuming a sand density of 200 kg m^{-3} . This finding means that lower sand volumes are needed to shallow Titan's craters and may contribute to why Titan lacks impact craters. While many processes may lead to crater removal, we conclude that craters are being mainly shallowed and removed by rain and fluvial processes in the high latitudes, and aeolian infill coupled with topographic relaxation in the equatorial region.

H. Works Cited

- Arnold, K.D., Radebaugh, J., Morris, T.H., 2014. Sand Sea Extents and Sediment Volumes on Titan from Dune Parameters. Masters Thesis.
- Buratti, B.J., Sotin, C., Lawrence, K., Brown, R.H., Le Mouélic, S., Soderblom, J.M., Barnes, J., Clark, R.N., Baines, K.H., Nicholson, P.D., 2012. A newly discovered impact crater in Titan's Senkyo: Cassini VIMS observations and comparison with other impact features. *Planet. Space Sci.* 60, 18-25. doi:10.1016/j.pss.2011.05.004
- Burr, D.M., Taylor Perron, J., Lamb, M.P., Irwin, R.P., Collins, G.C., Howard, A.D., Sklar, L.S., Moore, J.M., Ádámkovics, M., Baker, V.R., Drummond, S. a., Black, B. a., 2013. Fluvial features on Titan: Insights from morphology and modeling. *Bull. Geol. Soc. Am.* 125, 299-321. doi:10.1130/B30612.1
- Cable, M.L., Hörst, S.M., Hodyss, R., Beauchamp, P.M., Smith, M.A., Willis, P.A., 2012. Titan tholins: Simulating Titan organic chemistry in the Cassini-Huygens era. *Chem. Rev.* 112, 1882-1909. doi:10.1021/cr200221x
- Chen, S.X., 2008. Thermal conductivity of sands. *Heat Mass Transf. und Stoffuebertragung* 44, 1241-1246. doi:10.1007/s00231-007-0357-1
- Clark, R.N., Curchin, J.M., Barnes, J.W., Jaumann, R., Soderblom, L., Cruikshank, D.P., Brown, R.H., Rodriguez, S., Lunine, J., Stephan, K., Hoefen, T.M., Le Mouélic, S., Sotin, C., Baines, K.H., Buratti, B.J., Nicholson, P.D., 2010. Detection and mapping of hydrocarbon deposits on Titan. *J. Geophys. Res. E Planets* 115. doi:10.1029/2009JE003369
- Clendenin, J.D., Barclay, K.M., Donald, H.J., Gillmore, D.W., Wright, C.C., 1949. Thermal and electrical properties of anthracite and bituminous coals. *Trans. Seventh Annu. Anthracite Conf. Lehigh Univ.*
- Diment, W.H., Pratt, H.R., 1988. Thermal Conductivity of Some Rock-Forming Minerals : A Tabulation. USGS Rep. 16.
- Dombard, A.J., Johnson, C.L., Richards, M.A., Solomon, S.C., 2007. A magmatic loading model for coronae on Venus. *J. Geophys. Res. E Planets* 112, 1-13. doi:10.1029/2006JE002731
- Dombard, A.J., McKinnon, W.B., 2006. Elastoviscoplastic relaxation of impact crater topography with application to Ganymede and Callisto. *J. Geophys. Res. E Planets* 111, 1-22. doi:10.1029/2005JE002445
- Farouki, O., 1981. Thermal properties of soils. CRREL Monograph No. 81-1. U.S. Army Corps of Engineers Cold Regions Research and Engineering Laboratory, Hanover, NH

- Fudali, R.F., 1973. Roter Kamm: Evidence for an impact origin. *Meteorics* 8, 245-256
- Hamdhan, I.N., Clarke, B.G., 2010. Determination of thermal conductivity of coarse and fine sand soils. In: *Proc. World Geotherm. Conf.*, pp. 2952-2958.
- Janssen, M. a., Le Gall, a., Lopes, R.M., Lorenz, R.D., Malaska, M.J., Hayes, a. G., Neish, C.D., Solomonidou, a., Mitchell, K.L., Radebaugh, J., Keihm, S.J., Choukroun, M., Leyrat, C., Encrenaz, P.J., Mastrogiuseppe, M., 2015. Titan's surface at 2.18-cm wavelength imaged by the Cassini RADAR radiometer: Results and interpretations through the first ten years of observation. *Icarus* 270, 443-459. doi:10.1016/j.icarus.2015.09.027
- Karimi, S., Dombard, A.J., Buczkowski, D.L., Robbins, S.J., Williams, R.M., 2016. Using the viscoelastic relaxation of large impact craters to study the thermal history of Mars. *Icarus* 272, 102-113. doi:10.1016/j.icarus.2016.02.037
- Khare, B.N., Sagan, C., Thompson, W.R., Arakawa, E.T., Suits, F., Callcott, T. a, Williams, M.W., Shrader, S., Ogino, H., Willingham, T.O., Nagy, B., 1984. The organic aerosols of Titan. *Adv. Space Res.* 4, 59-68. doi:10.1016/0273-1177(84)90545-3
- Klinger, J., 1981. Some consequences of a phase-transition of water ice on the heat-balance of comet nuclei. *Icarus* 47, 320-324.
- Langhans, M.H., Jaumann, R., Stephan, K., Brown, R.H., Buratti, B.J., Clark, R.N., Baines, K.H., Nicholson, P.D., Lorenz, R.D., Soderblom, L. a., Soderblom, J.M., Sotin, C., Barnes, J.W., Nelson, R., 2012. Titan's fluvial valleys: Morphology, distribution, and spectral properties. *Planet. Space Sci.* 60, 34-51. doi:10.1016/j.pss.2011.01.020
- Liu, Z.Y.C., Radebaugh, J., Harris, R. a., Christiansen, E.H., Neish, C.D., Kirk, R.L., Lorenz, R.D., 2016. The tectonics of Titan: Global structural mapping from Cassini RADAR. *Icarus* 270, 14-29. doi:10.1016/j.icarus.2015.11.021
- Lorenz, R.D., 2014. Physics of saltation and sand transport on Titan: A brief review. *Icarus* 230, 162-167. doi:10.1016/j.icarus.2013.06.023
- Lorenz, R.D., Kirk, R.L., Hayes, A.G., Anderson, Y.Z., Lunine, J.I., Tokano, T., Turtle, E.P., Malaska, M.J., Soderblom, J.M., Lucas, A., Karatekin, Ö., Wall, S.D., 2014. A radar map of Titan Seas: Tidal dissipation and ocean mixing through the throat of Kraken. *Icarus* 237, 9-15. doi:10.1016/j.icarus.2014.04.005
- Lorenz, R.D., Wall, S., Radebaugh, J., Boubin, G., Reffet, E., Janssen, M., Stofan, E., Lopes, R., Kirk, R., Elachi, C., Lunine, J., Mitchell, K., Paganelli, F., Soderblom, L., Wood, C., Wye, L., Zebker, H., Anderson, Y., Ostro, S., Allison, M., Boehmer, R., Callahan, P., Encrenaz, P., Ori, G.G., Francescetti, G., Gim, Y., Hamilton, G., Hensley, S., Johnson, W., Kelleher, K., Muhleman, D., Picardi, G., Posa, F., Roth, L., Seu, R., Shaffer, S., Stiles, B., Vetrella, S., Flamini, E., West, R., 2006. The sand seas of Titan: Cassini RADAR observations of

- longitudinal dunes. *Science* 312, 724–727. doi:10.1126/science.1123257
- Lorenz, R.D., Wood, C. a., Lunine, J.I., Wall, S.D., Lopes, R.M., Mitchell, K.L., Paganelli, F., Anderson, Y.Z., Wye, L., Tsai, C., Zebker, H., Stofan, E.R., 2007. Titan's young surface: Initial impact crater survey by Cassini RADAR and model comparison. *Geophys. Res. Lett.* 34, 1–5. doi:10.1029/2006GL028971
- Mitchell, J.L., 2008. The drying of Titan's dunes: Titan's methane hydrology and its impact on atmospheric circulation. *J. Geophys. Res. E Planets* 113, 1–22. doi:10.1029/2007JE003017
- Neish, C.D., Kirk, R.L., Lorenz, R.D., Bray, V.J., Schenk, P., Stiles, B.W., Turtle, E., Mitchell, K., Hayes, a., 2013. Crater topography on Titan: Implications for landscape evolution. *Icarus* 223, 82–90. doi:10.1016/j.icarus.2012.11.030
- Neish, C.D., Lorenz, R.D., 2012. Titan's global crater population: A new assessment. *Planet. Space Sci.* 60, 26–33. doi:10.1016/j.pss.2011.02.016
- Neish, C.D., Molaro, J.L., Lora, J.M., Howard, a. D., Kirk, R.L., Schenk, P., Bray, V.J., Lorenz, R.D., 2016. Fluvial erosion as a mechanism for crater modification on Titan. *Icarus* 270, 114–129. doi:10.1016/j.icarus.2015.07.022
- Radebaugh, J., 2013. Dunes on Saturn's moon Titan as revealed by the Cassini Mission. *Aeolian Res.* 11, 23–41. doi:10.1016/j.aeolia.2013.07.001
- Radebaugh, J., Lopes, R.M.C., Lunine, J.I., Kirk, R.L., Wall, S.D., Stofan, E.R., Lorenz, R.D., 2007. Mountains on Titan observed by Cassini Radar. *Icarus* 192, 77–91. doi:10.1016/j.icarus.2007.06.020
- Radebaugh, J., Lorenz, R., Farr, T., Paillou, P., Savage, C., Spencer, C., 2010. Linear dunes on Titan and earth: Initial remote sensing comparisons. *Geomorphology* 121, 122–132. doi:10.1016/j.geomorph.2009.02.022
- Rannou, P., Montmessin, F., Hourdin, F., Lebonnois, S., 2006. The latitudinal distribution of clouds on Titan. *Science* (80-.). 311, 201–205. doi:10.1126/science.1118424
- Rodriguez, S., Garcia, a., Lucas, a., Appéré, T., Le Gall, a., Reffet, E., Le Corre, L., Le Mouélic, S., Cornet, T., Courrech du Pont, S., Narteau, C., Bourgeois, O., Radebaugh, J., Arnold, K., Barnes, J.W., Stephan, K., Jaumann, R., Sotin, C., Brown, R.H., Lorenz, R.D., Turtle, E.P., 2014. Global mapping and characterization of Titan's dune fields with Cassini: Correlation between RADAR and VIMS observations. *Icarus* 230, 168–179. doi:10.1016/j.icarus.2013.11.017
- Ross, R.G., Andersson, P., Bäckström, G., 1979. Thermal conductivity and heat capacity of benzene, naphthalene and anthracene under pressure. *Mol. Phys.* 38, 527–533.

doi:10.1080/00268977900101851

Savage, C.J., Radebaugh, J., Christiansen, E.H., Lorenz, R.D., 2014. Implications of dune pattern analysis for Titan's surface history. *Icarus* 230, 180–190.

doi:10.1016/j.icarus.2013.08.009

Schenk, P.M., 2002. Thickness constraints on the icy shells of the galilean satellites from a comparison of crater shapes. *Nature* 417, 419–421. doi:10.1038/417419a

Soderblom, L. a., Kirk, R.L., Lunine, J.I., Anderson, J. a., Baines, K.H., Barnes, J.W., Barrett, J.M., Brown, R.H., Buratti, B.J., Clark, R.N., Cruikshank, D.P., Elachi, C., Janssen, M. a., Jaumann, R., Karkoschka, E., Mouélic, S. Le, Lopes, R.M., Lorenz, R.D., McCord, T.B., Nicholson, P.D., Radebaugh, J., Rizk, B., Sotin, C., Stofan, E.R., Sucharski, T.L., Tomasko, M.G., Wall, S.D., 2007. Correlations between Cassini VIMS spectra and RADAR SAR images: Implications for Titan's surface composition and the character of the Huygens Probe Landing Site. *Planet. Space Sci.* 55, 2025–2036. doi:10.1016/j.pss.2007.04.014

Sohl, F., 2003. Interior structure models and tidal Love numbers of Titan. *J. Geophys. Res.* 108, 1–13. doi:10.1029/2003JE002044

Stiles, B.W., Hensley, S., Gim, Y., Bates, D.M., Kirk, R.L., Hayes, A., Radebaugh, J., Lorenz, R.D., Mitchell, K.L., Callahan, P.S., Zebker, H., Johnson, W.T.K., Wall, S.D., Lunine, J.I., Wood, C. a., Janssen, M., Pelletier, F., West, R.D., Veeramacheneni, C., 2009. Determining Titan surface topography from Cassini SAR data. *Icarus* 202, 584–598. doi:10.1016/j.icarus.2009.03.032

Stofan, E.R., Elachi, C., Lunine, J.I., Lorenz, R.D., Stiles, B., Mitchell, K.L., Ostro, S., Soderblom, L., Wood, C., Zebker, H., Wall, S., Janssen, M., Kirk, R., Lopes, R., Paganelli, F., Radebaugh, J., Wye, L., Anderson, Y., Allison, M., Boehmer, R., Callahan, P., Encrenaz, P., Flamini, E., Francescetti, G., Gim, Y., Hamilton, G., Hensley, S., Johnson, W.T.K., Kelleher, K., Muhleman, D., Paillou, P., Picardi, G., Posa, F., Roth, L., Seu, R., Shaffer, S., Vetrella, S., West, R., 2007. The lakes of Titan. *Nature* 445, 61–64. doi:10.1038/nature05438

Tokano, T., 2011. Planetary science. Precipitation climatology on Titan. *Science* 331, 1393–1394. doi:10.1126/science.1204092

Tomasko, M.G., Archinal, B., Becker, T., Bézard, B., Bushroe, M., Combes, M., Cook, D., Coustenis, a, de Bergh, C., Dafoe, L.E., Doose, L., Douté, S., Eibl, a, Engel, S., Gliem, F., Grieger, B., Holso, K., Howington-Kraus, E., Karkoschka, E., Keller, H.U., Kirk, R., Kramm, R., Küppers, M., Lanagan, P., Lellouch, E., Lemmon, M., Lunine, J., McFarlane, E., Moores, J., Prout, G.M., Rizk, B., Rosiek, M., Rueffer, P., Schröder, S.E., Schmitt, B., See, C., Smith, P., Soderblom, L., Thomas, N., West, R., 2005. Rain, winds and haze during the Huygens probe's descent to Titan's surface. *Nature* 438, 765–778. doi:10.1038/nature04126

- Toublanc, D., Parisot P., Brillet, J., Gautier, D., Raulin, F., McKay, C.P., 1995. Photochemical modelling of Titan's atmosphere. *Icarus*.
- Turtle, E.P., Perry, J.E., Hayes, a G., Lorenz, R.D., Barnes, J.W., McEwen, a S., West, R. a, Del Genio, a D., Barbara, J.M., Lunine, J.I., Schaller, E.L., Ray, T.L., Lopes, R.M.C., Stofan, E.R., 2011. Rapid and extensive surface changes near Titan's equator: evidence of April showers. *Science* 331, 1414-1417. doi:10.1126/science.1201063
- Warren, P.H., 2011. Ejecta-megaregolith accumulation on planetesimals and large asteroids. *Meteorit. Planet. Sci.* 46, 53-78. doi:10.1111/j.1945-5100.2010.01138.x
- Warren, P.H., Rasmussen, K.L., 1987. *J. Geophys. Res.* 92, 3453-3465. doi:10.1029/JB092iB05p03453
- Wood, C. a., Lorenz, R., Kirk, R., Lopes, R., Mitchell, K., Stofan, E., 2010. Impact craters on Titan. *Icarus* 206, 334-344. doi:10.1016/j.icarus.2009.08.021
- Yun, T.S., Santamarina, J.C., 2008. Fundamental study of thermal conduction in dry soils. *Granul. Matter* 10, 197-207. doi:10.1007/s10035-007-0051-5

CHAPTER III
INVESTIGATING THE SUPPORT OF TITAN'S LARGE MOUNTAIN PLATEAUS
BY AIRY ISOSTASY

Chapter III will be submitted to the journal Icarus as:

Investigating the Support of Titan's Large Mountain Plateaus by Airy Isostasy
Lauren R. Schurmeier¹, Andrew J. Dombard¹, Jani Radebaugh²

¹Department of Earth and Environmental Sciences, University of Illinois at Chicago, 845 W. Taylor St., Chicago, IL, United States

²Brigham Young University, Provo, UT.

A. Abstract

The varied topography of Titan is unlike anything else seen on icy satellites. Notably, there are two large-scale (200-350 km width) topographic features, which we term “mountain plateaus”. These plateaus are perplexing because all large-scale topography requires a mechanism of support. On Earth, large mountains are supported by Airy isostasy, in which large topographic highs have larger, low-density roots pushing into the denser mantle for buoyant support. On Titan, the roots of mountains would need to be very large to provide buoyant support because of the small density contrast between the outer ice shell and the subsurface ocean. Here, we investigate the long-term stability of Airy isostatic support for these plateaus using finite element modeling under two different thermal structures. Our results show that topographic loads of this scale cannot be supported by Airy isostasy on Titan. Over time, the mountain topography marginally descends, while the mountain root is incredibly unstable and quickly flows away, completely out of isostatic equilibrium. Thus, our simulations show that the plateaus are supported by the lithosphere in an ice-rich crust. We find that the lower ice shell and entire mountain root are unable to transfer significant support to the surface because the temperatures in the lower shell are too close to the melting temperature of ice. This finding also indicates that plateaus of this scale cannot be formed by crustal thickening; the buoyancy of a thickened crust will not transfer to, and therefore lift, the surface. To build these plateaus would require either a lower density material intruded into the surrounding lithosphere (i.e., Pratt isostasy), or the placement of a mountain load on top of or within the lithosphere. One mechanism that can achieve this

result is volcanism, and so we explore the possibility that these plateaus formed through cryovolcanic processes, finding morphological indicators in the form of a putative summit caldera with an emanating flow channel that branches downslope on one of the plateaus.

B. Introduction

For an icy satellite, Titan's topography is surprisingly curious. The topographies of similarly-sized Ganymede and Callisto, along with the other moons of Saturn are dominated largely by impact craters and in some cases large extensional faults and fractures. Quite to the contrary of this trend, regions of high topography, "mountains", and mountain chains were identified early in the Cassini mission in SAR imagery and radarclinometry (Cook-Hallett et al., 2015; Liu et al., 2016a, 2016b; Radebaugh et al., 2007). More recently, several large topographic features were identified in a global topographic map of Titan constructed from interpolated SARTopo and altimetry data (Lorenz et al., 2013). Notably, there are four topographic rises, at least 150 km wide and ~600 m above the surrounding terrain identified in an arc-like shape in the southeastern quadrant of Titan (Fig. 1).

These large, isolated, topographic rises, which we term "mountain plateaus", are perplexing because of what Titan's outer layers are made of: a solid icy crust that overlies a slightly denser liquid water ocean (McCord et al., 2006; Sohl, 2003; Tobie et al., 2005). With the exception of Iapetus and a curious dome on Ganymede (Kay et al., 2018), no other icy satellite currently has large positive topography on its surface. All large-scale topography such as these mountains requires a mechanism of support, and the three end-member forms of large-scale topographic support are: Airy isostasy, Pratt isostasy, and the strength of the lithosphere (Fig. 2).

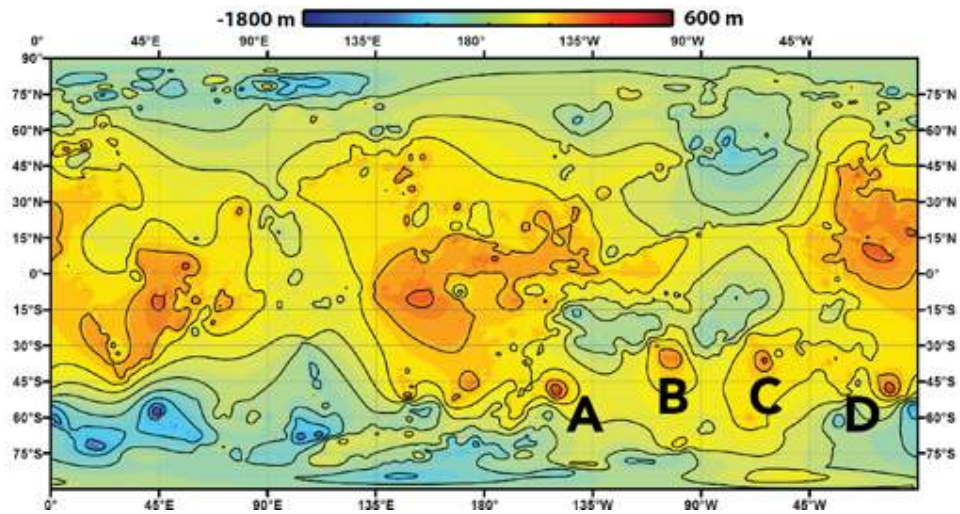


Figure 1: Interpolated topographic map of Titan from Lorenz et al. (2013). The four isolated topographic rises are labeled A, B, C, and D.

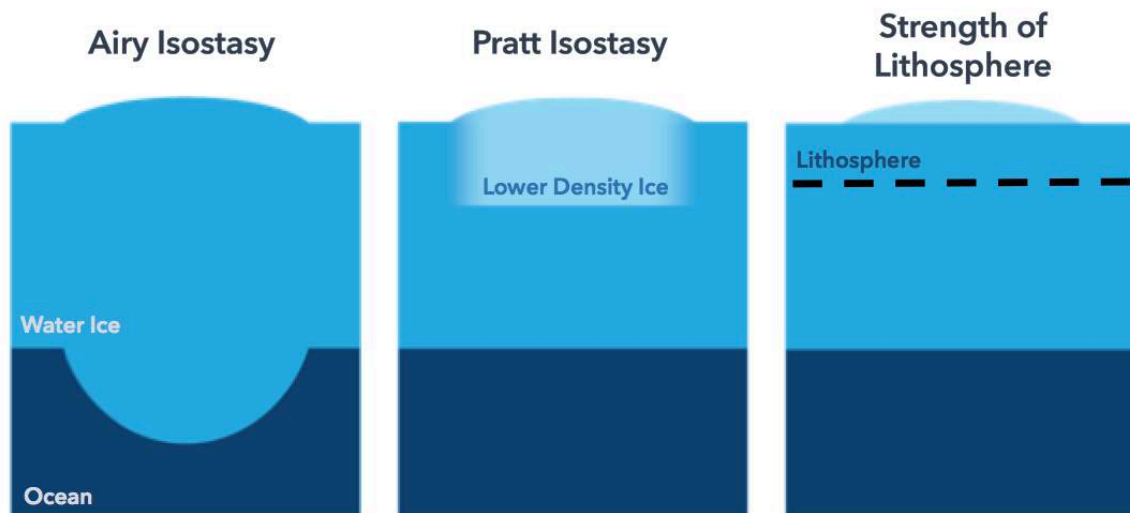


Figure 2: Three end-member forms of large-scale topographic support: Airy isostasy, Pratt isostasy, and the strength of the lithosphere. Not to scale.

On Earth, large mountains are mainly supported by Airy isostasy, in which topographic highs have larger, low-density roots pushing into the denser mantle for buoyant support. On Titan, the roots of mountains would need to be very large to provide buoyant support because of the small density contrast between ice and water. This is completely analogous to the ~10% of an iceberg that stands above the water's surface on Earth, supported by the remaining ~90% of the low-density iceberg protruding into the slightly denser water. A significant issue for the applicability of Airy isostasy in icy satellites is the very nature of an ice shell. Titan is thought to have a rather thick ice shell at its surface, ~100 km thick (Mitri et al., 2014; Nimmo and Bills, 2010). The lower portions of this thick ice shell, and any isostatic roots protruding into the lower ocean, will by definition have warm temperatures approaching the melting point of ice. This means the ice will be viscously weak and should not be able to transfer significant support to the surface, analogous to the evolution of large impact basins on Mars (Karimi et al., 2016). Therefore, mountain roots on Titan may not be able to provide buoyant support for large mountain plateaus.

The second mechanism, Pratt isostasy, has the mountainous region standing higher than the surrounding region because it is made of a lower density material. A lower density ice would protrude higher than the same mass of ice of higher density -relative to the depth of compensation- resulting in a topographic rise.

The third mechanism is simply lithospheric support. This could include a mountainous load placed on the lithosphere, or a load within -or just below- the elastic lithosphere, flexing the overlying material upwards into a mountain plateau shape. For loads placed upon or within the lithosphere, the scale of the topographic load is an important control on whether

the lithosphere can support it. Sufficiently short-wavelength topography causes nearly no deflection of the lithosphere, and the lithosphere can be thought of as infinitely rigid, hence completely supporting the load. Conversely, long-wavelength topography will only have minor support from the lithosphere, collapsing to a state of (Airy) isostatic support (e.g., Turcotte and Schubert, 2002). The mountain plateaus on Titan are at least 150 km wide, so it is not clear if these topographic loads can be supported on Titan where the ice shell is only ~100 km thick and elastic lithosphere must be thinner.

Large mountainous regions on Earth are believed to be supported by some combination of Airy isostasy and lithospheric strength (Turcotte and Schubert, 2002). Both mechanisms could be problematic in the support of the mountain plateaus of Titan. The weak lower ice shell may be ineffective in transferring the buoyancy forces from a root extending into the ocean, while the plateaus may be too broad to receive much support from a lithosphere that must be thinner than the shell. Here, we use finite element simulations to explore the support of these mountain plateaus.

C. Methods

Large plateaus of this scale on icy satellites are unusual, so we first needed to confirm that these four isolated topographic rises (Fig. 1) are in fact mountains and not simply artifacts of interpolation of sparse topographic coverage. We use the Esri ArcGIS software program to view the available Cassini SAR (Synthetic Aperture Radar) imagery, topographic data from SARTopo, or elevation derived from overlapping SAR beams (Stiles et al., 2009) and altimetry (Corlies et al., 2017), and the global interpolated topographic map (Corlies et al., 2017; Lorenz et al., 2013). At the four rises found within the global interpolated topography map, we first examine the SAR imagery for morphological indications of mountainous regions. Mountainous regions on Earth appear radar bright in general, indicating rough surfaces at the radar wavelength (~ 2 cm for *Cassini*). The amount of fluvial dissection and the direction that tributaries branch are also good indications of relative high and low elevations. In addition to morphological clues, we examine any available topographic information in the sparse SARTopo coverage. We use the ArcGIS spatial analyst toolset to plot interpolated topographic profiles of all data present around the plateaus. We examine profiles to determine if the morphological indications of plateaus correlate with the expected topographic profile of a mountain. Once the topographic rises are confirmed to be mountain plateaus, we use the SARTopo data topographic profiles to estimate their heights and widths.

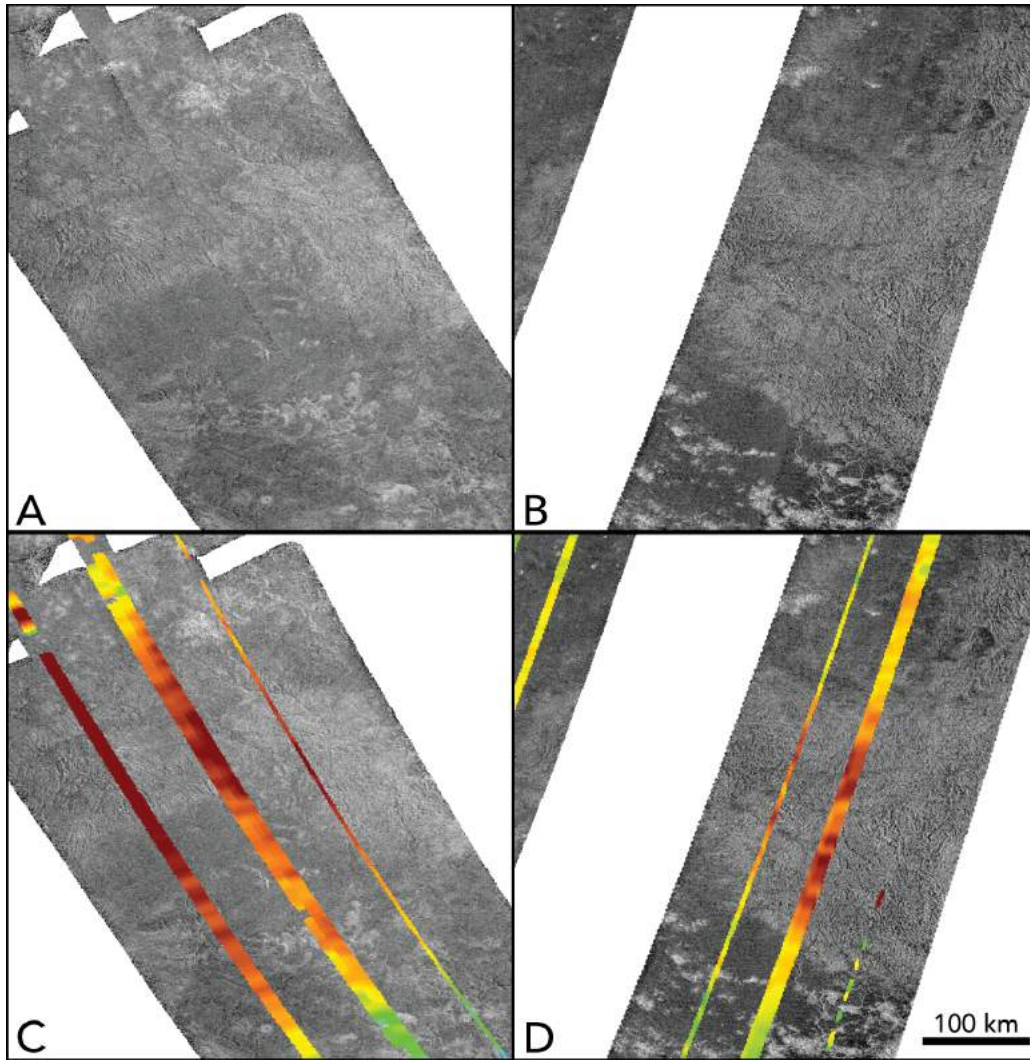


Figure 3: SAR images of the mountain plateaus at location D (left: A, C) and location A (right: B, D) with SARTopo data colorized to indicate high (red) and low (green to blue) elevations. The plateaus are ~600 m tall.

We confirmed that locations A and D (Fig. 3) are in fact large mountain plateaus. They are radar bright and highly dissected throughout the topographic high, and several thin irregular and branching channels appear to originate near their centers and flow downslope. We

interpret many of these as fluvial features because we can see evidence of tributaries feeding into a centralized channel at acute angles. The Strahler channel order increases downslope, as would be expected for fluvial systems that accumulate rainfall from a local region. This is in contrast to lava flows that are distributary, with the Strahler channel order increasing upslope. Using SARTopo data, we estimate that the mountains are ~600 m tall, but we note that they could be taller since the SARTopo data may not exactly cross the summit. Analysis of the morphology indicates that these plateaus are ~200 km wide, while the topographic profiles show the high standing are up to ~350 km wide.

Unlike A and D, location B shows some signs of dissection and radar-bright regions, but they are not localized to the topographic high in the global topography. Plus, the SARTopo data do not show a clear mountain shape, so we interpret this topographic high to be a product of the interpolation. Location C has one strip of altimetry data that is mountain-like; however, it lacks SAR imagery needed for confirmation. We therefore only focus on the plateaus in locations A and D in this work, but recognize that these results could potentially apply to the imagery-free location C.

1. Airy Isostasy Finite Element Modeling

Since most large terrestrial mountain plateaus are supported mainly by Airy isostasy, we investigate the stability of this type of support over time using the MSC.Marc finite element package, which has been used extensively to study lithospheric processes on planets and icy satellites (Dombard and McKinnon, 2006; Karimi et al., 2016; Kay and Dombard, 2018; Schurmeier and Dombard, 2017). The stability of the buoyant support and the mountain roots are examined by looking at how the mountain peak and roots evolve over time, and how the material responds to stresses. The viscoelastic evolution of the mountains is investigated using axisymmetric meshes 5x as wide and 3x as deep as half the mountain width (200 and 350 km), to avoid edge effects (cf. Dombard and McKinnon, 2006). The mesh is divided into two layers: an outer ice shell that is ostensibly 100 km thick (Mitri et al., 2014; Nimmo and Bills, 2010) with a density of $\rho_i = 950 \text{ kg m}^{-3}$, and the ocean below has a density of $\rho_o = 1,050 \text{ kg m}^{-3}$ (Fig. 4). We bias the size of the elements in the vertical direction in order to include more elements toward the surface and ice-ocean interface, where most of the movement occurs. The initial mountain shape is set to either the current height of the mountain plateau ($h = 600 \text{ m}$) or a taller height ($h = 1 \text{ km}$) for comparison. We assume that the plateau and root follow a Gaussian shape, where the plateau half-width, as determined from our measurements above, is defined as the radius where the Gaussian falls to 5% its peak height (standard deviation of the Gaussian of 71 km and 41 km). The maximum thickness of the isostatic root is determined using the density contrast of the ocean and icy plateau, where:

$$H_{\text{root}} = \rho_i h / (\rho_o - \rho_i)$$

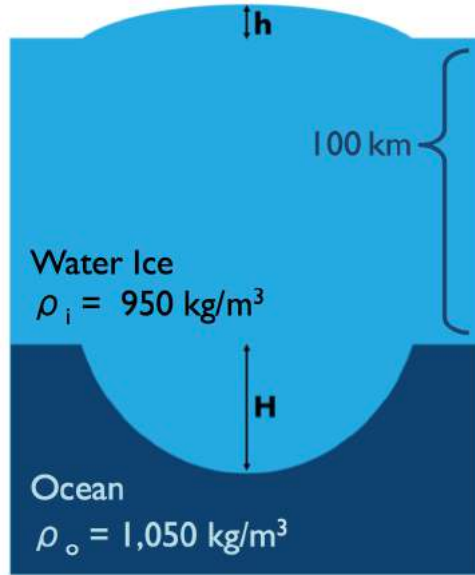


Figure 4: Schematic showing the Airy isostatic mountain. Not to scale.

Our simulations consist of a two-step process: a thermal simulation, then a mechanical simulation. For each plateau, we run two steady-state thermal simulations with different thermal structures. The first uses the assumed current heat flow on Titan of 4 mW m^{-2} (Sohl, 2003), and with an ice shell thickness of $\sim 100 \text{ km}$, the temperature at the base of the ice shell T_b will be 176 K. Implicit in these conditions is that ocean has a water-ammonia eutectic composition, which greatly suppresses the melting point. The second thermal structure assumes that no ammonia is present as antifreeze, so T_b is set 260 K, the melting temperature of ice at 100 km deep in Titan. We apply the required heat flow to get an ocean without antifreeze at 100 km depth is $q = 6.6 \text{ mW m}^{-2}$. All simulations have a locked surface

temperature of 94 K (the current surface temperature), and the base of the ice shell (including the base of the root) is locked to the ocean temperature. Basal heat flows are applied to the base of the mesh, and no heat is allowed to pass through the side edges. Water ice exhibits a temperature-dependent thermal conductivity, $k = 651/T$ (Petrenko and Whitworth, 1999), which we apply here.

After the thermal state is determined, we perform a mechanical simulation to track the evolution of the surface and root topography. We set uniform material properties through the mesh for both the water ice and liquid water using a Maxwell viscoelastic rheology. For the elastic response, we use the properties of water ice from Gammon et al., (1983) and the ductile creep flow laws of Goldsby and Kohlstedt (2001), assuming a grain size of 1 mm. The Young's modulus and Poisson's ratio of ice are 9.332 GPa and 0.325, respectively; however with this value of Poisson's ratio, the materials are compressible under Titan's gravity (gravitational acceleration of 1.35 m s^{-2}). To prevent unwanted gravitational self-compaction, we set the Poisson's ratio near its incompressible limit ($1/2$), but scale the Young's modulus to keep the flexural rigidity constant (for substantiation of this approach, see Dombard et al., 2007; Karimi et al., 2016). We apply full large-strain deformation and enforce constant dilatation across each element to prevent errors that can arise in the simulation of nearly incompressible behavior.

The water that underlies the ice shell provides a buoyant restoring force but not any resistance from material strength. In essence, the water's viscosity is so low relative to the viscosity of the ice at the base of the ice shell that the water simply moves to accommodate the deforming ice. The phenomenon can be leveraged in how we simulate the water,

because the rheological behavior of the water simply needs to allow the water to move at least as fast as the deforming ice. Consequently, we can apply the same material properties to the water as we do to the overlying ice, except for the water's higher density. Simulations using a lower viscosity for the water show negligible differences, justifying this approach.

Time stepping is automatically controlled to resolve the minimum viscoelastic Maxwell time in the mesh by a factor of 4 or greater. We implement a minimum viscosity in the mesh of 10^{18} Pa s to keep run times reasonable. Viscosity values below this cut-off only occur far from the lithospheric deformation that we are interested in, and we have confirmed our results are not sensitive to this cut-off value. The nodes of the mesh are locked along the base in both vertical and horizontal directions, and we apply free-slip boundary conditions to the side edges of the mesh, which restrict normal displacements but permit transverse displacements. Each simulation is run for a simulated time of 3 Gyr. If the plateau surface topography and roots are stable over time (i.e., limited deformation), this result indicates that buoyancy in the ice in the deep shell can support stresses over long time scales, and Airy isostasy is a plausible mechanism of support for the large mountain plateaus on Titan. To confirm the effects of buoyant support, we run these thermal simulations again but with only ice (no ocean or root) and therefore no density contrast. We maintain the same temperature structure (i.e. locked surface temperature and ocean-interface temperature).

Additionally, we explore the idea that these features are supported in a methane clathrate hydrate crust and lithosphere. Methane clathrate hydrate has been hypothesized to be present in significant quantities in Titan's ice shell as a source to replenish Titan's atmospheric methane (Choukroun et al., 2010; Choukroun and Sotin, 2012; Tobie et al.,

2006). To do this, we first explore an all methane clathrate hydrate mesh, applying its low thermal conductivity k of $0.5 \text{ W m}^{-1}\text{K}^{-1}$ (Krivchikov et al., 2005) and a ductile creep law of methane clathrate hydrate (Durham et al., 2003). Second, we examine a case with the thermal effects of a surficial layer of methane clathrate hydrate (2 km) on a mechanically all-water ice mesh. For this case, we employ a surface temperature that is the temperature that would be found under a methane clathrate hydrate layer that is 2 km thick, h , at Titan's current heat flow, q . This effective temperature is $T_e = T_s + qh/k$, where T_s is the current surface temperature of 94 K. These simulations serve as a comparison with our water ice simulations. Methane clathrate hydrate is known to be considerably stronger than water ice at the same temperature (Durham et al., 2003), but the low thermal conductivity may actually prevent the formation of thick, strong lithospheres on Titan, and result in poor mountain support.

D. Results

For all simulations, our results show that Airy isostasy is not an adequate mechanism of support for large mountainous plateaus on Titan. Here we show the results of our finite element simulations. Each graph compares the evolution of the topography of the mountain plateau or root under different conditions on each side of the y-axis. Each individual curve is a topographic profile from a specified time step and is axisymmetric about the plateau center (y-axis).

The simulations that include initial buoyant support show that the isostatic root is incredibly unstable and quickly flows away into a negligible size (Fig. 5). For both sizes of plateau, the surface topography minimally sags as the lithosphere responds to the imposed load at the current basal heat flow of 4 mW m^{-2} . Unsurprisingly, the higher heat flow of 6.6 mW m^{-2} results in a greater amount of elevation loss for both plateaus due to the fact that viscous flow is strongly controlled by the thermal structure of the ice, and ice closer to its melting temperature (greater homologous temperatures) flows more easily. Most importantly, the rates of change of the topography of the surface and the root are not in synch and completely out of isostatic equilibrium. For example in a mere 1 Myr, the 200 km wide plateau's surface topography at a heat flow of 4 mW m^{-2} descended only ~40 m at its peak, while the root ascended ~760 m. If the root and surface topography were in isostatic equilibrium, then the root would have ascended only ~380 m, half the ascent observed (Fig. 6). After 1 Gyr, this isostatic disequilibrium is exacerbated, with the surface topography descending only ~110 m while the root ascends ~4,580 m. Isostatic equilibrium would

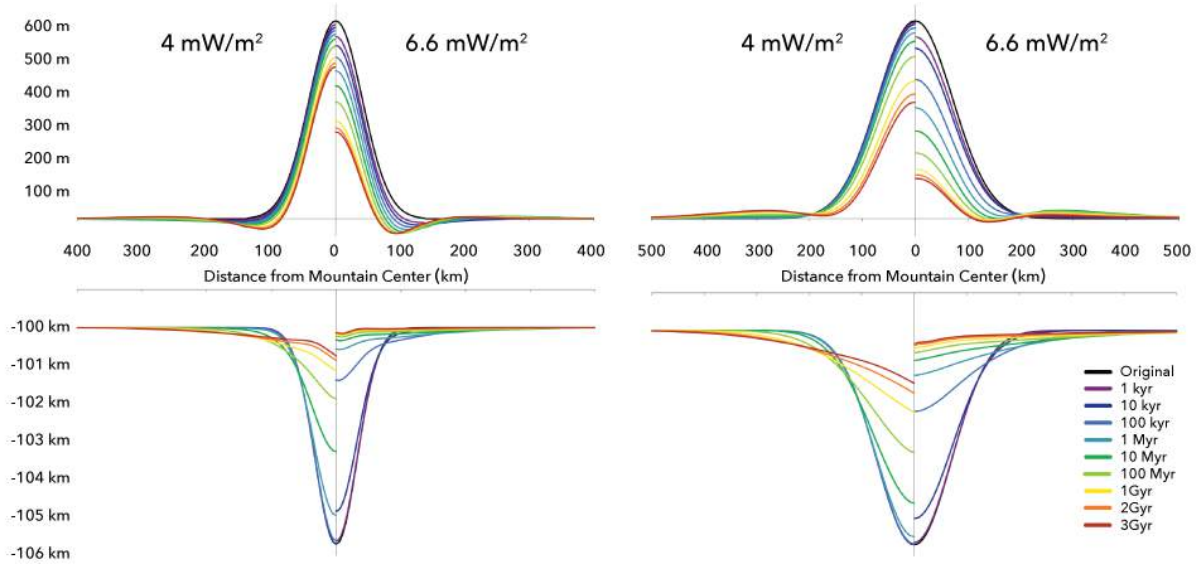


Figure 5: Viscoelastic evolution of the surface topography (top) and base of the ice shell and mountain root (bottom), with an initial mountain height of 600 m. The 200 km wide plateau is on the left, and the 350 km wide plateau is on the right. Each plot compares a thermal structure using a basal heat flow of 4 mW m^{-2} (left side of y-axis) and 6.6 mW m^{-2} (right side of y-axis).

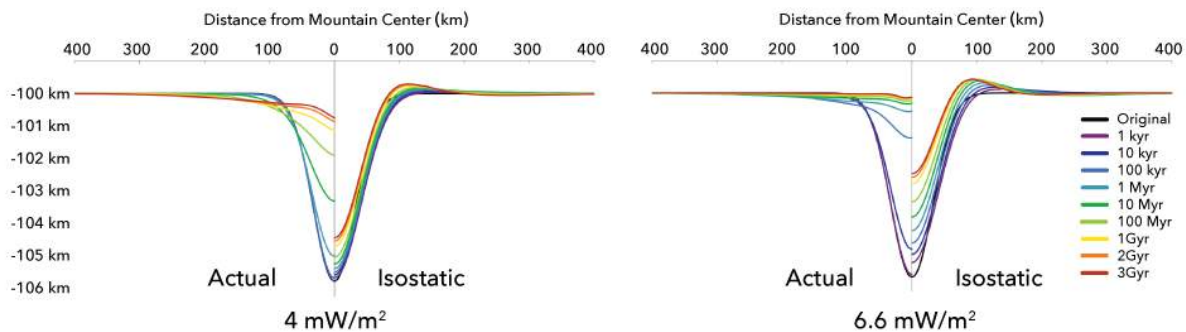


Figure 6: Comparison of the evolution of the simulated root topography (left side of y-axis) and the ideal topographic profiles of a root in isostatic equilibrium with the simulated surface topography (right side of y-axis) for heat flows of 4 mW m^{-2} (left) and 6.6 mW m^{-2} (right).

require only a change of $\sim 1,050$ m. By 3 Gyr, the removal of the root has stabilized because it is essentially gone, but is $\sim 3,630$ m short of isostatic equilibrium. Likewise, the simulations starting with an initial height of 1 km show similar evolutions (Fig. 5, Fig. 7). The surface sinks slightly over time while the root quickly ascends, completely out of isostatic equilibrium. When normalized, the evolution of the topography for initial heights of 600 m and 1 km are nearly identical in terms of surface height, and only differ slightly in width (Fig. 8). The 350 km wide plateau simulations show similar evolutions (Fig. 5, Fig. 7), with the main difference being the increased overall change in height of the plateau and root, and a slightly more pronounced flexural bulge at in the last few billion years. This difference is expected because larger wavelength features are expected to deform more easily and are less supported by the lithosphere.

To ascertain the effects of buoyant support, we compare simulations that include an ocean-shell density contrast and an isostatic root (buoyant support), to those with an all-ice mesh with the density of ice (no buoyant support). We find that there is very little difference between the simulations with and without buoyant support for the 200 km plateau at both heat flows (Fig. 9). The larger, 350 km plateau displays one notable difference, initially the plateaus with no buoyant support falls ~ 90 m more for the 4 mW m^{-2} heat flow (~ 150 m for the 6.6 mW m^{-2} heat flow), but it then evolves essentially the same as the simulations that include buoyant support.

Finally, we compare our results in a purely water ice shell with those that include methane clathrate hydrates. We find that a purely methane clathrate ice crust does not support mountain loads of this scale. The plateaus are unstable and quickly relax into

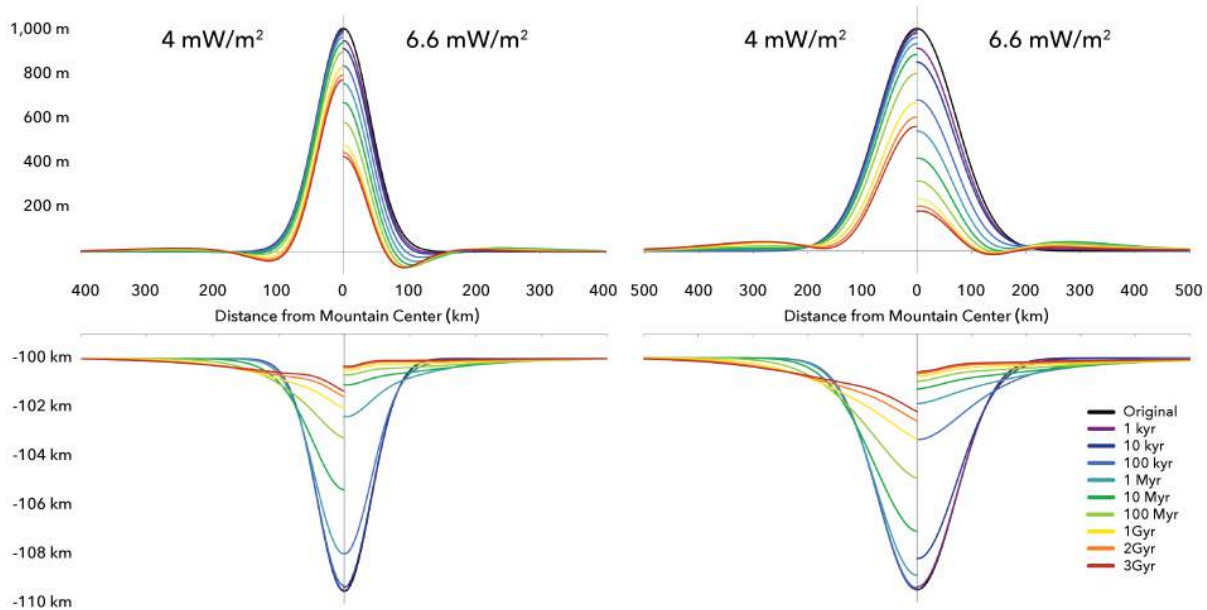


Figure 7: Viscoelastic evolution of the surface topography (top) and base of the ice shell and mountain root (bottom), with an initial mountain height of 1,000 m. The 200 km wide plateau is on the left, and the 350 km wide plateau is on the right. Each plot compares a thermal structure using a basal heat flow of 4 mW m^{-2} (left side of y-axis) and 6.6 mW m^{-2} (right side of y-axis).

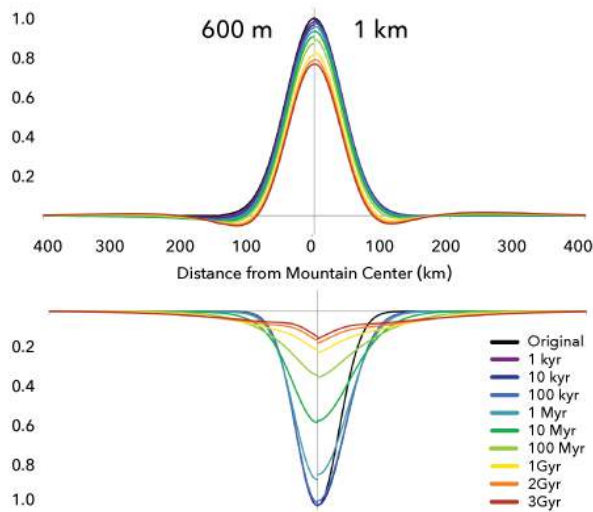


Figure 8: Normalized comparison for the 200 km mountain plateau at 4 mW m^{-2} for initial heights of 600 m (left side of y-axis) and an initial height of 1 km (right side of the y-axis).

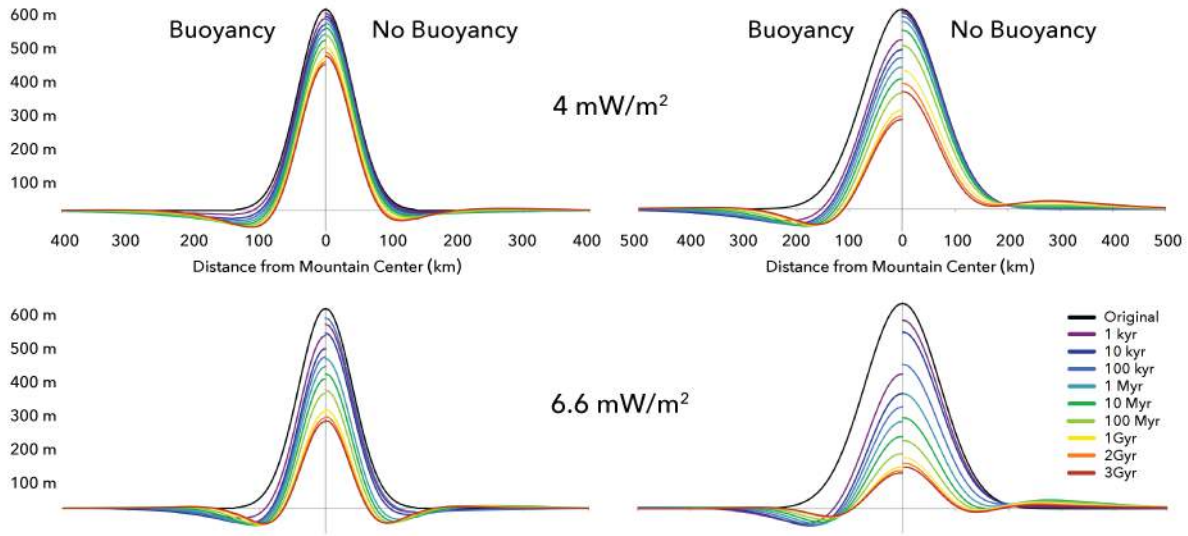


Figure 9: A comparison of the simulated viscoelastic evolution the plateau surface topography without buoyant support (left side of y-axis) and with buoyant support (right side of y-axis) for thermal structures using a basal heat flow of 4 mW m^{-2} (left) and 6.6 mW m^{-2} (right). The top two plots are for 200 km wide plateau, and the bottom two are for 350 km wide plateau.

significantly shorter features, while the same feature composed of pure ice is relatively stable over time (Fig. 10). We also explore the thermal effects of a relatively warmer surface temperature due to the presence of a relatively thin surficial methane clathrate hydrate layer. The effective surface temperature increase due to a 2 km low thermal conductivity layer results in significantly warmer ice, which more readily deforms. While methane clathrate hydrates may be stronger than pure ice at the same temperatures, the thermal effect of the low thermal conductivity methane clathrate hydrate dominates, resulting in mountains that are too warm to be stable as topographic loads and relax away over time.

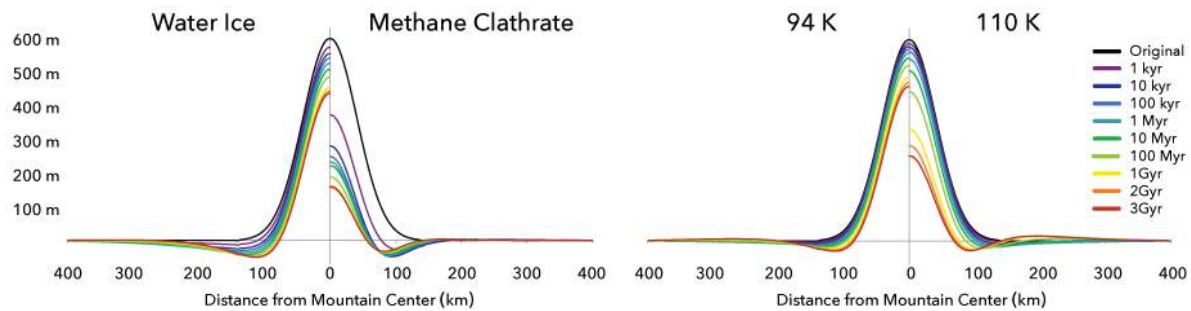


Figure 10: Comparison of the evolution of a 200 km plateau at 4 mW m^{-2} in an all water ice mesh (left plot - left side of y-axis), an all methane clathrate mesh (left plot, right side of y-axis) with the current surface temperature (94 K). On the right is a comparison of a normal water ice mesh at 94 K (left), and a water ice mesh with the thermal effect of a 2 km (110 K surface temperature).

E. Discussion

Our results indicate that mountain plateaus of this scale on Titan cannot be supported by Airy isostasy. The simulations with an isostatic root protruding into a denser ocean show that the root is incredibly unstable. The root flows and disappears over time at a rate far greater than the surface topography sags, and is completely out of isostatic equilibrium. Plus, our simulations with and without the root and buoyant support from a denser subsurface ocean show very little differences. Together, these results tell us that the root is not communicating with the surface. The lower portions of the ice shell and the entire root are close enough to the melting temperature of ice that they are viscously weak and therefore cannot transfer significant support to the upper ice shell and surface. Instead, the surface topography in our simulations is only supported by the strength of the mechanically stronger outer layer of the ice, the lithosphere.

We can see that it is indeed the lithosphere supporting these mountain plateaus through the differences between the topographic evolutions of the plateaus of different scales. The rate of descent of the 350 km wide plateau is notably greater than that of the 200 km wide plateau (Fig. 5, Sup. Fig. 2). For a given heat flow and time, the thickness of the lithosphere will remain the same, but the longer wavelength feature will sag more because of the wavelength dependence of a flexing lithosphere (cf. Turcotte and Schubert, 2002). Thus, the topography of the longer wavelength plateau can descend more easily. The initial height of the plateau makes very little difference on the evolution; the normalized change is similar between the two (Fig. 8). This is another indication that this is a lithospheric support; the

amplitude of the load matters very little, while the wavelength of the feature has a more notable effect on the degree of support.

The thickness of the lithosphere can be identified in our simulations as well. A profile of differential (radial minus vertical) stress with depth under the mountain load can serve as a proxy for the extent of the lithosphere; the peak differential stress in the subsurface should mark the approximate thickness of the lithosphere because beneath this point, the material responds to stress by flowing ductily. For the 350 km mountain load at the current heat flow, this depth is around 45 to 25 km for 1 to 100 Myr (Fig. 11), with a thickness that decays with time because of progressive creep at the base of the lithosphere (cf. Damptz and Dombard, 2011).

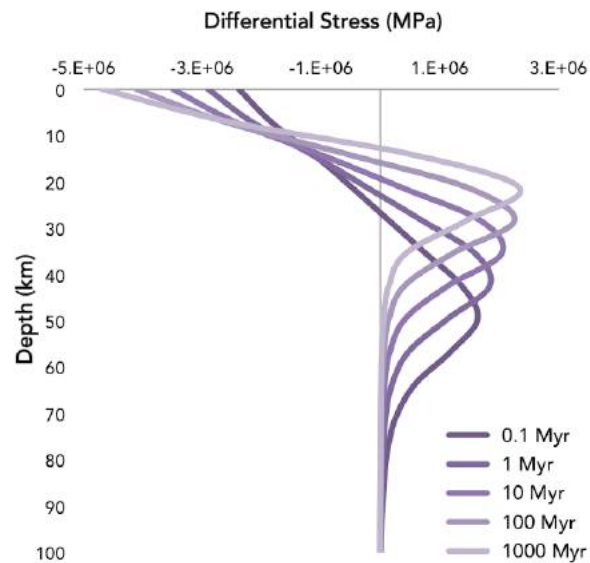


Figure 11: Profile of differential stress at depth over time for the 350 km mountain load with basal heat flow 4 mW m^{-2} , directly under the mountain center. The peak depth of the differential stress is a decent proxy for the thickness of the lithosphere.

A mesh composed of methane clathrate hydrates or even the presence of a surficial layer of clathrates (effective surface temperature increase) drastically changes the thermal structure of the near-surface ice such that mountains of this scale cannot be supported by Airy isostasy nor even Titan's lithosphere. Methane clathrate hydrate is so thermally insulating that the significantly warmer ice shell constrains the brittle behavior of the icy shell to much shallower depths, and renders the lithosphere much thinner relative to a purely water ice shell. Lithospheric support scales with the thickness of the lithosphere; hence a methane clathrate hydrate-dominated surface cannot support plateaus of this scale or larger. This result is important because it limits the availability of methane clathrate hydrate as a reservoir for atmospheric methane replenishment. Our finding suggests that in these locations methane clathrate hydrate cannot dominate the composition of the icy crust in the near surface during the lifetimes of these features. Atmospheric replenishment by release from clathrates may need to be confined to a small (< 2 km) surficial layer in these regions, only occur elsewhere (i.e., the polar regions), or perhaps methane replenishment must come from another source altogether. A second implication of the thermal effects of methane clathrate hydrate is that the presence or absence of methane clathrate hydrate could greatly affect not only the lithospheric thickness of Titan's ice shell, but also the thickness of the ice shell itself. It has been noted that the difference in Titan's ice shell thickness may be vast between the equator and the pole, which has been attributed to differing amounts of tidal heating (e.g., Nimmo and Bills, 2010). While this is outside of the scope of this paper, we suggest that another origin for this planet-wide topographic differential may be an uneven distribution of

methane clathrate hydrates, where the presence of clathrates at the poles results in a locally thinner lithosphere and ice shell.

The differences in the evolution of the topography at different heat flow values demonstrate that large features of this scale are much more susceptible to deformation at heat flows greater than the current expected value of 4 mW m^{-2} . Heat flow can vary spatially and temporally, so these results may indicate that in these particular locations within Titan's mid-latitudes, the basal heat flow has not exceeded the 4 mW m^{-2} within the plateaus' lifetimes. Alternatively, if these plateaus experienced a significant amount of time at a higher heat flow of at least 6.6 mW m^{-2} , or more than a few hundred million years at the current heat flow, then these features may require a larger initial height to currently be at the height of $\sim 600 \text{ m}$.

The inability of Airy isostasy to support these features means that even larger features will also not be supported. Through primarily morphology, we have identified another potential mountain plateau with some similarities to those at locations A and D, located west of location A (Fig. 1). In SAR imagery, it has a highly dissected texture, channels that we interpret as fluvial features flowing downslope and some sparse SARTopo data that implies that it is at least 600 m above the background elevation (Fig. 12). Unfortunately, it appears that much of this feature falls between two SAR images, and the limited SARTopo data only appear to graze the side of the feature, so we do not truly know the scale of this feature in terms of area or elevation. Regardless, this feature, the two confirmed mountain plateaus at locations A and D, and possibly the un-imaged topographic rise at location C are all examples of features that cannot be supported by Airy isostasy.

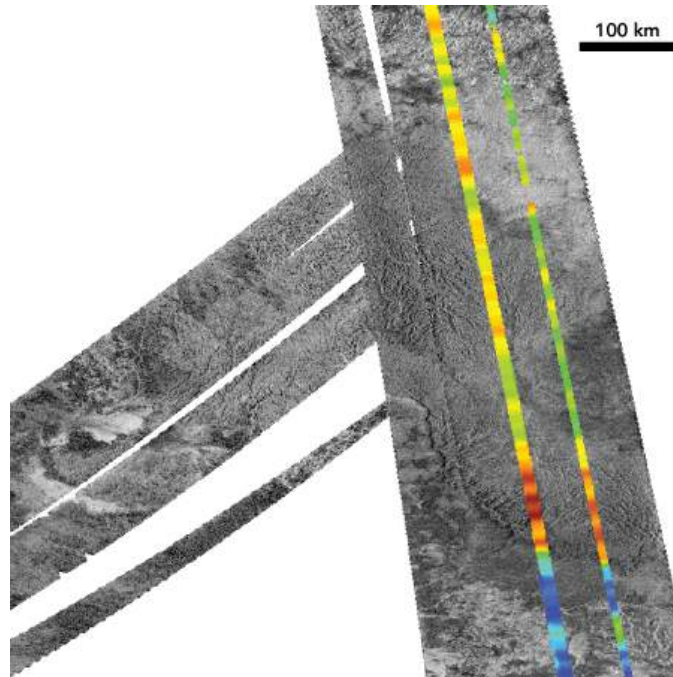


Figure 12: A large feature with limited SARTopo coverage. The maximum height is at least 600 m above the background elevation. It is morphologically similar to the other plateaus and may be an example of a wider plateau on Titan. SARTopo data are colorized to indicate high (red) and low (blue) elevations.

Since the mountain plateaus and mountain roots are not stable over geologic timescales when supported by Airy isostasy, an important corollary is that the mountains of this scale cannot be formed through crustal thickening or pushed up from below the lithosphere. To build these plateaus would require either a lower density material than the

surrounding region (i.e., Pratt isostasy), or the mountain load was placed on top of or within the lithosphere. Both ideas could result from cryovolcanic processes: injection of clean ice into a dirty ice shell, intrusive cryovolcanism (e.g., a large scale laccolith), or eruption onto the surface. Consequently, we visually inspect the radar imagery at both locations for morphological signs of extrusive cryovolcanism. The plateau at location A did not show any obvious signs, aside from the fact that the feature is isolated and elevated above the surroundings and has morphologies consistent with being soft, having badlands-style erosion (Fig. 3). This characteristic could be interpreted as an icy volcanism equivalent to pyroclastically deposited material (cryoclastic?). Similar textures are present at the plateau at location D; in addition, this location appears to have a large, flow-like feature emanating from a circular feature near the summit (Fig. 13). We interpret the channel as cryovolcanic rather than fluvial because the channel appears significantly wider and deeper than other surrounding, putatively fluvial channels (Burr et al., 2013). The morphology is also more consistent with an eruptive flow; it originates from a single source (the near summit circular feature that could be a summit caldera) that later fans outwards downslope into distributaries (Fig. 13). Even at this resolution, we can see that the Strahler channel order increases upslope, as seen in most unconfined lava flows (i.e. Dietterich and Cashman, 2014). This is in contrast to the thinner channels found elsewhere on Titan (including a few notable examples at location A). The thinner (fluvial) channels on Titan have tributaries that feed in at acute angles and have an increasing Strahler channel order downslope. Therefore, we interpret these thinner features on Titan as river networks fed by precipitation from a larger region (not a point source), and this larger channel feature located on the dome (Fig. 13) as an eruptive

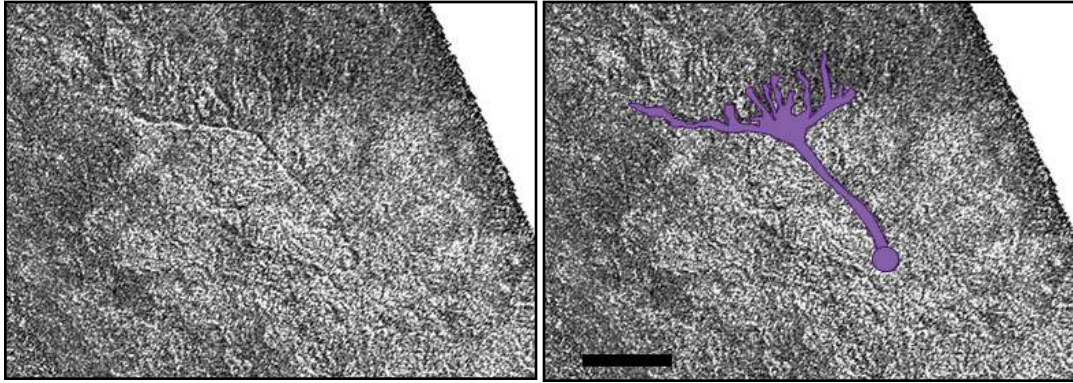


Figure 13: Possible cryovolcanic “caldera” and flow at location D. The scale bar is 25 km wide.

flow from a point source. This morphological evidence, along with our modeling, suggests a possibly cryovolcanic origin. The scale of these features is on par with the recently discovered cryovolcanic candidates on Pluto, Wright and Piccard Mons (Moore et al., 2016). While key differences between the two worlds clearly exist (surface gravity, surface material properties, thermal histories), it is interesting to note how similar the features are in width. Pluto’s putative cryovolcanic features are ~150 - 230 km wide and 4 - 6 km tall, while Titan’s are 200 - 350 km wide and ~0.6 km tall. On Titan, cryovolcanic features of this scale have been long searched for and debated (Lopes et al., 2013; Moore and Pappalardo, 2011), and our study may have identified a new type of cryovolcanic feature on Titan, possibly analogous to shield volcanoes on the terrestrial planets.

In contrast, however, the near-infrared spectral signature of these features, according to interpretation of data from Cassini Visual and Infrared Mapping Spectrometer (VIMS) data

and RADAR emissivity data (Janssen et al., 2016) indicates that their surfaces are not predominately composed of water ice, but instead organic-rich materials. If these features are in fact cryovolcanic edifices, then they must either be ancient enough to have a surficial layer of organics (from the organic hazes presumed to fall from the atmosphere), or the cryovolcanic magma itself incorporated organics, at least at the surface. Alternatively, these features could form as intrusive cryovolcanism below an organic-rich sedimentary layer, or they may simply be the eroded remnants of thick, organic-rich sedimentary structures. We believe that the latter is less likely, because it would be a great coincidence that at least two different locations (and possibly more) on a planetary body eroded into similar-scale, dome-like features. It is also unclear where all of the surrounding material that may have made up a larger sedimentary unit ended up, especially considering that the contact between the plateau and surrounding Undifferentiated Plains shows no gradational transition, as would be expected for one material physically eroding into another.

F. Conclusions

We have confirmed two large topographic rises in Titan's mid-latitudes, which we term "mountain plateaus". The scale of these features is unprecedented on Titan, and the topography of these large features requires a mechanism of support. Since most large mountain plateaus on Earth are supported mainly by Airy isostasy, we have used finite element simulations to determine if these plateaus could be supported by Airy isostasy, despite Titan's large ice shell thickness and the low-density contrast between the ice shell and subsurface ocean. We have simulated the evolution of the two sizes of mountain plateaus, (200 km and 350 km wide, 600 m tall), with thermal structures at or above the current expected basal heat flux, at two different initial heights, and also have compared simulations with and without buoyancy effects.

In all of our simulations, we find that the Airy isostatic roots are incredibly unstable and quickly flow away, completely out of isostatic equilibrium with the evolution of the surface topography. This result, in addition to the result that plateaus modeled with buoyancy effects show very similar deformation to the plateaus simulated without buoyancy effects, prove that buoyant support is not being transferred from the root to the surface. The lower portion of the ice shell and the root are too close to the melting temperature of ice, making it too viscously weak to transfer significant buoyant support to the surface. Our results also suggest that at least in these regions, methane clathrate hydrate cannot dominate the composition of Titan's upper crust. The low thermal conductivity of methane clathrate hydrate results in a lithosphere that is too warm and therefore too thin to support features of this scale.

Furthermore, our conclusions mean that mountain plateaus of this scale cannot be formed through crustal thickening or pushed up from below the lithosphere. Instead, these features most likely formed as a lower-density material rising higher than the surrounding denser regions (i.e., Pratt isostasy), or the placement of a mountain load on top of or within the water ice lithosphere. We suggest that both options could have resulted from intrusive or extrusive cryovolcanic processes. Additionally, we have identified potential morphological indicators of cryovolcanism (a summit caldera with emanating flow channel) on one of the plateaus. If these mountain plateaus are indeed cryovolcanic in origin, they represent a new class of putative cryovolcanic feature and imply a large degree of cryovolcanism that has thus far been unidentified on Titan.

G. Works Cited:

- Burr, D.M., Taylor Perron, J., Lamb, M.P., Irwin, R.P., Collins, G.C., Howard, A.D., Sklar, L.S., Moore, J.M., Ádámkovics, M., Baker, V.R., Drummond, S. a., Black, B. a., 2013. Fluvial features on Titan: Insights from morphology and modeling. *Bull. Geol. Soc. Am.* 125, 299-321. doi:10.1130/B30612.1
- Choukroun, M., Grasset, O., Tobie, G., Sotin, C., 2010. Stability of methane clathrate hydrates under pressure: Influence on outgassing processes of methane on Titan. *Icarus* 205, 581-593. doi:10.1016/j.icarus.2009.08.011
- Choukroun, M., Sotin, C., 2012. Is Titan's shape caused by its meteorology and carbon cycle? *Geophys. Res. Lett.* 39, 1-5. doi:10.1029/2011GL050747
- Cook-Hallett, C., Barnes, J.W., Kattenhorn, S.A., Hurford, T., Radebaugh, J., Stiles, B., Beuthe, M., 2015. Global contraction/expansion and polar lithospheric thinning on Titan from patterns of tectonism. *J. Geophys. Res. E Planets* 120, 1220-1236. doi:10.1002/2014JE004645
- Corlies, P., Hayes, A.G., Birch, S.P.D., Lorenz, R., Stiles, B.W., Kirk, R., Poggiali, V., Zebker, H., less, L., 2017. Titan's Topography and Shape at the End of the Cassini Mission. *Geophys. Res. Lett.* 44, 11,754-11,761. doi:10.1002/2017GL075518
- Damptz, A.L., Dombard, A.J., 2011. Time-dependent flexure of the lithospheres on the icy satellites of Jupiter and Saturn. *Icarus* 216, 86-88. doi:10.1016/j.icarus.2011.07.011
- Dietterich, H.R., Cashman, K. V., 2014. Channel networks within lava flows: Formation, evolution, and implications for flow behavior. *J. Geophys. Res. Earth Sci.* 119, 1704-1724. doi:10.1002/2014JF003103
- Dombard, A.J., McKinnon, W.B., 2006. Elastoviscoplastic relaxation of impact crater topography with application to Ganymede and Callisto. *J. Geophys. Res. E Planets* 111, 1-22. doi:10.1029/2005JE002445
- Durham, W.B., Kirby, S.H., Stern, L.A., Zhang, W., 2003. The strength and rheology of methane clathrate hydrate. *J. Geophys. Res. Solid Earth* 108, 1-11. doi:10.1029/2002JB001872
- Gammon, P.H., Kieft, H., Clouter, M.J., 1983. Elastic Constants of Ice By Brillouin. *J. Phys. Chem.* 87, 4025-4029. doi:10.1021/j100244a004
- Goldsby, D.L., Kohlstedt, D.L., 2001. Superplastic deformation of ice: Experimental observations. *J. Geophys. Res. Solid Earth* 106, 11017-11030. doi:10.1029/2000JB900336

- Janssen, M.A., Le Gall, A., Lopes, R.M., Lorenz, R.D., Malaska, M.J., Hayes, A.G., Neish, C.D., Solomonidou, A., Mitchell, K.L., Radebaugh, J., Keihm, S.J., Choukroun, M., Leyrat, C., Encrenaz, P.J., Mastrogiuseppe, M., 2016. Titan's surface at 2.18-cm wavelength imaged by the Cassini RADAR radiometer: Results and interpretations through the first ten years of observation. *Icarus* 270, 443–459. doi:10.1016/j.icarus.2015.09.027
- Karimi, S., Dombard, A.J., Buczkowski, D.L., Robbins, S.J., Williams, R.M., 2016. Using the viscoelastic relaxation of large impact craters to study the thermal history of Mars. *Icarus* 272, 102–113. doi:10.1016/j.icarus.2016.02.037
- Kay, J.P., Dombard, A.J., 2018. Formation of the bulge of Iapetus through long-wavelength folding of the lithosphere. *Icarus* 302, 237–244. doi:10.1016/j.icarus.2017.10.033
- Kay, J.P., Schenk, P.M., Dombard, A.J., McKinnon, W.B., 2018. The 3-km High Subjovian Megadome on Ganymede: Simulation of Stability via Pratt Isostasy, in: LPSC. p. No. 2083
- Krivchikov, a. I., Gorodilov, B.Y., Korolyuk, O. a., Manzhelii, V.G., Conrad, H., Press, W., 2005. Thermal conductivity of methane-hydrate. *J. Low Temp. Phys.* 139, 693–702. doi:10.1007/s10909-005-5481-z
- Liu, Z.Y.C., Radebaugh, J., Harris, R. a., Christiansen, E.H., Neish, C.D., Kirk, R.L., Lorenz, R.D., 2016a. The tectonics of Titan: Global structural mapping from Cassini RADAR. *Icarus* 270, 14–29. doi:10.1016/j.icarus.2015.11.021
- Liu, Z.Y.C., Radebaugh, J., Harris, R. a., Christiansen, E.H., Rupper, S., 2016b. Role of fluids in the tectonic evolution of Titan. *Icarus* 270, 2–13. doi:10.1016/j.icarus.2016.02.016
- Lopes, R.M.C., Kirk, R.L., Mitchell, K.L., Legall, a., Barnes, J.W., Hayes, a., Kargel, J., Wye, L., Radebaugh, J., Stofan, E.R., Janssen, M. a., Neish, C.D., Wall, S.D., Wood, C. a., Lunine, J.I., Malaska, M.J., 2013. Cryovolcanism on Titan: New results from Cassini RADAR and VIMS. *J. Geophys. Res. E Planets* 118, 416–435. doi:10.1002/jgre.20062
- Lorenz, R.D., Stiles, B.W., Aharonson, O., Lucas, A., Hayes, A.G., Kirk, R.L., Zebker, H. a., Turtle, E.P., Neish, C.D., Stofan, E.R., Barnes, J.W., 2013. A global topographic map of Titan. *Icarus* 225, 367–377. doi:10.1016/j.icarus.2013.04.002
- McCord, T.B., Hansen, G.B., Buratti, B.J., Clark, R.N., Cruikshank, D.P., D'Aversa, E., Griffith, C. a., Baines, E.K.H., Brown, R.H., Dalle Ore, C.M., Filacchione, G., Formisano, V., Hibbitts, C. a., Jaumann, R., Lunine, J.I., Nelson, R.M., Sotin, C., 2006. Composition of Titan's surface from Cassini VIMS. *Planet. Space Sci.* 54, 1524–1539. doi:10.1016/j.pss.2006.06.007
- Mitri, G., Meriggiola, R., Hayes, A., Lefevre, A., Tobie, G., Genova, A., Lunine, J.I., Zebker, H., 2014. Shape, topography, gravity anomalies and tidal deformation of Titan. *Icarus* 236, 169–177. doi:10.1016/j.icarus.2014.03.018

- Moore, J.M., McKinnon, W.B., Spencer, J.R., Howard, A.D., Schenk, P.M., Beyer, R.A., Nimmo, F., Singer, K.N., Umurhan, O.M., White, O.L., Stern, S.A., 2016. The geology of Pluto and Charon through the eyes of New Horizons. *Science* (80-.). 351, 1284-1294.
- Moore, J.M., Pappalardo, R.T., 2011. Titan: An exogenic world? *Icarus* 212, 790-806.
doi:10.1016/j.icarus.2011.01.019
- Nimmo, F., Bills, B.G., 2010a. Shell thickness variations and the long-wavelength topography of Titan. *Icarus* 208, 896-904. doi:10.1016/j.icarus.2010.02.020
- Nimmo, F., Bills, B.G., 2010b. Shell thickness variations and the long-wavelength topography of Titan. *Icarus* 208, 896-904. doi:10.1016/j.icarus.2010.02.020
- Petrenko, V.F., Whitworth, R.W., 1999. *Physics of Ice*. Oxford University Press, Oxford.
- Radebaugh, J., Lopes, R.M.C., Lunine, J.I., Kirk, R.L., Wall, S.D., Stofan, E.R., Lorenz, R.D., 2007. Mountains on Titan observed by Cassini Radar. *Icarus* 192, 77-91.
doi:10.1016/j.icarus.2007.06.020
- Schurmeier, L.R., Dombard, A.J., 2017. Crater relaxation on Titan aided by low thermal conductivity sand infill. *Icarus*. doi:10.1016/j.icarus.2017.10.034
- Sohl, F., 2003. Interior structure models and tidal Love numbers of Titan. *J. Geophys. Res.* 108, 1-13. doi:10.1029/2003JE002044
- Stiles, B.W., Hensley, S., Gim, Y., Bates, D.M., Kirk, R.L., Hayes, A., Radebaugh, J., Lorenz, R.D., Mitchell, K.L., Callahan, P.S., Zebker, H., Johnson, W.T.K., Wall, S.D., Lunine, J.I., Wood, C. a., Janssen, M., Pelletier, F., West, R.D., Veeramacheneni, C., 2009. Determining Titan surface topography from Cassini SAR data. *Icarus* 202, 584-598.
doi:10.1016/j.icarus.2009.03.032
- Tobie, G., Grasset, O., Lunine, J.I., Mocquet, A., Sotin, C., 2005. Titan's internal structure inferred from a coupled thermal-orbital model. *Icarus* 175, 496-502.
doi:10.1016/j.icarus.2004.12.007
- Tobie, G., Lunine, J.I., Sotin, C., 2006. Episodic outgassing as the origin of atmospheric methane on Titan. *Nature* 440, 61-64. doi:10.1038/nature04497
- Turcotte, D.L., Schubert, G., 2002. *Geodynamics*, 2nd ed. Cambridge University Press, New York.

CHAPTER IV

An Intrusive Cryovolcanic Origin for Domal Labyrinth Terrains on Titan

Implies a Water Ice-Rich Crust

Chapter III will be submitted to the journal Icarus as:

An Intrusive Cryovolcanic Origin for Domal Labyrinth Terrains on Titan Implies a Water Ice-Rich Crust

Lauren R. Schurmeier¹, Andrew J. Dombard¹, Michael Malaska², Jani Radebaugh³

¹Department of Earth and Environmental Sciences, University of Illinois at Chicago, 845 W. Taylor St., Chicago, IL

²Jet Propulsion Laboratory, Pasadena, CA.

³Brigham Young University, Provo, UT.

A. Abstract

Titan's organic-rich, topographically elevated, and highly dissected Labyrinth terrains are arguably the most Titanian geomorphic unit. How the region came to be composed of organics and remain elevated may hold clues about Titan's complicated history, and in particular the composition of Titan's crust. The Labyrinths are found in Titan's mid-latitudes, are dome-shaped and appear to be a clustering of uplifted, organic-rich Undifferentiated Plains. We use scaling relationships to determine if they formed over an elevated surface that was inflated by diapirs or cryovolcanic laccoliths. Based on the large spacing between features, we find it unlikely that they formed via density-driven diapirism. Instead, their dimensions suggest that they are cryovolcanic intrusions that formed at the most prominent rheological contrast in Titan's ice shell, the brittle-ductile transition (BDT). At that transition, the intrusion spreads horizontally and inflates, forming large cryovolcanic laccoliths or upturned saucer-shaped sills. This intrusion flexes the overlying lithosphere and thin surficial sedimentary layers (Undifferentiated Plains), resulting in a domed feature that is more prominent and thus susceptible to erosion from methane rain. This process then led to the highly dissected, dome-shaped Labyrinth terrains. To determine if the laccoliths formed near Titan's BDT, we calculate a lithospheric strength envelope for pure water ice and methane clathrate ice shells. The plausible range for the BDT for a pure water ice shell (21-50 km) agrees well with the expected intrusion depth for the laccoliths (29-33 km) from a scaling relationship. Surprisingly, the expected BDT for a methane clathrate ice shell is too shallow (9-14 km) to match our observations. While methane clathrate is known to be significantly

stronger than ice, its low thermal conductivity significantly raises the shell's temperature profile, and results in a lithosphere that is too thin to agree with our observations and previous modeling efforts. We conclude that in these locations, Titan's ice shell needs to be predominantly water ice, not methane clathrate, and there may be significant intrusive cryovolcanic activity deep within the water ice shell on Titan.

B. Introduction

Saturn's moon Titan is a unique world with a distinctive, orange, hazy atmosphere. Its orange color arises from photochemical reactions between nitrogen and methane that result in the production of a plethora of organic molecules of varying complexity. Termed "tholins" (Khare et al., 1984), these materials form several orange haze layers that are opaque to visible light. The hazes veil an Earth-like, yet alien world filled with vast sand seas of thousands of organic-rich, long, linear dunes (Lorenz et al., 2006; Radebaugh, 2013), organic-rich plains (Lopes et al., 2016), mountainous regions of varying size, composition and morphology (Cook-Hallett et al., 2015; Liu et al., 2016a; Lorenz et al., 2013; Mitri et al., 2010; Radebaugh et al., 2007), clouds that precipitate liquid methane (Turtle et al., 2011), river channels (Burr et al., 2013), and lakes and seas of liquid methane and ethane in the polar-regions (Stofan et al., 2007).

The photochemical breakdown of Titan's atmosphere leads to a rapid and irreversible depletion of methane. The current amount of methane should be depleted within 10-100 Myr (e.g. Toubanc et al., 1995; Yung et al., 1984); hence methane replenishment is presumed to somehow occur. Replenishment may be accomplished by means of large bodies of near-surface methane reservoirs (currently unconfirmed at the appropriate scale), released from near-surface methane hydrate clathrates due to the substitution of methane with ethane liquids percolating into the crust (Choukroun and Sotin, 2012), direct atmospheric insertion due to cryovolcanic eruptions (Lopes et al., 2016), and due to the destabilization of methane clathrates around near-surface intrusive cryovolcanism

(Choukroun et al., 2010) or during episodes of internal convection (Tobie et al., 2006). The extent of clathrates in the ice shell through time is not currently well constrained. Methane clathrates are stable throughout the equilibrium thermal profile of Titan, but it is not established where the clathrates are located; mixed into the entire ice shell, present in the top 5-10 km of the ice crust, or even separated into a layer either just below or just above the ammonia-water ocean (Choukroun et al., 2010; Grasset et al., 2000; Loveday et al., 2001; Tobie et al., 2006). Moreover, the amount and even existence of cryovolcanism is also currently debated (e.g., Lopes et al., 2013; Moore and Pappalardo, 2011). If cryovolcanism does exist, there should be an even greater extent of intrusive cryovolcanism that never breached the surface. On Earth, Mars, Venus, and the Moon, intrusive volcanism volumes exceed those of extrusive volcanism (e.g., Greeley and Schneid, 1991; White et al., 2006). Therefore, if Titan has cryovolcanism, we should expect to see some signs of intrusive cryovolcanic activity as well. Unlike silicate volcanism, the neutral buoyancy level of cryomagmas (in this case, water) is not above the surface, but is actually in the upper 10% of the ice column. Furthermore, slight amounts of pressure or the inclusion of materials to lower the cryomagma density (e.g., ammonia) makes intrusive cryovolcanism not only possible, but likely.

The Labyrinth terrains on Titan are arguably the most uniquely Titanian geomorphic unit. They are defined by their regionally high elevation, medium SAR backscatter, and high microwave emissivity that indicates that they are made of organics and not water ice (Malaska et al., 2016). The name Labyrinth is a reference to their distinctively high density of channel dissection that is reminiscent of complex mazes. The channels are undoubtedly negative

topography, confirmed by the bright-dark pairing of SAR backscatter in the up-range and down-range side, due to reflections and shadows on canyon walls. The level of channel dissection is always high in labyrinth terrains, but the thickness and amount of branching in channels varies across different Labyrinth units. The style of channel networking is either radial, structurally controlled (i.e., rectangular), or random. Labyrinth terrains are generally found in groups, both in the mid-latitudes and near the polar-regions, but are notably scarce in the equatorial region. The radial Labyrinth terrains found at mid-latitudes (Malaska et al., 2016) are of particular interest because it is unclear how these organics collected and became notably large - scale positive topography, while remaining significantly more eroded than other units on Titan. Titan's Labyrinth terrains are a uniquely Titanian type of high-standing topography rarely seen on other planetary bodies, and are likely a key clue to understanding the complicated evolution of Titan's ice shell.

Radial Labyrinths are generally circular or elliptical features in planform. We believe that they are generally dome shaped according to sparse topography data and the branching patterns of channels that we interpret as fluvial networks (formed by methane rain) that appear to flow downslope, outward from the dome center. They are found exclusively in the mid-latitudes and are always surrounded by the Undifferentiated Plains unit (Lopes et al., 2016). The Undifferentiated Plains, nicknamed the "blandlands" for their notably homogeneous SAR-dark appearance, generally featureless appearance (including a lack of fluvial erosion), and low relief. The composition of the Undifferentiated Plains is thought to be organic-rich and water ice-poor, due to high microwave emissivity (similar to that of the dunes and Labyrinth terrains), and very low SAR backscatter that is only slightly brighter than

that of the dark dune fields but darker than the mountains (Malaska et al. 2016). Based on similar composition and geographic context, we suggest that radial Labyrinth terrains are uplifted portions of the Undifferentiated Plains. Once uplifted, they become progressively more susceptible to fluvial erosion from methane rain due to the increase in potential energy associated with a rising riverhead level. In this paper, we aim to explain the formation of radial Labyrinth terrains as uplifted Undifferentiated Plains, and find that their dimensions are consistent with the formation of an intrusive cryovolcanic lenticular intrusion in a water ice (not clathrate-rich) crust.

C. Observations of Labyrinths

The data used is derived from the Cassini multimode Ku-band (2.2 cm wavelength) RADAR instrument designed to map Titan's surface (Elachi et al., 2005) in four modes - SAR (Synthetic Aperture Radar), altimetry, scatterometry, and radiometry. In this study, we use the products of SAR, altimetry, and SAR-derived topography (SARTopo). The SAR mode of the RADAR instrument operates below an altitude of 4000 km, resulting in resolution cell size down to 300 m. Lower-resolution, high altitude "HiSAR" is not used in this study. The variations in radar backscatter in SAR images can be interpreted in terms of variations of near-surface roughness at the wavelength scale, surface slope at the pixel scale, and near-surface dielectric properties. Topography data from the RADAR instrument came directly from the altimetry mode and indirectly derived by comparing the calibration of overlapping SAR imagery obtained from different antenna feeds of the RADAR instrument (SARTopo - see Stiles et al., 2009). We use the most recent update to Titan's topographic data (Corlies et al., 2017) and Cassini RADAR swaths taken during Titan flybys T00A through T95. Using the mapping software Esri ArcGIS 10.4, we search the mapped locations of Labyrinth terrains (Lopes et al., 2016; Malaska et al., 2016) in the Cassini RADAR swaths for notable patterns in the distribution of radial Labyrinth terrains. We identify a region of interest that includes several Labyrinths (A - H) that exhibit radial or nearly radial dissection patterns in the northern mid-latitudes (Fig. 1).

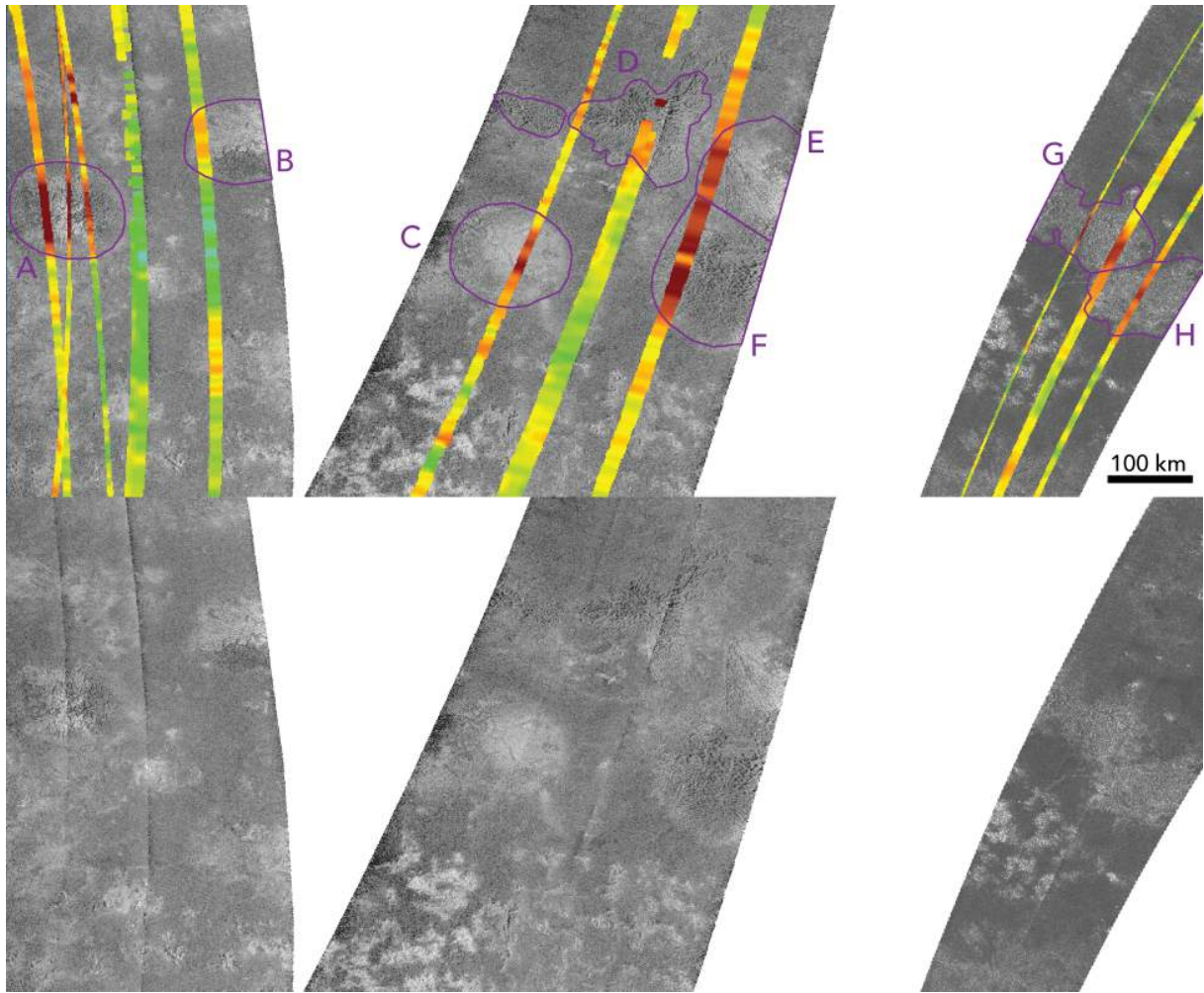


Figure 1: Region of interest with at least 7 locations of domed Labyrinths, and the informally named "hot cross bun" feature (C). The generally featureless gray regions are Undifferentiated Plains. The images are Synthetic Aperture Radar images and colored with warm and cool colors to indicate high and low elevations. The range of actual elevations in this figure is from ~750 (red) m to -500 (blue). Extends from ~142° E to 39° E, and 45° N to 32° N. It includes SAR images and SARTopo from Cassini flybys T64, T68, T83, and T95, and the whitespace is unmapped regions. Map scale is 1:2,000,000.

1. Description of the Labyrinths

The region of interest spans from about 142° E to 39° E, and 45° N to 32° N, and includes SAR images from four Titan flybys (T64, T68, T83, and T95). In Fig. 1 on the left side of leftmost SAR image is the quintessential example of a radially eroded Labyrinth terrain, named Anbus (Fig. 1, feature A). Anbus is circular in planform and is highly dissected by what we interpret as fluvial channels caused by methane rain (Fig. 2). The channels appear to originate from the center of the feature and flow radially outwards in a similar fashion to dome-shaped, radially dissected features on Earth such as volcanic domes. Fortuitously, three strips of SARTopo nicely cross the entire feature (Fig. 2). Using the 3D analyst tool in ArcGIS, we produce topographic profiles and confirm that the feature is generally dome shaped based on the elevated and concave downward profiles. Within the same SAR strip, another feature (Fig. 1, feature B) shares a similar, domed appearance. Unfortunately, it appears to extend outside of the SAR image, and the nearest SARTopo strip barely grazes the far edge of the feature. The limited topographic coverage does show some positive topography in a concave downward shape that matches with the extent of the feature seen in the SAR imagery. The channel dissection of this feature is not as obviously radial as Anbus, and appears more parallel (which are interpreted as yardangs) but the channels again appear to flow outwards toward the north from the assumed center. The southern side is more chaotically eroded (and therefore more difficult to interpret), but there are some channel-like features radiating outwards.

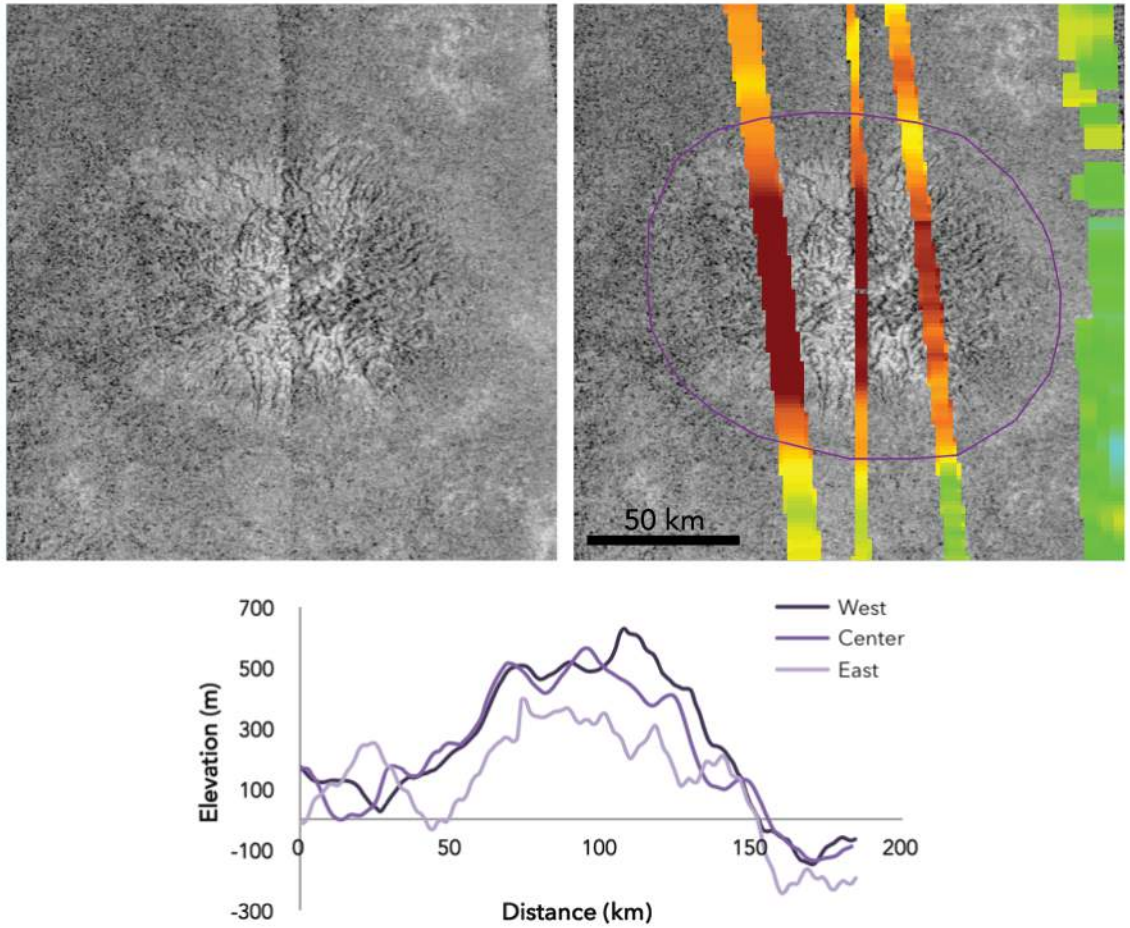


Figure 2: Radial Labyrinth terrain Anbus (feature A) with SARTopo data (right) and without (left). Three topographic profiles of the SARTopo data are included below (west, center, and east), which span the entire image from North to South. North is at the top of the image.

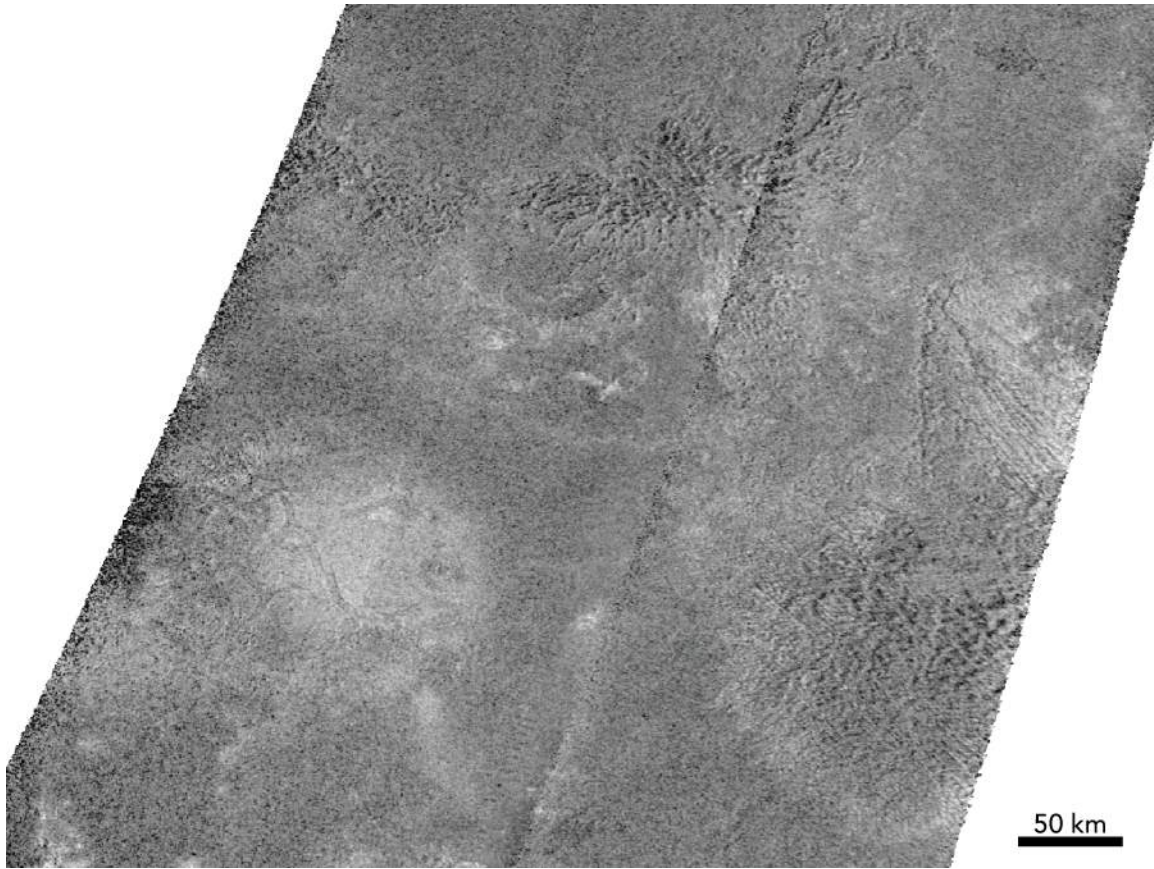


Figure 3: Center Cassini SAR images in closer detail, showing features C-F.

In the central SAR swath of Fig. 1, there are several more topographic mounds with dome-like appearances clustered together (Fig. 3). In the bottom left is the feature nicknamed the “hot cross bun” (Lopes et al., 2012) for its domed shape and four thick graben-like depressions that radiate from a central depression in a cross shape, reminiscent of the baked treat (Fig. 1, feature C; Fig. 3). The large valleys show radar darkening on both sides (outlining the edges of the channels), and have a relatively constant thickness. This structural morphology is

consistent with normal faulting caused by tension from the stretching of the sediments caused by a subsurface intrusion. It is circular in planform, similar to Anbus, and instead of a heavily dissected surface, it is generally radar bright. These differences may indicate that the hot cross bun feature is composed of a different material than the others, or it is at an early or end state of the erosive process. The hot cross bun was previously interpreted as a cryovolcanic laccolith based on its morphological similarities with other domed objects interpreted as volcanic intrusions on Venus and the Moon (Lopes et. al 2012). North of the hot cross bun is a feature named Richese (Fig. 1, feature D; Fig. 3). It is the least elliptical feature of the set, has a more chaotic erosive morphology, and less SARTopo coverage. Based on the limited topographic data, we can see that it at least it extends to a similar height as the other domed features. It also includes some indications of radial dissection from the highest point in the SARTopo.

On the right side of the central SAR image, there is a larger feature that appears to extend of out the SAR swath in both directions. The SARTopo shows that it is a relatively tall feature, and much more broad than the other domed features. Morphologically, it appears to be two different domes that have merged together. The upper and lower portions are eroded differently and there is a dip in the topographic profile where these features meet. The erosive state of the northern portion (Fig. 1, feature E; Fig. 3) is brighter, and the channels are much more parallel. (yardangs, perhaps). The southern portion (Fig. 1, feature F; Fig. 3) is darker, and the erosive state is very chaotic. It is difficult to discern trends in the erosive patterns, but it appears that the channels are darker and wider near the feature's

center. Based on the morphology, we suggest that this feature is actually two smaller features that have merged as the intrusion uplifted them and as they eroded outwards.

In the SAR image on the right, there is another chaotically eroded feature that we also believe is the result of the merging of two features (Fig. 1, features G and H; Fig. 4). Three topographic profiles cross through these features, all of which show a concave downward shape, with the highest peaks corresponding with the centers of the two radar bright regions. We interpret these as two merged features because there is a radar dark region between them (similar in appearance to the surrounding low lying Undifferentiated Plains) that corresponds with a slightly lower elevation. Additionally, the peaks in the two SARTopo topographic profiles that cross the left portion (G) are located notably higher north than the location of the topographic peak in the only available SARTopo strip of the right portion (H). This indicates that there are two adjacent domes, shifted slightly in the north-south direction.

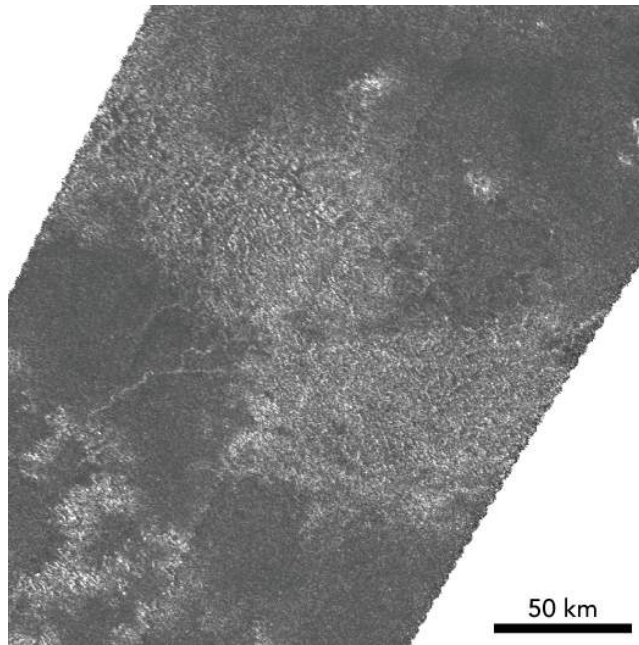


Figure 4: Cassini SAR image of features G and H.

2. Measurements

Rough outlines of the features are made primarily using the morphological differences in the SAR imagery between the features and the surrounding Undifferentiated Plains and secondarily using the limited SARTopo topographic information. These outlines generally agree with previous mapping efforts of Labyrinth terrains (Lopes et al., 2016; Malaska et al., 2016), but are not as finely detailed. We choose a simplified outline because we are after general dimensions and recognize that these features are highly eroded and modified. We use these outlines and the SARTopo profiles to measure their shortest and longest widths and the spacing between the assumed centers of Labyrinths within the same SAR strip. The Labyrinths within our region of interest have maximum diameters ranging from ~130 km to 160 km (or larger, if these features extend out of the imaged area), and spacings (λ) between the assumed domed centers ranges from 130 km to 250 km.

D. Models of Formation and Mechanics

The Labyrinth terrains are compositionally similar to the surrounding Undifferentiated Plains (Lopes et al., 2016; Malaska et al., 2016), but morphologically they are distinct because the Labyrinths are significantly more eroded and are roughly either elliptical in planform or a merged form of two elliptical shapes (rather than featureless and expansive). In 3D, they appear generally dome shaped based on the sparse topography data available, along with the branching patterns of channels (interpret as fluvial networks) that appear to flow downslope outward from the presumed dome centers. We suggest that these features are uplifted portions of the Undifferentiated Plains and not inverted topography or the remnants of regional deflation of the surrounding regions because we find it improbable that nearly all of the surrounding area eroded or deflated to a common low elevation, leaving such suspiciously elliptical features of similar sizes. Based on their clustering and appearance, we suggest that the two most plausible forms of uplift include diapiric upwelling and lenticular cryovolcanic intrusions (Schurmeier et al., 2018).

1. Diapiric Upwelling

The clustering, general dome shape and highly eroded peaks of these Labyrinths relative to the surrounding materials bares a notable resemblance to salt diapir fields on Earth. Diapirs form through the buoyant upwelling of relatively low-density material with the ability to flow on relatively short timescales. The spacing between diapirs, λ , in a simple system may be related to the thickness of the rising layer, as seen in examples on Earth and Triton (Schenk and Jackson, 1993; Turcotte and Schubert, 2002). In this simplistic two-layer system, this model predicts that the dominant wavelength (also λ) for diapiric growth by Rayleigh-Taylor instability is related to the thickness of the rising layer, h , by the relationship $\lambda = 2.57 h$ (Turcotte and Schubert, 2002). The range in spacing between these features thus implies a rising layer thickness of 50 km to nearly 100 km. We find that this thickness is unreasonable for two reasons. The range is far too large to imply that these features stemmed from the same subsurface layer when these features are located so close together. Second, it is unlikely that a low density, mobile layer exists in such a large thickness beneath Titan's upper sedimentary layers. Indeed, the upper end of our estimate is the expected full thickness of the entire ice shell on Titan. While this simplistic diapiric model may not perfectly explain the likely more complicated processes that could lead to diapiric upwelling on Titan, we suggest that the implied rising layer thickness is unreasonably large.

2. Intrusive Cryovolcanism

A recent study by Manga and Michaut (2017) explained Europa's lenticulae (pits, domes, spots and small chaos features) with intrusive cryovolcanism at the base of Europa's lithosphere. On Earth, vertical dike intrusions typically rise until they reach a rheological contrast that inhibits vertical motion and favors horizontal intrusion. In this model (Fig. 5), pressurized dikes or conduits of cryomagma (water or impure water mixtures) from a subsurface ocean or localized melt within the ice shell rises to the most prominent rheological contrast - the brittle-ductile transition at the base of the lithosphere (depth d). At this boundary, it becomes easier for the intrusion to spread horizontally as a lenticular sill (Fig. 5: crack stage). The sill fills and extends out to radius r , forming a laccolith that begins to flex the overlying lithosphere (Fig. 5: laccolith stage). This bending of the lithosphere rotates the stress at the edges of the intrusion, and a critical transition occurs in which it is easier for the crack to propagate vertically than to continue horizontally (see Manga and Michaut, 2017 for a more detailed description). This transition forms a large saucer-shaped intrusion that includes the horizontal laccolith and upward inclined sheets, and continues to flex the overlying layers (Fig. 5: saucer-shaped sill and thickening stage). The final uplift occurs when the fractured overlying ice flexes as the intrusion cools and solidifies (Fig. 5: freezing and flexure of lithosphere stage).

On Titan, the relatively thin surficial Undifferentiated Plains, likely composed of organic-rich sediments (Lopes et al., 2016), would also uplift due to the flexing underlying ice. The sedimentary layers become more susceptible to erosion due to fracturing caused by

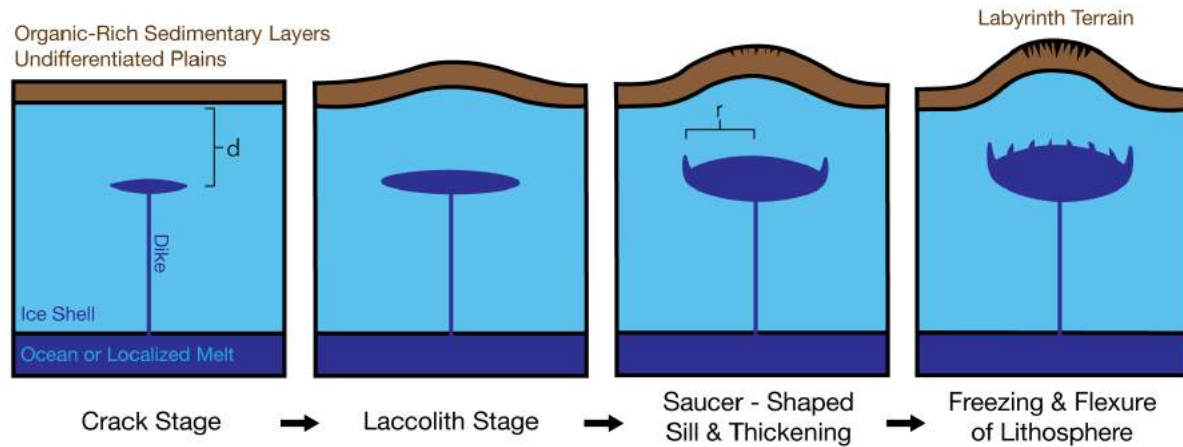


Figure 5: Uplift and formation sequence of dome shaped Labyrinth Terrains by intrusive cryovolcanism. Dikes of water from a subsurface ocean or localized melt within the ice shell rises to the bottom of the lithosphere (depth d) and spreads horizontally as a sill. The sill fills, forming a laccolith, and extends out to radius r , where stresses rotate to become easier to propagate upwards instead of horizontally. A saucer-shaped laccolith forms, and the infill of cryomagma flexes the overlying lithosphere and sedimentary layers. Freezing continues to expand and flex the lithosphere. The uplifted portions of the Undifferentiated Plains become more susceptible to erosion from methane, resulting in the highly dissected Labyrinth terrains. Modified from Manga and Michaut (2017).

the flexure. Perhaps more importantly, the increase in elevation provides more potential energy for the fluvial erosion due to methane rain, resulting in a greater ability of mechanical erosion by rain and fluvial channels and thus producing uplifted, highly eroded and generally dome shaped Labyrinth terrains within the Undifferentiated Plains unit.

Accordingly, the longest diameter of the Labyrinth terrains should approximately equal the largest extent (radius r) of the subsurface saucer-shaped laccolith intrusion. We

measure the longest diameter of the Labyrinths (or the longest diameter that is imaged for those on the edges of SAR swaths), and can predict a laccolith intrusion depth, d , where $r = 2.4 d$ (Manga and Michaut, 2017). Because the Manga and Michaut model utilizes a purely elastic rheological model, this depth is essentially at the base of Titan's elastic lithosphere at that location.

The elastic lithosphere, however, is approximately the same (though generally thinner) than a lithosphere composed of a brittle near-surface underlain by a ductile substrate. To determine if the laccoliths formed at the base of Titan's elastic lithosphere (essentially the brittle-ductile transition), we create a lithospheric strength envelope for pure water ice and methane clathrate ice shells. To calculate the brittle-ductile transition of Titan, we find where the ice shell transitions from brittle failure to ductile deformation (Fig. 6). Near Titan's surface, the ice is cold and brittle (surface temperature of 94 K). Instead of needing to exceed the brittle failure of intact rock, Byerlee's law (Byerlee, 1978) states that lower shear stresses are required to propagate failure along pre-existing fractures, where

$$\tau = \mu \sigma_n + b$$

and τ is the shear stress for failure, σ_n is the normal stress across the fault, b is a cohesion, and μ is the coefficient of friction (related to the angle of internal friction for the material). For Titan, we apply parameters from frictional sliding measurements of water ice (Beeman et al., 1988). Since the vertical stress is essentially the lithostatic load ($\sigma_{zz} = \rho g d$, where ρ is the ice density [950 kg m^{-3}], g is the gravity [1.35 m s^{-2}], and d is depth), this predicts a linear increase

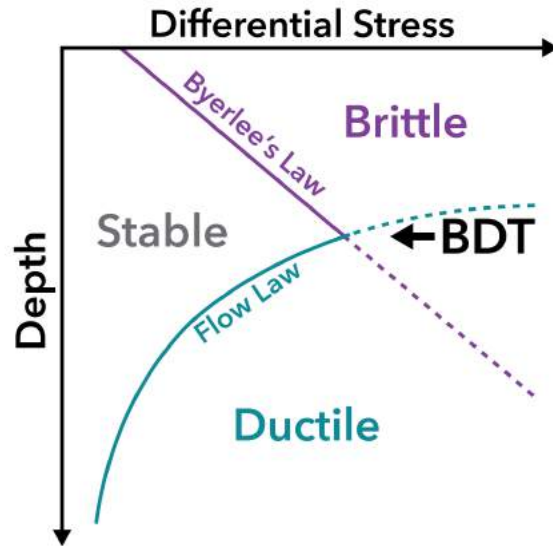


Figure 6: Schematic of a lithospheric strength envelope used to find the brittle-ductile transition (BDT) of a planetary ice shell. The BDT marks the transition depth where the ice shell transitions from brittle failure (Byerlee's law) to ductile deformation (dominant ductile flow law), essentially the base of the elastic lithosphere.

in yield stress with depth. Because the plane of minimum slip resistance is always tilted to the most compressive stress direction by the angle of internal friction, the brittle strength curves are different under horizontal compression and tension.

Meanwhile, as depth increases, temperature also increases, which decreases the ductile strength of the ice shell. For a water ice shell, creep experiments show that four regimes, dislocation creep, diffusion creep, grain boundary sliding, and easy-slip dislocation can control the ductile flow of ice (Goldsby and Kohlstedt, 2001). We calculate these regimes

for Titan's ice shell, using the following parameters: a surface temperature of 94 K (the current surface temperature), the assumed current basal heat flux of 4 mW/m², grain sizes of 0.1 and 10 mm, strain rates of $1 \times 10^{-18} \text{ s}^{-1}$ to $1 \times 10^{-13} \text{ s}^{-1}$, and an ice thermal conductivity that varies with temperature following the relationship $k = (651 \text{ W/m})/T$ (Petrenko and Whitworth, 1999). We identify the shallowest and deepest extent of the brittle-ductile transition for a water ice shell (Fig. 7). The extent of the elastic lithosphere should be around the brittle-ductile transition.

Additionally, we plot the lithospheric strength envelope for an ice shell made of methane clathrate (Fig. 7). Since the extent and existence of methane clathrates is not definitively constrained in Titan's ice shell, we examine two cases: a completely methane clathrate dominated ice shell, and cases that includes the thermal effects of 2-5 km of methane clathrate overlying a water ice shell. We apply the dislocation creep relationship for methane clathrate (Durham et al., 2003), but use the same brittle failure curves for water ice. The most notable differences between pure ice and methane clathrates are methane clathrate's increased strength at similar temperatures (Durham et al., 2003) and lower thermal conductivity of $0.5 \text{ W m}^{-1} \text{ K}^{-1}$ (Krivchikov et al., 2005).

The range in diameters of the Labyrinths implies an intrusion depth of 29-33 km. Assuming that the Labyrinths are surface expressions of similar scale subsurface cryovolcanic intrusions at the base of the lithosphere (where ice transitions from brittle to ductile behavior), this predicts a BDT of ~30 km depth. Figure 7 shows the lithospheric strength envelope for Titan for a 100% water ice shell (blue curves), and a 100% methane clathrate ice shell (red curves). We plot the brittle failure curves for water ice in compression and

extension as positive values for easier comparison. As noted previously, water ice has several ductile mechanisms that can operate, but only one will dominate at a given time. Thus, we explore a large parameter space and find the minimum and maximum BDT depths predicted, and display here the dominant mechanism curves. The two dominant mechanism curves happen to both be dislocation creep at the two strain rate extremes explored (blue curves in Fig. 7). The lithospheric strength envelope of a 100% water ice crust thus predicts a brittle-ductile transition in the range of 21 to 50 km. Surprisingly, we find that the BTD of a 100% methane clathrate ice shell is much more shallow, falling within the range of 9 to 14 km. Restricting the clathrate to a surface layer 5 km thick surficial layer makes the underlying water ice too warm for elastic support; therefore the brittle-ductile transition is essentially at the top of the water ice/clathrate interface around 5 km depth.

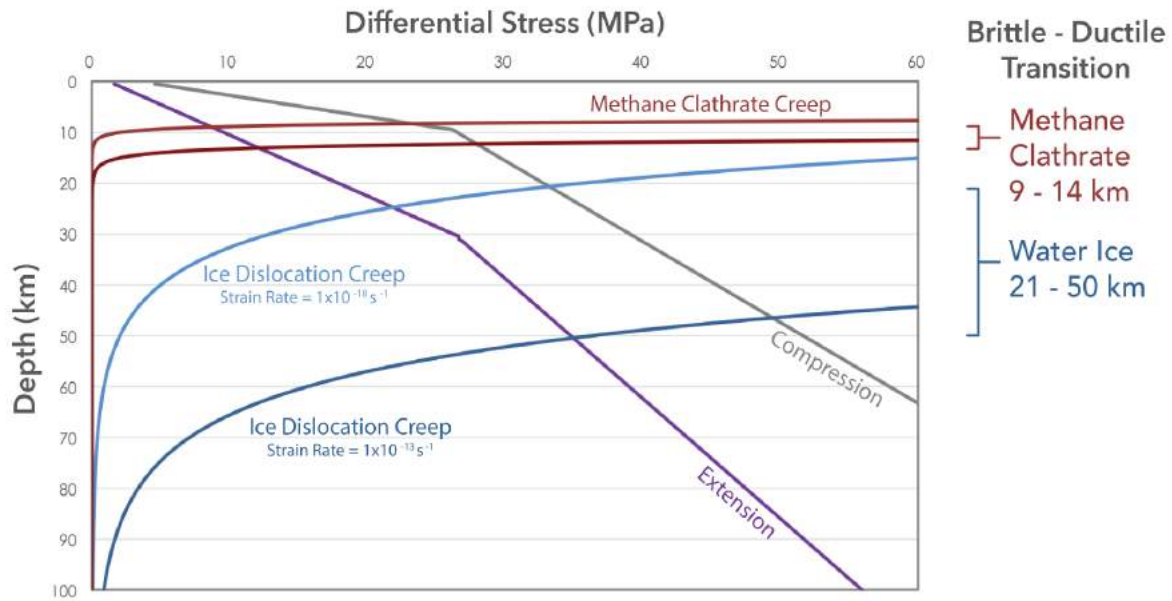


Figure 7: Titan's lithospheric strength envelopes. The brittle-ductile transition occurs at the depth where the brittle failure curve (in compression or extension) intersects with the dominant ductile creep flow law. This plot only shows the shallowest and deepest extent of the dominant ductile mechanism for ice (which includes dislocation creep, diffusion creep, grain boundary sliding, and easy slip over a range of parameters). Both the shallowest and deepest dominant mechanism are dislocation creep, but at the two extremes of the strain rates explored. For water ice, the brittle ductile transition is within the range of 21–50 km. For methane clathrate, the brittle - ductile transition is significantly shallower, in the range of 9–14 km.

E. Discussion

Despite looking very similar to terrestrial diapirs, we find no convincing evidence that the dome-shaped Labyrinths in Titan's northern mid-latitudes formed through buoyancy-driven diapirism. The spacing between features is too variable, and the predicted rising layer thicknesses are too large (50-100 km) to be a plausible formation mechanism. Considering that Titan's ice shell is thought to be ~100 km thick or less, and the fact that ice is brittle at Titan's surface temperatures, it does not seem plausible. The main expected materials on Titan surface are organics (tholins) and water ice. Water ice has a density around 950 kg m^{-3} , and Titan tholins produced in the laboratory have a density around 800 kg m^{-3} (Trainer et al., 2006), or in the range of $\sim 400\text{-}1100 \text{ kg m}^{-3}$ (Hörst and Tolbert, 2013). The most abundant solid product predicted to fall on Titan's surface is acetylene (Toublanc et al., 1995); it has a density of around 800 kg m^{-3} . Therefore, density contrasts between the different components of tholins, and between tholins and ice could exist. However, there is no evidence for a mechanism that would have produced such a thick (ice shell scale) low-density tholin layer beneath the surficial sediments of the Undifferentiated Plains. Thus large-scale density-driven motion is unlikely.

Instead, we suggest that these features are the surface expression of deep cryovolcanic intrusions. If these Labyrinths are large saucer-shaped intrusions, their maximum radii indicates that they formed beneath a lithosphere ~30 km thick. Results from our lithospheric strength envelope predict a brittle-ductile transition (BDT, essentially the base of the elastic lithosphere) within the range of 21 to 50 km for a water ice shell (Fig. 7). This BDT

agrees well with the intrusion depth predicted by our scaling relationships for a cryovolcanic saucer shaped sill/laccolith (from Manga and Michaut, 2017). Originally, this relationship was used to explain the formation of domes, pits, and chaos features (lenticulae) on Jupiter's moon Europa. The domed lenticulae are similar in height (a few hundred meters) compared with the domed Labyrinths in our study, but are about an order of magnitude smaller in maximum radii and therefore leads to a prediction of a much thinner lithosphere (a few kilometers). Europa's increased surface temperature, and significantly higher heat flow (mainly due to contributions from tidal heating), would result in a thinner lithosphere. On Titan, intrusions will need to spread farther horizontally to flex the thicker elastic lithospheres upward, but the height of the features would not need to be significantly larger, in agreement with our findings.

The presence of cryovolcanic intrusions is potentially important for astrobiological studies. All life on Earth uses liquid water, which is a main reason why NASA's astrobiology efforts focus a lot of attention on finding liquid water sources across the solar system. Several experimental studies of the chemical reactions that occur between Titan tholins and cryomagmas (water ammonia mixtures) have been explored, and they produced organics compounds of astrobiological interest, including amino acids (Brassé et al., 2017; Poch et al., 2012; Ramírez et al., 2010). Such reactions would likely require interactions of the surface organics and the cryomagma deep in Titan's ice shell, which may be difficult. However, the large size of the laccoliths proposed here does imply that the cryomagma would cool slowly (especially if it formed as several composite intrusions over time, as seen in many large

volcanic intrusions on Earth), likely creating a longer lasting water environment, thus giving more time for astrobiological chemistry to occur.

A surprising result of our analyses is the predicted BDT of a predominantly methane clathrate ice shell. Methane clathrate is known to be significantly stronger than pure water ice at similar temperatures according to creep experiments (Durham et al., 2003). In their study, they noted that methane clathrate at a given strain rate is over 20 times stronger than ice at the ice point, and that the contrast in strength increases at lower temperatures. This would suggest that a methane clathrate ice shell should have a much thicker lithosphere than that of a pure water ice shell. However, methane clathrate has a significantly lower thermal conductivity than water ice at relevant temperatures (at least an order of magnitude less). The low thermal conductivity inhibits conductive release of heat, thus significantly warming the ice shell. Since ductile creep is strongly controlled by temperature, the increase in temperature with depth results in the ductile mechanisms dominating closer to the surface. This creates a significantly shallower BDT, and a thinner, weaker lithosphere. The BDT that we calculate for methane clathrate (9-14 km) does not match the predicted intrusion depth of the laccoliths. Furthermore, even a few kilometers of methane clathrate in the surface of Titan's ice shell will significantly change the thermal profile of the underlying water ice shell, and would generally result in BDT that is too shallow to agree with our laccolith intrusion depth scaling relationship. Therefore, our work does not support the theory that methane clathrate is a significant part of Titan's upper ice shell at this location.

This result is in agreement with our previous work studying larger topographic loads (Schurmeier et al., in preparation). In that study, we aimed to understand how larger broad

Labyrinths (at least 350 km wide) found within the southern mid-latitudes, which we termed “mountainous plateaus”, are supported by Titan’s ice shell. We found that at Titan’s current heat flow, these features are easily supported by the lithosphere in a water ice shell. These simulations further showed that the likely extent of the BDT is within the range of 25-45 km, in agreement with the results of this study. We repeated this for methane clathrate and saw that large mountain plateaus are not supported, and instead quickly collapse. The warm, thin lithosphere of methane clathrate could not support such wide features. Altogether, this evidence suggests that methane clathrate cannot dominate the upper layers of Titan in the mid-latitudes. In a methane clathrate rich ice shell, we would expect to see smaller domed labyrinths in the northern mid-latitudes (which formed at shallower intrusion depths). We would also not expect to see stable, large mountainous plateaus because they are too large in wavelength to be supported by a thin methane clathrate lithosphere.

This finding may have important implications about methane replenishment from clathrates. At this current time and at these locations (mid-latitudes, and perhaps the equatorial region), it is unlikely that methane clathrate dominates Titan’s ice shell. Thus, atmospheric methane replenishment must come from elsewhere. We note that this does not completely exclude the presence methane clathrates on Titan – our work cannot comment on whether they it could occur in smaller, isolated amounts, in the distant past, or the polar regions. Future work will explore the effects of including methane clathrate only in the poles.

F. Conclusions

Titan's dome-shaped and clustered Labyrinth terrains within the northern mid-latitudes appear to be uplifted and eroded Undifferentiated Plains based on their similar composition and geographic context. Based on scaling relationships, we find that these Labyrinths are unlikely to be diapirs; instead, they are possibly the surface expression of saucer-shaped cryovolcanic intrusions that form near the base of Titan's lithosphere (Schurmeier et al., 2018).

We produce lithospheric strength envelopes for Titan's ice shell and find that the brittle-ductile transition for a water ice shell (21-50 km) agrees well with the intrusion depth predicted (~30 km) for Titan's domed Labyrinth terrains based on the scaling relationship developed by Manga and Michuat (2017). The BDT for a methane clathrate rich ice shell does not agree with this intrusion depth. Its high thermal conductivity results in a much warmer ice shell and a lithosphere that is too thin. Since the width of the laccolith scales linearly with the thickness of the lithosphere, lithospheres of a thickness consistent with a methane clathrate shell or thick clathrate surface layer would yield Labyrinth terrains a factor of several smaller than what is observed.

Our results, in combination with previous work modeling the support of larger features on Titan (Schurmeier et al., in preparation) indicate that methane clathrate cannot dominate the crust of Titan at these locations. Thus, we find that significant replenishment of atmospheric methane via release from thick near-surface methane clathrate layers is unlikely at these locations. Our results further imply that there may be significant intrusive

cryovolcanic activity deep within the water ice shell on Titan, and cryovolcanism may be more widespread than previously estimated.

G. Works Cited:

- Beeman, M., Durham, W.B., Kirby, S.H., 1988. Friction of Ice. *J. Geophys. Res.* 93, 7625–7633.
- Brassé, C., Buch, A., Coll, P., Raulin, F., 2017. Low-Temperature Alkaline pH Hydrolysis of Oxygen-Free Titan Tholins: Carbonates' Impact. *Astrobiology* 17, 8–26.
doi:10.1089/ast.2016.1524
- Burr, D.M., Taylor Perron, J., Lamb, M.P., Irwin, R.P., Collins, G.C., Howard, A.D., Sklar, L.S., Moore, J.M., Ádámkovics, M., Baker, V.R., Drummond, S. a., Black, B. a., 2013. Fluvial features on Titan: Insights from morphology and modeling. *Bull. Geol. Soc. Am.* 125, 299–321. doi:10.1130/B30612.1
- Byerlee, J., 1978. Friction of rocks. *pure Appl. Geophys.* 116, 615–626.
doi:10.1007/BF00876528
- Choukroun, M., Grasset, O., Tobie, G., Sotin, C., 2010. Stability of methane clathrate hydrates under pressure: Influence on outgassing processes of methane on Titan. *Icarus* 205, 581–593. doi:10.1016/j.icarus.2009.08.011
- Choukroun, M., Sotin, C., 2012. Is Titan's shape caused by its meteorology and carbon cycle? *Geophys. Res. Lett.* 39, 1–5. doi:10.1029/2011GL050747
- Cook-Hallett, C., Barnes, J.W., Kattenhorn, S.A., Hurford, T., Radebaugh, J., Stiles, B., Beuthe, M., 2015. Global contraction/expansion and polar lithospheric thinning on Titan from patterns of tectonism. *J. Geophys. Res. E Planets* 120, 1220–1236.
doi:10.1002/2014JE004645
- Corlies, P., Hayes, A.G., Birch, S.P.D., Lorenz, R., Stiles, B.W., Kirk, R., Poggiali, V., Zebker, H., less, L., 2017. Titan's Topography and Shape at the End of the Cassini Mission. *Geophys. Res. Lett.* 44, 11,754–11,761. doi:10.1002/2017GL075518
- Durham, W.B., Kirby, S.H., Stern, L.A., Zhang, W., 2003. The strength and rheology of methane clathrate hydrate. *J. Geophys. Res. Solid Earth* 108, 1–11.
doi:10.1029/2002JB001872
- Elachi, C., Allison, M.D., Borgarelli, L., Encrenaz, P., Im, E., Janssen, M. a., Johnson, W.T.K., Kirk, R.L., Lorenz, R.D., Lunine, J.I., Muhleman, D.O., Ostro, S.J., Picardi, G., Posa, F., Rapley, C.G., Roth, L.E., Seu, R., Soderblom, L. a., Vetrella, S., Wall, S.D., Wood, C. a., Zebker, H. a., 2005. Radar: The Cassini Titan RADAR mapper. *Space Sci. Rev.* 115, 71–110. doi:10.1007/s11214-004-1438-9
- Goldsby, D.L., Kohlstedt, D.L., 2001. Superplastic deformation of ice: Experimental observations. *J. Geophys. Res. Solid Earth* 106, 11017–11030.

doi:10.1029/2000JB900336

Grasset, O., Sotin, C., Deschamps, F., 2000. On the internal structure and dynamics of Titan. *Planet. Space Sci.* 48, 617-636.

Greeley, R., Schneid, B.D., 1991. *Magma Generation on Mars : Amounts , Rates , and Comparisons with Earth , Moon , and Venus* Author (s): Ronald Greeley and Byron D . Schneid Published by : American Association for the Advancement of Science Stable URL : <http://www.jstor.org/stable/28797254>, 996-998.

Hörst, S.M., Tolbert, M.A., 2013. In situ measurements of the size and density of titan aerosol analogs. *Astrophys. J. Lett.* 770. doi:10.1088/2041-8205/770/1/L10

Khare, B.N., Sagan, C., Thompson, W.R., Arakawa, E.T., Suits, F., Callcott, T. a, Williams, M.W., Shrader, S., Ogino, H., Willingham, T.O., Nagy, B., 1984. The organic aerosols of Titan. *Adv. Space Res.* 4, 59-68. doi:10.1016/0273-1177(84)90545-3

Krivchikov, a. I., Gorodilov, B.Y., Korolyuk, O. a., Manzhelii, V.G., Conrad, H., Press, W., 2005. Thermal conductivity of methane-hydrate. *J. Low Temp. Phys.* 139, 693-702. doi:10.1007/s10909-005-5481-z

Liu, Z.Y.C., Radebaugh, J., Harris, R. a., Christiansen, E.H., Neish, C.D., Kirk, R.L., Lorenz, R.D., 2016. The tectonics of Titan: Global structural mapping from Cassini RADAR. *Icarus* 270, 14-29. doi:10.1016/j.icarus.2015.11.021

Lopes, R., Stofan, E.R., Wall, S.D., Wood, C., Kirk, R.L., Lucas, A., Mitchell, K.L., Lunine, J.I., Turtle, E.P., Radebaugh, J., Malaska, M., 2012. Titan's "Hot Cross Bun": A Titan Laccolith?, in: *AAS/Division for Planetary Sciences Meeting*.

Lopes, R.M.C., Kirk, R.L., Mitchell, K.L., Legall, a., Barnes, J.W., Hayes, a., Kargel, J., Wye, L., Radebaugh, J., Stofan, E.R., Janssen, M. a., Neish, C.D., Wall, S.D., Wood, C. a., Lunine, J.I., Malaska, M.J., 2013. Cryovolcanism on Titan: New results from Cassini RADAR and VIMS. *J. Geophys. Res. E Planets* 118, 416-435. doi:10.1002/jgre.20062

Lopes, R.M.C., Malaska, M.J., Solomonidou, a., Le Gall, a., Janssen, M. a., Neish, C.D., Turtle, E.P., Birch, S.P.D., Hayes, a. G., Radebaugh, J., Coustenis, a., Schoenfeld, a., Stiles, B.W., Kirk, R.L., Mitchell, K.L., Stofan, E.R., Lawrence, K.J., 2016. Nature, distribution, and origin of Titan's Undifferentiated Plains. *Icarus* 270, 162-182. doi:10.1016/j.icarus.2015.11.034

Lorenz, R.D., Stiles, B.W., Aharonson, O., Lucas, A., Hayes, A.G., Kirk, R.L., Zebker, H. a., Turtle, E.P., Neish, C.D., Stofan, E.R., Barnes, J.W., 2013. A global topographic map of Titan. *Icarus* 225, 367-377. doi:10.1016/j.icarus.2013.04.002

Lorenz, R.D., Wall, S., Radebaugh, J., Boubin, G., Reffet, E., Janssen, M., Stofan, E., Lopes, R.,

- Kirk, R., Elachi, C., Lunine, J., Mitchell, K., Paganelli, F., Soderblom, L., Wood, C., Wye, L., Zebker, H., Anderson, Y., Ostro, S., Allison, M., Boehmer, R., Callahan, P., Encrenaz, P., Ori, G.G., Francescetti, G., Gim, Y., Hamilton, G., Hensley, S., Johnson, W., Kelleher, K., Muhleman, D., Picardi, G., Posa, F., Roth, L., Seu, R., Shaffer, S., Stiles, B., Vetrella, S., Flamini, E., West, R., 2006. The sand seas of Titan: Cassini RADAR observations of longitudinal dunes. *Science* 312, 724–727. doi:10.1126/science.1123257
- Loveday, J.S., Nelmes, R.J., Guthrie, M., Belmonte, S.A., Allan, D.R., Klug, D.D., Tse, J.S., Handa, Y.P., 2001. Stable methane hydrate above 2[thinsp]GPa and the source of Titan's atmospheric methane 410, 661–663. doi:10.1038/35070513
- Malaska, M.J., Lopes, R.M.C., Williams, D. a., Neish, C.D., Solomonidou, A., Soderblom, J.M., Schoenfeld, A.M., Birch, S.P.D., Hayes, A.G., Le Gall, A., Janssen, M. a., Farr, T.G., Lorenz, R.D., Radebaugh, J., Turtle, E.P., 2016. Geomorphological map of the Afekan Crater region, Titan: Terrain relationships in the equatorial and mid-latitude regions. *Icarus* 270, 130–161. doi:10.1016/j.icarus.2016.02.021
- Manga, M., Michaut, C., 2017. Formation of lenticulae on Europa by saucer-shaped sills. *Icarus* 286, 261–269. doi:10.1016/j.icarus.2016.10.009
- Mitri, G., Bland, M.T., Showman, A.P., Radebaugh, J., Stiles, B., Lopes, R.M.C., Lunine, J.I., Pappalardo, R.T., 2010. Mountains on Titan: Modeling and observations. *J. Geophys. Res. E Planets* 115, 1–15. doi:10.1029/2010JE003592
- Moore, J.M., Pappalardo, R.T., 2011. Titan: An exogenic world? *Icarus* 212, 790–806. doi:10.1016/j.icarus.2011.01.019
- Petrenko, V.F., Whitworth, R.W., 1999. *Physics of Ice*. Oxford University Press, Oxford.
- Poch, O., Coll, P., Buch, A., Ramírez, S.I., Raulin, F., 2012. Production yields of organics of astrobiological interest from H₂ONH₃hydrolysis of Titans tholins. *Planet. Space Sci.* 61, 114–123. doi:10.1016/j.pss.2011.04.009
- Radebaugh, J., 2013. Dunes on Saturn's moon Titan as revealed by the Cassini Mission. *Aeolian Res.* 11, 23–41. doi:10.1016/j.aeolia.2013.07.001
- Radebaugh, J., Lopes, R.M.C., Lunine, J.I., Kirk, R.L., Wall, S.D., Stofan, E.R., Lorenz, R.D., 2007. Mountains on Titan observed by Cassini Radar. *Icarus* 192, 77–91. doi:10.1016/j.icarus.2007.06.020
- Ramírez, S.I., Coll, P., Buch, A., Brassé, C., Poch, O., Raulin, F., 2010. The fate of aerosols on the surface of Titan. *Faraday Discuss.* 147, 419. doi:10.1039/c003925j
- Schenk, P., Jackson, M.P.A., 1993. Diapirism on Triton: a record of crustal layering and instability. *Geology* 21, 299–302. doi:10.1130/0091-7613(1993)021<0299:

- Schurmeier, L., Dombard, A., Radebaugh, J., Malaska, M., 2018. Intrusive and Extrusive Cryovolcanism and the Composition of Titan's Icy Crust, in: LPSC. doi:Abstract # 2934
- Stiles, B.W., Hensley, S., Gim, Y., Bates, D.M., Kirk, R.L., Hayes, A., Radebaugh, J., Lorenz, R.D., Mitchell, K.L., Callahan, P.S., Zebker, H., Johnson, W.T.K., Wall, S.D., Lunine, J.I., Wood, C. a., Janssen, M., Pelletier, F., West, R.D., Veeramacheneni, C., 2009. Determining Titan surface topography from Cassini SAR data. *Icarus* 202, 584–598. doi:10.1016/j.icarus.2009.03.032
- Stofan, E.R., Elachi, C., Lunine, J.I., Lorenz, R.D., Stiles, B., Mitchell, K.L., Ostro, S., Soderblom, L., Wood, C., Zebker, H., Wall, S., Janssen, M., Kirk, R., Lopes, R., Paganelli, F., Radebaugh, J., Wye, L., Anderson, Y., Allison, M., Boehmer, R., Callahan, P., Encrenaz, P., Flamini, E., Francescetti, G., Gim, Y., Hamilton, G., Hensley, S., Johnson, W.T.K., Kelleher, K., Muhleman, D., Paillou, P., Picardi, G., Posa, F., Roth, L., Seu, R., Shaffer, S., Vetrella, S., West, R., 2007. The lakes of Titan. *Nature* 445, 61–64. doi:10.1038/nature05438
- Tobie, G., Lunine, J.I., Sotin, C., 2006. Episodic outgassing as the origin of atmospheric methane on Titan. *Nature* 440, 61–64. doi:10.1038/nature04497
- Toublanc, D., Parisot P., Brillet, J., Gautier, D., Raulin, F., McKay, C.P., 1995. Photochemical modelling of Titan's atmosphere. *Icarus*.
- Trainer, M.G., Pavlov, A.A., DeWitt, H.L., Jimenez, J.L., McKay, C.P., Toon, O.B., Tolbert, M.A., 2006. Organic haze on Titan and the early Earth. *Proc. Natl. Acad. Sci.* 103, 18035–18042. doi:10.1073/pnas.0608561103
- Turcotte, D.L., Schubert, G., 2002. *Geodynamics*, 2nd ed. Cambridge University Press, New York.
- Turtle, E.P., Perry, J.E., Hayes, a G., Lorenz, R.D., Barnes, J.W., McEwen, a S., West, R. a, Del Genio, a D., Barbara, J.M., Lunine, J.I., Schaller, E.L., Ray, T.L., Lopes, R.M.C., Stofan, E.R., 2011. Rapid and extensive surface changes near Titan's equator: evidence of April showers. *Science* 331, 1414–1417. doi:10.1126/science.1201063
- White, S.M., Crisp, J.A., Spera, F.J., 2006. Long-term volumetric eruption rates and magma budgets. *Geochemistry, Geophys. Geosystems* 7. doi:10.1029/2005GC001002
- Yung, Y., Allen, M., Pinto, J., 1984. Photochemistry of the atmosphere of Titan: Comparison between model and observations. *Astrophys. J.* 55, 465–506.

CHAPTER V

APPENDICES

A. Appendix A. for Chapter II: Thermal File Example for Crater Relaxation:

Note: the MARC finite element package has been used extensively for simulating planetary lithosphere deformation. A complete MARC finite element package is built by combining: a .dat file for the thermal simulation, a .dat file for the mechanical simulation, and a user-subroutine file (or .f file, in Appendix ###). As an example, I show the .dat files and a .f file relaxation of a crater. The actual .dat files are very long, so I edit the file to exclude some of the coordinate and connectivity arrays. Lines that start with \$ are not read by the MARC package and are included as notes. Readers are encouraged to refer to the MARC user manuals for a complete set of explanation.

Example: Sinlap crater (radius 40 km) filled with a maximum thickness of 400 m of sand (158 K), using thermal conductivity of $0.025 \text{ W m}^{-1}\text{K}^{-1}$.

```
title          job1
$....MARC input file produced by Marc Mentat 2010.2.0 (64bit)
$.....
$....input file using extended precision
extended
$.....
sizing          0   1500   1581   51
alloc          25
elements        40
version         11
table           0   0   2   1   1   0   0   1
processor        1   1   1   0
$no list
heat            0   0   1   0   1   1
thermal
all points
no echo         1   2   3
setname         19
end
$.....
solver
  8   0   0   0   0   0   0   0   0   0   0   0   0   0   0
0
optimize        11
connectivity
```

```

0    0    1
1   40    1  103  104    5
2   40  103  105  106  104
$(deleted remaining connectivity array)

```

```

coordinates
3 1581    0    1
1-2.0000000000000000+5 0.0000000000000000+0 0.0000000000000000+0
2-7.5800000000000000+2 0.0000000000000000+0 0.0000000000000000+
$(deleted remaining coordinates array)

```

```

define      node      set      icond1_nodes
1    to 1581
define      node      set      apply1_nodes
2    54    55    56
define      node      set      apply2_nodes
57
define      node      set      apply3_nodes
58
define      node      set      apply4_nodes
59
define      node      set      apply5_nodes
60
define      node      set      apply6_nodes
61    to    63
define      node      set      apply7_nodes
64
define      node      set      apply8_nodes
65
define      node      set      apply9_nodes
66
define      node      set      apply10_nodes
67    68
define      node      set      apply11_nodes
69    to    71
define      node      set      apply12_nodes
72    73
define      node      set      apply13_nodes
74    to    79
define      node      set      apply14_nodes
80    to    86
define      node      set      apply15_nodes
87    to    93

```

```

define      node      set      apply16_nodes
   3      94      95      96      97      98      99      100      101      102
define      edgemt      set      apply17_edges
   1:0      2:0      3:0      4:0      5:0      6:0      7:0      8:0
c
   9:0      10:0      11:0      12:0      13:0      14:0      15:0
16:0 c
   17:0      18:0      19:0      20:0      21:0      22:0      23:0
24:0 c
   25:0      26:0      27:0      28:0      29:0      30:0      1471:2
1472:2 c
   1473:2      1474:2      1475:2      1476:2      1477:2      1478:2
1479:2      1480:2 c
   1481:2      1482:2      1483:2      1484:2      1485:2      1486:2
1487:2      1488:2 c
   1489:2      1490:2      1491:2      1492:2      1493:2      1494:2
1495:2      1496:2 c
   1497:2      1498:2      1499:2      1500:2
define      edgemt      set      apply18_edges
   1:3      31:3      61:3      91:3      121:3      151:3      181:3
211:3 c
   241:3      271:3      301:3      331:3      361:3      391:3      421:3
451:3 c
   481:3      511:3      541:3      571:3      601:3      631:3      661:3
691:3 c
   721:3      751:3      781:3      811:3      841:3      871:3      901:3
931:3 c
   961:3      991:3      1021:3      1051:3      1081:3      1111:3
1141:3      1171:3 c
   1201:3      1231:3      1261:3      1291:3      1321:3      1351:3
1381:3      1411:3 c
   1441:3      1471:3
isotropic

   1      0      0      0      0material1
9.3000000000000001+0 1.0000000000000000+3 9.500000000000000+2
0.0000000000000000+0 0.0000000000000000+0 0.0000000000000000+0
0.0000000000000000+0
   0      0      0      0      0      0      0
   1      to      1500
geometry

```


0.0000000000000000+0 0.0000000000000000+0 0.0000000000000000+0
0.0000000000000000+0 0.0000000000000000+0 0.0000000000000000+0
0.0000000000000000+0

1 to 1500							
temperature effects				data			
22	22	0	0	0	0	1	0
9.3000000000000000+0				0.0000000000000000+2			
9.3000000000000000+0				0.7000000000000000+2			
8.1375000000000000+0				0.8000000000000000+2			
7.2333000000000000+0				0.9000000000000000+2			
6.5100000000000000+0				1.0000000000000000+2			
5.918181818181818+0				1.1000000000000000+2			
5.4250000000000000+0				1.2000000000000000+2			
5.0077000000000000+0				1.3000000000000000+2			
4.6500000000000000+0				1.4000000000000000+2			
4.3400000000000000+0				1.5000000000000000+2			
4.0687500000000000+0				1.6000000000000000+2			
3.8294100000000000+0				1.7000000000000000+2			
3.616666666666666+0				1.8000000000000000+2			
3.4263000000000000+0				1.9000000000000000+2			
3.2550000000000000+0				2.0000000000000000+2			
3.1000000000000000+0				2.1000000000000000+2			
2.9591000000000000+0				2.2000000000000000+2			
2.8300000000000000+0				2.3000000000000000+2			
2.7125000000000000+0				2.4000000000000000+2			
2.6040000000000000+0				2.5000000000000000+2			
2.5040000000000000+0				2.6000000000000000+2			
2.5040000000000000+0				2.6000000000000000+4			
6.6320000000000000+3				0.0000000000000000+2			
6.6320000000000000+3				0.7000000000000000+2			
6.6320000000000000+3				0.8000000000000000+2			
6.6320000000000000+3				0.9000000000000000+2			
5.9680000000000000+3				1.0000000000000000+2			
5.4260000000000000+3				1.1000000000000000+2			
4.9740000000000000+3				1.2000000000000000+2			
4.5910000000000000+3				1.3000000000000000+2			
4.2630000000000000+3				1.4000000000000000+2			
3.9790000000000000+3				1.5000000000000000+2			
3.7300000000000000+3				1.6000000000000000+2			
3.5110000000000000+3				1.7000000000000000+2			
3.3160000000000000+3				1.8000000000000000+2			
3.1410000000000000+3				1.9000000000000000+2			
2.9840000000000000+3				2.0000000000000000+2			

2.842000000000000+3	2.100000000000000+2
2.713000000000000+3	2.200000000000000+2
2.595000000000000+3	2.300000000000000+2
2.487000000000000+3	2.400000000000000+2
2.387000000000000+3	2.500000000000000+2
2.296000000000000+3	2.600000000000000+2
2.296000000000000+3	2.600000000000000+4

initial temp

1	0	0	0	0	0	icond1
9.000000000000000+1						
0						
2						

icond1_nodes
fixed temperature

1	0	0	0	0	0	0	apply1
1.580000000000000+2							
0							
1							
2							

apply1_nodes

1	0	0	0	0	0	0	apply2
1.540000000000000+2							
0							
1							
2							

apply2_nodes

1	0	0	0	0	0	0	apply3
1.470000000000000+2							
0							
1							
2							

apply3_nodes

1	0	0	0	0	0	0	apply4
1.350000000000000+2							
0							
1							
2							

apply4_nodes

1	0	0	0	0	0	0	apply5
1.160000000000000+2							
0							

```

1
2
apply5_nodes
1 0 0 0 0 0 apply6
9.400000000000000+1
0
1
2
$(apply6 - apply12 are removed; they are identical to apply5)
apply13_nodes
1 0 0 0 0 0 apply14
1.000000000000000+2
0
1
2
apply14_nodes
1 0 0 0 0 0 apply15
1.000000000000000+2
0
1
2
apply15_nodes
1 0 0 0 0 0 apply16
1.000000000000000+2
0
1
2
apply16_nodes
dist fluxes
1 0 0 0 0 0 apply17
0.000000000000000+0
0
0 10
13
apply17_edges
1 0 0 0 0 0 apply18
4.000000000000000-3
0
0 10
13
apply18_edges
loadcase job1

```

```

19
icond1
apply1
apply2
apply3
apply4
apply5
apply6
apply7
apply8
apply9
apply10
apply11
apply12
apply13
apply14
apply15
apply16
apply17
apply18
no print
post
    0   16   17   0   0   19   20   0   1   0   0   0   0   0
0   0
parameters
1.000000000000000+0 1.000000000000000+9 1.000000000000000+2
1.000000000000000+6 2.500000000000000-1 5.000000000000000-1
1.500000000000000+0-5.000000000000000-1
8.625000000000000+0 2.000000000000000+1 1.000000000000000-4
1.000000000000000-6 1.000000000000000+0 1.000000000000000-4
8.314000000000000+0 2.731500000000000+2 5.000000000000000-1
0.000000000000000+0 5.670510000000000-8 1.438769000000000-2
2.997900000000000+8 1.000000000000000+30
0.000000000000000+0 0.000000000000000+0 1.000000000000000+2
0.000000000000000+0 1.000000000000000+0-2.000000000000000+0
1.000000000000000+6
0.000000000000000+0 0.000000000000000+0 1.256637061000000-6 8.85418781700000-
12 1.200000000000000+2
end option
$.....
$....start of loadcase lcase1
title          lcase1
loadcase       lcase1

```

```

18
apply1
apply2
apply3
apply4
apply5
apply6
apply7
apply8
apply9
apply10
apply11
apply12
apply13
apply14
apply15
apply16
apply17
apply18
control
  99999  10  0  0  0  0  0  0  1  0  0  0
2.000000000000000+1 1.000000000000000+2 0.000000000000000+0
1.000000000000000+2 1.000000000000000-1 1.000000000000000-1 1.000000000000000-
1 1.000000000000000+30
parameters
1.000000000000000+0 1.000000000000000+9 1.000000000000000+2
1.000000000000000+6 2.500000000000000-1 5.000000000000000-1
1.500000000000000+0-5.000000000000000-1
8.625000000000000+0 2.000000000000000+1 1.000000000000000-4
1.000000000000000-6 1.000000000000000+0 1.000000000000000-4
8.314000000000000+0 2.731500000000000+2 5.000000000000000-1
0.000000000000000+0 5.670510000000000-8 1.438769000000000-2
2.997900000000000+8 1.000000000000000+30
0.000000000000000+0 0.000000000000000+0 1.000000000000000+2
0.000000000000000+0 1.000000000000000+0-1.000000000000000+0
1.000000000000000+6
0.000000000000000+0 0.000000000000000+0 1.256637061000000-6 8.85418781700000-
12 1.200000000000000+2
steady state
continue
$....end of loadcase lcase1
$.....
$(repeat the previous 45 lines x19)

```

B. Appendix B. for Chapter II: Mechanical File Example for Crater Relaxation:

Example: Sinlap crater (radius 40 km) filled with a maximum thickness of 400 m of sand (158 K), using a sand density of 200 kg m⁻³.

```

title          job1
$....MARC input file produced by Marc Mentat 2010.2.0 (64bit)
$.....
$....input file using extended precision
extended
$.....
sizing          0   1500   1581   164
alloc          25
elements        10
version         11
table           0   0   2   1   1   0   0   1
processor        1   1   1   0
$no list
constant d
assumed st
large stra       1   0
follow for       1   0   0
creep            0   0   0   0
all points
no echo          1   2   3
setname          16
end
$.....
solver
  8   0   0   0   0   0   0   0   0   0   0   0   0   0   0   0
0
optimize        11
connectivity
  0   0   1
  1  10   1  103  104   5
  2  10  103  105  106  104
$(deleted remaining connectivity array)

coordinates
  3  1581   0   1
  1-2.0000000000000000+5 0.0000000000000000+0 0.0000000000000000+0
  2-7.5800000000000000+2 0.0000000000000000+0 0.0000000000000000+0
$(deleted remaining coordinates array)

```

```

define      element      set      icond1_elements
  1      to      1500
define      node      set      apply1_nodes
  1      4      5      6      7      8      9      10      11      12      13      14
15 c
  16      17      18      19      20      21      22      23      24      25      26
27      28 c
  29      30      31      32      33      34      35      36      37      38      39
40      41 c
  42      43      44      45      46      47      48      49      50      51      52
53
define      node      set      apply2_nodes
  1      2      3      4      103      105      107      109      111      113      115
117      119 c
  121      123      125      127      129      131      133      135      137      139
141      143      145 c
  147      149      151      153      155      157      159      1553      1554      1555
1556      1557      1558 c
  1559      1560      1561      1562      1563      1564      1565      1566      1567
1568      1569      1570      1571 c
  1572      1573      1574      1575      1576      1577      1578      1579      1580
1581
define      edgmt      set      apply3_edges
  30:1
define      edgmt      set      apply4_edges
  60:1
define      edgmt      set      apply5_edges
  90:1
define      edgmt      set      apply6_edges
  120:1
define      edgmt      set      apply7_edges
  150:1
define      edgmt      set      apply8_edges
  180:1
define      edgmt      set      apply9_edges
  210:1
define      edgmt      set      apply10_edges
  240:1
define      edgmt      set      apply11_edges
  270:1
define      element      set      apply12_elements
  1      to      1500

```

isotropic

```
1elastic 0 0 0 0material1
7.827000000000000+9 4.999900000000000-1 9.500000000000000+2
0.000000000000000+0 0.000000000000000+0 0.000000000000000+0
0.000000000000000+0 0.000000000000000+0
0 0 0 0 0 0 0 0
1 to 1500
creep data
0 0 0 0 0.000000000000000+0
0.000000000000000+0 0.000000000000000+0 0 1 0
0 0 0 0 0
geometry
0.000000000000000+0 1.000000000000000+0 0.000000000000000+0
0.000000000000000+0 0.000000000000000+0 0.000000000000000+0
0.000000000000000+0
1 to 1500
fixed disp
1 0 0 0 1 0apply1
0.000000000000000+0 0.000000000000000+0
0 0
1 2
2
apply1_nodes
1 0 0 0 1 0apply2
0.000000000000000+0
0
2
2
apply2_nodes
dist loads
1 0 0 0 0 0apply3
1.0800000000000002+5
0
0 1
13
apply3_edges
1 0 0 0 0 0apply4
1.0800000000000002+5
0
```



```

0    1
13
apply4_edges
1    0    0    0    0    0    0apply5
1.0700000000000002+5
0
0    1
13
apply5_edges
1    0    0    0    0    0    0apply6
1.0300000000000002+5
0
0    1
13
apply6_edges
1    0    0    0    0    0    0apply7
9.5000000000000002+4
0
0    1
13
apply7_edges
1    0    0    0    0    0    0apply8
7.9600000000000002+4
0
0    1
13
apply8_edges
1    0    0    0    0    0    0apply9
5.3300000000000000+4
0
0    1
13
apply9_edges
1    0    0    0    0    0    0apply10
1.1900000000000001+4
0
0    1
13
apply10_edges
1    0    0    0    0    0    0apply11
0.000000000000000+1
0
0    1

```

```

13
apply11_edges
1 0 0 0 0 0 apply12
-1.3520000000000000+0 0.0000000000000000+0
0 0
0 102
1
apply12_elements
initial state

1 3 1 0 0 0 icond1
loadcase job1
13
icond1
apply1
apply2
apply3
apply4
apply5
apply6
apply7
apply8
apply9
apply10
apply11
apply12
no print
post
5 16 17 0 0 19 20 0 1 0 0 0 0 0
0 0
18 0
48 0
58 0
311 0
411 0
9 0
-1 0 differential stress
-2 0 Viscosity
parameters
1.0000000000000000+0 1.0000000000000000+9 1.0000000000000000+2
1.0000000000000000+6 2.5000000000000000-1 5.0000000000000000-1
1.5000000000000000+0-5.0000000000000000-1

```

```

8.625000000000000+0 2.000000000000000+1 1.000000000000000-4
1.000000000000000-6 1.000000000000000+0 1.000000000000000-4
8.314000000000000+0 2.731500000000000+2 5.000000000000000-1
0.000000000000000+0 5.670510000000000-8 1.438769000000000-2
2.997900000000000+8 1.000000000000000+30
0.000000000000000+0 0.000000000000000+0 1.000000000000000+2
0.000000000000000+0 1.000000000000000+0-2.000000000000000+0
1.000000000000000+6
0.000000000000000+0 0.000000000000000+0 1.256637061000000-6 8.85418781700000-
12 1.200000000000000+2
end option
$.....
$....start of loadcase lcase1
title      lcase1
loadcase   lcase1
      12
apply1
apply2
apply3
apply4
apply5
apply6
apply7
apply8
apply9
apply10
apply11
apply12
control
      99999      10      0      0      0      1      0      0      1      0      1      0
1.000000000000000-1 0.000000000000000+0 0.000000000000000+0
0.000000000000000+0 0.000000000000000+0 0.000000000000000+0
0.000000000000000+0 0.000000000000000+0
parameters
1.000000000000000+0 1.000000000000000+9 1.000000000000000+2
1.000000000000000+6 2.500000000000000-1 5.000000000000000-1
1.500000000000000+0-5.000000000000000-1
8.625000000000000+0 2.000000000000000+1 1.000000000000000-4
1.000000000000000-6 1.000000000000000+0 1.000000000000000-4
8.314000000000000+0 2.731500000000000+2 5.000000000000000-1
0.000000000000000+0 5.670510000000000-8 1.438769000000000-2
2.997900000000000+8 1.000000000000000+30

```

```

0.0000000000000000+0 0.0000000000000000+0 1.0000000000000000+2
0.0000000000000000+0 1.0000000000000000+0-1.0000000000000000+0
1.0000000000000000+6
0.0000000000000000+0 0.0000000000000000+0 1.256637061000000-6 8.85418781700000-
12 1.2000000000000000+2
creep increment
0.000000000000000000000000000000+0
continue
$....end of loadcase lcase1
$.....
$(repeat previous 41 lines x19)

$....start of loadcase lcase1
title          lcase1
loadcase       lcase1
    12
apply1
apply2
apply3
apply4
apply5
apply6
apply7
apply8
apply9
apply10
apply11
apply12
control
    99999    10    0    0    0    1    0    0    1    0    1    0
1.0000000000000000-1 0.0000000000000000+0 0.0000000000000000+0
0.0000000000000000+0 0.0000000000000000+0 0.0000000000000000+0
0.0000000000000000+0 0.0000000000000000+0
parameters
1.0000000000000000+0 1.0000000000000000+9 1.0000000000000000+2
1.0000000000000000+6 2.5000000000000000-1 5.0000000000000000-1
1.5000000000000000+0-5.0000000000000000-1
8.6250000000000000+0 2.0000000000000000+1 1.0000000000000000-4
1.0000000000000000-6 1.0000000000000000+0 1.0000000000000000-4
8.3140000000000000+0 2.7315000000000000+2 5.0000000000000000-1
0.0000000000000000+0 5.6705100000000000-8 1.4387690000000000-2
2.9979000000000000+8 1.0000000000000000+30

```

```

0.0000000000000000+0 0.0000000000000000+0 1.0000000000000000+2
0.0000000000000000+0 1.0000000000000000+0-1.0000000000000000+0
1.0000000000000000+6
0.0000000000000000+0 0.0000000000000000+0 1.256637061000000-6 8.85418781700000-
12 1.2000000000000000+2
post increment
1111111111
creep increment
0.000000000000000000000000000000+0
continue
$....end of loadcase lcase1
$....start of loadcase lcase1
title          lcase1
loadcase       lcase1
    12
apply1
apply2
apply3
apply4
apply5
apply6
apply7
apply8
apply9
apply10
apply11
apply12
control
    999999    10    0    0    0    1    0    0    1    0    1    0
1.0000000000000000-1 0.0000000000000000+0 0.0000000000000000+0
0.0000000000000000+0 0.0000000000000000+0 0.0000000000000000+0
0.0000000000000000+0 0.0000000000000000+0
parameters
1.0000000000000000+0 1.0000000000000000+9 1.0000000000000000+2
1.0000000000000000+6 2.5000000000000000-1 5.0000000000000000-1
1.5000000000000000+0-5.0000000000000000-1
8.6250000000000000+0 2.0000000000000000+1 1.0000000000000000-4
1.0000000000000000-6 1.0000000000000000+0 1.0000000000000000-4
8.3140000000000000+0 2.7315000000000000+2 5.0000000000000000-1
0.0000000000000000+0 5.6705100000000000-8 1.4387690000000000-2
2.9979000000000000+8 1.0000000000000000+30

```

```

0.0000000000000000+0 0.0000000000000000+0 1.0000000000000000+2
0.0000000000000000+0 1.0000000000000000+0-1.0000000000000000+0
1.0000000000000000+6
0.0000000000000000+0 0.0000000000000000+0 1.256637061000000-6 8.85418781700000-
12 1.2000000000000000+2
auto creep
3.15576000000000000000000000000000+12 7.889460000000000000000000000000+16 999999 40
0 0 0.0000000000000000+0
5.0000000000000000-1 1.0000000000000000-1 5.0000000000000001-2 0 0
continue
$(repeat previous 40 lines, changing auto creep to output desired times)

```

C. Appendix C. for Chapter II: Example Subroutine File

This subroutine is written in Fortran by Andrew Dombard and edited by Lauren Schurmeier. Lines starting with C are not read.

Example: Sinlap crater (radius 40 km) filled with a maximum thickness of 400 m of sand (158 K), using a sand density of 200 kg m^{-3} .

```

SUBROUTINE CRPLAW(EQCP,EQCPNC,STR,CRPE,T,DT,TIMINC,CPTIM,M,NN,KC,
*      MATS,NDI,NSHEAR)
C
      IMPLICIT REAL*8 (A-H,O-Z)
C
      DIMENSION T(3),DT(1),STR(1),CRPE(1)
C
      GS = 1.d-3
      RT = 8.31451d0*DT(1)
      dis = (4.d5)*((T(1)/1.0d+6)**(4.d0))*dexp(-60.d3/RT)
      dif = (3.02d-8)*(T(1)/(DT(1)*GS*GS))*(dexp(-59.4d3/RT) +
*      2.84d-9*dexp(-60.d3/RT)/GS)
      GBS = ((3.9d-3)/(GS**1.4d0))*((T(1)/1.0d+6)**(1.8d0))*
*      dexp(-49.d3/RT)
      ES = (5.5d+7)*((T(1)/1.0d+6)**(2.4d0))*dexp(-60.d3/RT)
C
      rate = 1.d0/(1.d0/GBS + 1.d0/ES) + dis + dif
      viscmmin = 1.d18
      if (cptim.gt.3.15576d11) viscmmin = 1.d18
      if (cptim.gt.3.15576d12) viscmmin = 1.d19
      if (cptim.gt.3.15576d13) viscmmin = 1.d20
      if (cptim.gt.3.15576d14) viscmmin = 1.d21

```

```

    if (cptim.gt.3.15576d15) viscmin = 1.d22
    eta = T(1)/(3.d0*rate)
    if (eta.lt.viscmin) rate = T(1)/(3.d0*viscmin)
    EQCPNC = TIMINC*rate
C
    RETURN
    END
C
C-----
C
    SUBROUTINE UINSTR(S,NDI,NSHEAR,NI,NNI,KCI,XINTP,NCRDI,INC,TIME,TIMEINC)
C
    IMPLICIT REAL*8 (A-H,O-Z)
C
    DIMENSION S(1),XINTP(NCRD),NI(2)
    DIMENSION CCNODE(12)
C
    parameter(GP = 0.577350269189626d0)
C
    include '/opt/msc/marc2010.2/common/lass'
    include '/opt/msc/marc2010.2/common/dimen'
    include '/opt/msc/marc2010.2/common/space'
    include '/opt/msc/marc2010.2/common/blnk'
    include '/opt/msc/marc2010.2/common/array2'
    include '/opt/msc/marc2010.2/common/spacevec'
    include '/opt/msc/marc2010.2/common/strvar'
C
    if (nnl.eq.1) then
        eta1 = -1.d0*GP
        eta2 = -1.d0*GP
    endif
    if (nnl.eq.2) then
        eta1 = 1.d0*GP
        eta2 = -1.d0*GP
    endif
    if (nnl.eq.3) then
        eta1 = -1.d0*GP
        eta2 = 1.d0*GP
    endif
    if (nnl.eq.4) then
        eta1 = 1.d0*GP
        eta2 = 1.d0*GP
    endif
    endif

```

```

C      Quadralateral Elements
      x = 0.d0
      y = 0.d0
      JRDPRE = 0
C      CALL VECFTC(CCNODE,VARS(IXORD),NCRDMX,NCRD,lm(1),JRDPRE,2,1)
      CALL VECFTC(CCNODE,XORD_D,NCRDMX,NCRD,lm(1),JRDPRE,2,1)
      x = x + (1.d0 - eta1)*(1.d0 - eta2)*ccnode(1)/4.d0
      y = y + (1.d0 - eta1)*(1.d0 - eta2)*ccnode(2)/4.d0
      JRDPRE = 0
C      CALL VECFTC(CCNODE,VARS(IXORD),NCRDMX,NCRD,lm(2),JRDPRE,2,1)
      CALL VECFTC(CCNODE,XORD_D,NCRDMX,NCRD,lm(2),JRDPRE,2,1)
      x = x + (1.d0 + eta1)*(1.d0 - eta2)*ccnode(1)/4.d0
      y = y + (1.d0 + eta1)*(1.d0 - eta2)*ccnode(2)/4.d0
      JRDPRE = 0
C      CALL VECFTC(CCNODE,VARS(IXORD),NCRDMX,NCRD,lm(3),JRDPRE,2,1)
      CALL VECFTC(CCNODE,XORD_D,NCRDMX,NCRD,lm(3),JRDPRE,2,1)
      x = x + (1.d0 + eta1)*(1.d0 + eta2)*ccnode(1)/4.d0
      y = y + (1.d0 + eta1)*(1.d0 + eta2)*ccnode(2)/4.d0
      JRDPRE = 0
C      CALL VECFTC(CCNODE,VARS(IXORD),NCRDMX,NCRD,lm(4),JRDPRE,2,1)
      CALL VECFTC(CCNODE,XORD_D,NCRDMX,NCRD,lm(4),JRDPRE,2,1)
      x = x + (1.d0 - eta1)*(1.d0 + eta2)*ccnode(1)/4.d0
      y = y + (1.d0 - eta1)*(1.d0 + eta2)*ccnode(2)/4.d0
C
C      Stress Profile Parameters:
      rho = 950.d0
      g = 1.352d0
C
      S(1) = rho*g*y
      S(2) = rho*g*y
      S(3) = rho*g*y
C
      RETURN
      END
C
C-----
C
      subroutine impd(n,dd,td,xord,f,v,a,nd,ncrd)
C
      IMPLICIT REAL*8 (A-H,O-Z)
C
      dimension dd(nd),td(nd),xord(ncrd),f(nd),v(nd),a(nd),n(2)
      dimension d(12),h(12)

```



```

C      include '/opt/msc/marc2010.2/common/creeps'
      include '/opt/msc/marc2010.2/common/concom'
C
      open(10,file='sinlap_4_pressure_400d_158K.txt',status='unknown')
      open(11,file='sinlap_4_pressure_400d_158K-shape.txt',status='unknown')
C
      Radius = 40.d3
      dr = Radius/10.d0
      dt = 1096.d0
      da = 758.d0
      do i = 1,11
        h(i) = dt*(dble(i-1)*dr/Radius)**4.d0 - da
      enddo
      if (n(1).eq.2) d(1) = td(1)
      if (n(1).eq.3) then
        dl = td(1)
        dmin = h(1) + d(1) - dl + 1.d6
      endif
      do i = 2,11
        j = i + 52
        if (n(1).eq.j) d(i) = td(1)
        dtest = h(i) + d(i) - dl + 1.d6
        if (dtest.lt.dmin) dmin = dtest
      enddo
      if (inc.eq.20) then
        do i=1,11
          write(11,*)inc,i,dble(i-1)*dr/1.d3,h(i)
        enddo
      endif
      if (inc.ge.20.and.n(1).eq.63) then
        dmin = dmin - 1.d6
        write(10,666)inc,cptim/3.15576d7,dmin
      endif
666  format(i6,e13.5,f9.2)
C
      return
      end
C
C-----
C
      subroutine plotv(v,s,sp,etot,eplas,ecreep,t,m,nn,layer,ndi,
*      nshear,jplbcd)

```

```

C      SUBROUTINE PLOTV(V,S,SP,ETOT,EPLAS,ECREEP,T,M,NN,LAYER,NDI,
C      *          NSHEAR,JPLNCD)
C
C      include '/opt/msc/marc2010.2/common/implicit'
C      IMPLICIT REAL*8 (A-H,O-Z)
C      dimension s(*),etot(*),eplas(*),ecreep(*),sp(*),m(2)
C      DIMENSION S(1),SP(1),ETOT(1),EPLAS(1),ECREEP(1),M(2)
C
C      if (jplnctd.lt.2) then
C          V = S(2) - S(1)
C      else
C          smean = (s(1) + s(2) + s(3))/3.d0
C          s1 = s(1) - smean
C          s2 = s(2) - smean
C          s3 = s(3) - smean
C          es = dsqrt((s1*s1 + s2*s2 + s3*s3)/2.d0 + s(4)*s(4))
C      GS = 1.d-3
C      RT = 8.31451d0*T
C      dis = (4.d5)*((es/1.0d+6)**(4.d0))*dexp(-60.d3/RT)
C      dif = (3.02d-8)*(es/(T*GS*GS))*(dexp(-59.4d3/RT) +
C      *          2.84d-9*dexp(-60.d3/RT)/GS)
C      GBS = ((3.9d-3)/(GS**1.4d0))*((es/1.0d+6)**(1.8d0))*
C      *          dexp(-49.d3/RT)
C      ESS = (5.5d+7)*((es/1.0d+6)**(2.4d0))*dexp(-60.d3/RT)
C      r = 1.d0/(1.d0/GBS + 1.d0/ESS) + dis + dif
C      V = dlog10(dabs(es)) - dlog10(dabs(3.d0*r))
C      endif
C
C      RETURN
C      END
C
C=====
=====

```

D. Appendix D. for Chapter III: Mountain Shape Approximation as a Gaussian

For the 350 km wide mountain:

$$X_{\text{surface}} = 600 * e^{(-0.5 * (y/71000)^2)}$$

$$X_{\text{root}} = -100,000 - 5700 * e^{(-0.5 * (y/71000)^2)}$$

For the 200 km wide mountain:

$$X_{\text{surface}} = 1,000 * e^{(-0.5 * (y/41000)^2)}$$

$$X_{\text{root}} = -100,000 - 9500 * e^{(-0.5 * (y/41000)^2)}$$

E. Appendix E. for Chapter III: Data Comparing Actual Mountain Root with an Isostatically Equilibrated Root

Table 1: Comparison of the actual maximum depth of the mountain root with what would be expected if the root were in isostatic equilibrium at various times in the simulation.

		600 m Initial Height		1 km Initial Height	
		4 mW	6.6 mW	4 mW	6.6 mW
Surface	10 kyr height	580	526	986	908
	dh	20	74	14	92
	1 Myr height	560	449	960	752
	dh	40	151	40	248
	1 Gyr height	489	296	827	477
	dh	111	304	173	523
	3 Gyr height	461	263	770	425
	dh	139	337	230	575
Root	10 kyr depth	-1.06E+05	-1.0484E+05	-1.09E+05	-1.09E+05
	dH	-4	-863	-30	-160
	Hi	-105511	-104996	-109369	-108628
	dHi	-189	-704	-131	-872
	Error	-185	160	-101	-712
	% Error	98%	-23%	77%	82%
	1 Myr depth	-1.05E+05	-1.0056E+05	-1.08E+05	-1.02E+05
	dH	-759	-5136	-1520	-7130
	Hi	-105320	-104266	-109122	-107148
	dHi	-380	-1435	-378	-2352
	Error	379	3702	1142	4778
	% Error	-100%	-258%	-302%	-203%
	1 Gyr depth	-1.01E+05	-1.0018E+05	-1.02E+05	-1.00E+05
	dH	-4576	-5524	-7470	-9030
	Hi	-104646	-102812	-107855	-104536
	dHi	-1055	-2888	-1645	-4964
	Error	3521	2636	5825	4066
	% Error	-334%	-91%	-354%	-82%
	3 Gyr depth	-1.01E+05	-1.0013E+05	-1.01E+05	-1.00E+05
	dH	-4954	-5565	-8160	-9180
	Hi	-104380	-102498	-107317	-104035

	dHi	-1321	-3202	-2183	-5465
	Error	3633	2363	5977	3715
	% Error	-275%	-74%	-274%	-68%

Simulated mountain (surface) heights and root depths at each time increment are in bold.

dh: the difference in the current height from the initial mountain height (600 m or 1 km)

dHi: the difference in the depth from the initial root depth (-105,700 m for 600 m initial height, and -109,500 for a 1 km initial height).

H_i: depth expected (H) if in isostatic equilibrium with the current surface elevation (h), where $H = -100000 \text{ m} - ((h \cdot 950 \text{ kg m}^{-3}) / (1050 \text{ kg m}^{-3} - 950 \text{ kg m}^{-3}))$.

dHi: the difference in depth of the initial depth (-105,700 m for 600 m initial height, and -109,500 for a 1 km initial height) to the isostatic depth.

Error: dH - dHi

% Error: $((dH - dHi) / dHi) \cdot 100\%$

F. Appendix F. for Chapter III: Example Mountain Subroutine File for Water Ice

This subroutine is written in Fortran by Andrew Dombard and edited by Lauren Schurmeier. Lines starting with C are not read.

```

C
      SUBROUTINE CRPLAW(EQCP,EQCPNC,STR,CRPE,T,DT,TIMINC,CPTIM,M,NN,KC,
*
          MATS,NDI,NSHEAR)
C
      IMPLICIT REAL*8 (A-H,O-Z)
C
      DIMENSION T(3),DT(1),STR(1),CRPE(1)
C
      GS = 1.d-3
      RT = 8.31451d0*DT(1)
      dis = (4.d5)*((T(1)/1.0d+6)**(4.d0))*dexp(-60.d3/RT)
      dif = (3.02d-8)*(T(1)/(DT(1)*GS*GS))*(dexp(-59.4d3/RT) +
*
          2.84d-9*dexp(-60.d3/RT)/GS)
      GBS = ((3.9d-3)/(GS**1.4d0))*((T(1)/1.0d+6)**(1.8d0))*
*
          dexp(-49.d3/RT)
      ES = (5.5d+7)*((T(1)/1.0d+6)**(2.4d0))*dexp(-60.d3/RT)
C
      rate = 1.d0/(1.d0/GBS + 1.d0/ES) + dis + dif
      viscmin = 1.d18
      if (cptim.gt.3.15576d11) viscmin = 1.d18

```

```

      if (cptim.gt.3.15576d12) viscmn = 1.d19
      if (cptim.gt.3.15576d13) viscmn = 1.d20
      if (cptim.gt.3.15576d14) viscmn = 1.d21
      if (cptim.gt.3.15576d15) viscmn = 1.d22
      eta = T(1)/(3.d0*rate)
      if (eta.lt.viscmn) rate = T(1)/(3.d0*viscmn)
      EQCPNC = TIMINC*rate
C
      RETURN
      END
C
C-----
C
      SUBROUTINE UINSTR(S,NDI,NSHEAR,NI,NNI,KCI,XINTP,NCRDI,INC,TIME,TIMEINC)
C
      IMPLICIT REAL*8 (A-H,O-Z)
C
      DIMENSION S(1),XINTP(NCRD),NI(2)
      DIMENSION CCNODE(12)
C
      parameter(GP = 0.577350269189626d0)
C
      include '/opt/msc/marc2010.2/common/lass'
      include '/opt/msc/marc2010.2/common/dimen'
      include '/opt/msc/marc2010.2/common/space'
      include '/opt/msc/marc2010.2/common/blnk'
      include '/opt/msc/marc2010.2/common/array2'
      include '/opt/msc/marc2010.2/common/spacevec'
      include '/opt/msc/marc2010.2/common/strvar'
C
      if (nnl.eq.1) then
         eta1 = -1.d0*GP
         eta2 = -1.d0*GP
      endif
      if (nnl.eq.2) then
         eta1 = 1.d0*GP
         eta2 = -1.d0*GP
      endif
      if (nnl.eq.3) then
         eta1 = -1.d0*GP
         eta2 = 1.d0*GP
      endif
      if (nnl.eq.4) then

```

```

        eta1 = 1.d0*GP
        eta2 = 1.d0*GP
    endif
C    Quadralateral Elements
    x = 0.d0
    y = 0.d0
    JRDPRE = 0
C    CALL VECFTC(CCNODE,VARS(IXORD),NCRDMX,NCRD,lm(1),JRDPRE,2,1)
    CALL VECFTC(CCNODE,XORD_D,NCRDMX,NCRD,lm(1),JRDPRE,2,1)
    x = x + (1.d0 - eta1)*(1.d0 - eta2)*ccnode(1)/4.d0
    y = y + (1.d0 - eta1)*(1.d0 - eta2)*ccnode(2)/4.d0
    JRDPRE = 0
C    CALL VECFTC(CCNODE,VARS(IXORD),NCRDMX,NCRD,lm(2),JRDPRE,2,1)
    CALL VECFTC(CCNODE,XORD_D,NCRDMX,NCRD,lm(2),JRDPRE,2,1)
    x = x + (1.d0 + eta1)*(1.d0 - eta2)*ccnode(1)/4.d0
    y = y + (1.d0 + eta1)*(1.d0 - eta2)*ccnode(2)/4.d0
    JRDPRE = 0
C    CALL VECFTC(CCNODE,VARS(IXORD),NCRDMX,NCRD,lm(3),JRDPRE,2,1)
    CALL VECFTC(CCNODE,XORD_D,NCRDMX,NCRD,lm(3),JRDPRE,2,1)
    x = x + (1.d0 + eta1)*(1.d0 + eta2)*ccnode(1)/4.d0
    y = y + (1.d0 + eta1)*(1.d0 + eta2)*ccnode(2)/4.d0
    JRDPRE = 0
C    CALL VECFTC(CCNODE,VARS(IXORD),NCRDMX,NCRD,lm(4),JRDPRE,2,1)
    CALL VECFTC(CCNODE,XORD_D,NCRDMX,NCRD,lm(4),JRDPRE,2,1)
    x = x + (1.d0 - eta1)*(1.d0 + eta2)*ccnode(1)/4.d0
    y = y + (1.d0 - eta1)*(1.d0 + eta2)*ccnode(2)/4.d0
C
C    Stress Profile Parameters:
    rho = 950.d0
    g = 1.352d0
C
    S(1) = rho*g*y
    S(2) = rho*g*y
    S(3) = rho*g*y
C
    RETURN
    END
C
C-----
C
    subroutine impd(n,dd,td,xord,f,v,a,nd,ncrd)
C
    IMPLICIT REAL*8 (A-H,O-Z)

```

```

C      dimension dd(nd),td(nd),xord(ncrd),f(nd),v(nd),a(nd),n(2)
C
C      include '/opt/msc/marc2010.2/common/creeps'
C      include '/opt/msc/marc2010.2/common/concom'
C
C      open(10,file='file.txt',status='unknown')
C
C      d0 = 600.d0
C      if (n(1).eq.2) d1 = td(1)
C      if (n(1).eq.3) then
C          d2 = td(1)
C          dc = d0 + d1 - d2
C      if (inc.eq.20) de = dc
C      dn = dc/de
C      if (inc.ge.20) write(10,666)inc,cptim/3.15576d7,dc,1.d0 - dn
C      if (inc.ge.20) write(10,666)inc,cptim/3.15576d7,dc
C      endif
C666 format(i6,e13.5,f9.2,2f9.5)
666 format(i6,e13.5,f9.2)
C
C      return
C      end
C
C-----
C
C      subroutine plotv(v,s,sp,etot,eplas,ecreep,t,m,nn,layer,ndi,
*      nshear,jpltcd)
C      SUBROUTINE PLOTV(V,S,SP,ETOT,EPLAS,ECREEP,T,M,NN,LAYER,NDI,
C      *      NSHEAR,JPLNCD)
C
C      include '/opt/msc/marc2010.2/common/implicit'
C      IMPLICIT REAL*8 (A-H,O-Z)
C      dimension s(*),etot(*),eplas(*),ecreep(*),sp(*),m(2)
C      DIMENSION S(1),SP(1),ETOT(1),EPLAS(1),ECREEP(1),M(2)
C
C      if (jpltcd.lt.2) then
C          V = S(2) - S(1)
C      else
C          smean = (s(1) + s(2) + s(3))/3.d0
C          s1 = s(1) - smean
C          s2 = s(2) - smean
C          s3 = s(3) - smean

```

```

      es = dsqrt((s1*s1 + s2*s2 + s3*s3)/2.d0 + s(4)*s(4))
      GS = 1.d-3
      RT = 8.31451d0*T
      dis = (4.d5)*((es/1.0d+6)**(4.d0))*dexp(-60.d3/RT)
      dif = (3.02d-8)*(es/(T*GS*GS))*(dexp(-59.4d3/RT) +
*      2.84d-9*dexp(-60.d3/RT)/GS)
      GBS = ((3.9d-3)/(GS**1.4d0))*((es/1.0d+6)**(1.8d0))*
*      dexp(-49.d3/RT)
      ESS = (5.5d+7)*((es/1.0d+6)**(2.4d0))*dexp(-60.d3/RT)
      r = 1.d0/(1.d0/GBS + 1.d0/ESS) + dis + dif
      V = dlog10(dabs(es)) - dlog10(dabs(3.d0*r))
    endif
  C
    RETURN
  END
C
C=====
=====

```

G. Appendix G. for Chapter III: Example Mountain 1 Layer Thermal dat file

Example: For a 200 km wide mountain with a 600 m initial height and no ocean bouyancy

```

title      job1
$....MARC input file produced by Marc Mentat 2010.2.0 (64bit)
$.....
$....input file using extended precision
extended
$.....
sizing      0  4000  4141  202
alloc      25
elements    40
version     11
table       0   0   2   1   1   0   0   1
processor    1   1   1   0
$no list
heat        0   0   1   0   1   1
thermal
all points
no echo     1   2   3
setname     24
end
$.....
solver

```


8 0 0 0 0 0 0 0 0 0 0 0 0 0 0
0

optimize 11

connectivity

0 0 1
1 40 5 304 305 106
2 40 304 306 307 305

\$(deleted remaining connectivity array)

coordinates

3 4141 0 1
1-2.5000000000000000+5 0.0000000000000000+0 0.0000000000000000+0
2 6.0000000000000000+2 0.0000000000000000+0 0.0000000000000000+0

\$(deleted remaining coordinates array)

define	node			set	apply1_nodes					
	2	3	205	206	207	208	209	210	211	212
213	214	215	c							
	216	217	218	219	220	221	222	223	224	225
226	227	228	c							
	229	230	231	232	233	234	235	236	237	238
239	240	241	c							
	242	243	244	245	246	247	248	249	250	251
252	253	254	c							
	255	256	257	258	259	260	261	262	263	264
265	266	267	c							
	268	269	270	271	272	273	274	275	276	277
278	279	280	c							
	281	282	283	284	285	286	287	288	289	290
291	292	293	c							
	294	295	296	297	298	299	300	301	302	303
define	node			set	apply2_nodes					
	5	6	106	107	108	109	110	111	112	113
114	115	116	c							
	117	118	119	120	121	122	123	124	125	126
127	128	129	c							
	130	131	132	133	134	135	136	137	138	139
140	141	142	c							
	143	144	145	146	147	148	149	150	151	152
153	154	155	c							
	156	157	158	159	160	161	162	163	164	165
166	167	168	c							

	169	170	171	172	173	174	175	176	177	178
179	180	181	c							
	182	183	184	185	186	187	188	189	190	191
192	193	194	c							
	195	196	197	198	199	200	201	202	203	204
define	edgmt		set	apply3_edges						
	2001:3	2021:3		2041:3	2061:3		2081:3		2101:3	
2121:3	2141:3	c								
	2161:3	2181:3		2201:3	2221:3		2241:3		2261:3	
2281:3	2301:3	c								
	2321:3	2341:3		2361:3	2381:3		2401:3		2421:3	
2441:3	2461:3	c								
	2481:3	2501:3		2521:3	2541:3		2561:3		2581:3	
2601:3	2621:3	c								
	2641:3	2661:3		2681:3	2701:3		2721:3		2741:3	
2761:3	2781:3	c								
	2801:3	2821:3		2841:3	2861:3		2881:3		2901:3	
2921:3	2941:3	c								
	2961:3	2981:3		3001:3	3021:3		3041:3		3061:3	
3081:3	3101:3	c								
	3121:3	3141:3		3161:3	3181:3		3201:3		3221:3	
3241:3	3261:3	c								
	3281:3	3301:3		3321:3	3341:3		3361:3		3381:3	
3401:3	3421:3	c								
	3441:3	3461:3		3481:3	3501:3		3521:3		3541:3	
3561:3	3581:3	c								
	3601:3	3621:3		3641:3	3661:3		3681:3		3701:3	
3721:3	3741:3	c								
	3761:3	3781:3		3801:3	3821:3		3841:3		3861:3	
3881:3	3901:3	c								
	3921:3	3941:3		3961:3	3981:3					
define	node		set	icond1_nodes						
	1	to 4141								
define	edgmt		set	apply4_edges						
	1:0	2:0	3:0	4:0	5:0	6:0	7:0	8:0		
c										
	9:0	10:0	11:0	12:0	13:0	14:0	15:0			
16:0	c									
	17:0	18:0	19:0	20:0	1981:2	1982:2	1983:2			
1984:2	c									
	1985:2	1986:2	1987:2	1988:2	1989:2	1990:2				
1991:2	1992:2	c								

```

      1      0      0      0      0crust
9.3000000000000001+0 1.0000000000000000+3 9.500000000000000+2
0.0000000000000000+0 0.0000000000000000+0 0.0000000000000000+0
0.0000000000000000+0
      0      0      0      0      0      0      0
      1      to      2000
isotropic
```

```
0.0000000000000000+0 0.0000000000000000+0 0.0000000000000000+0
1.0000000000000000+0 0.0000000000000000+0 0.0000000000000000+0
0.0000000000000000+0
      1      to      4000
```

149

icond1_nodes

fixed temperature

```
1 0 0 0 0 0 apply1
9.400000000000000+1
0
1
2
```

apply1_nodes

```
1 0 0 0 0 0 apply2
1.760000000000000+2
0
1
2
```

apply2_nodes

dist fluxes

```
1 0 0 0 0 0 apply3
4.000000000000000-3
0
0 10
13
```

apply3_edges

```
1 0 0 0 0 0 apply4
0.000000000000000+0
0
0 10
13
```

apply4_edges

loadcase job1

5

icond1

apply1

apply2

apply3

apply4

no print

post

```
1 16 17 0 0 19 20 0 1 0 0 0 0 0
0 0
180 0
```

parameters

```

1.0000000000000000+0 1.0000000000000000+9 1.0000000000000000+2
1.0000000000000000+6 2.5000000000000000-1 5.0000000000000000-1
1.5000000000000000+0-5.0000000000000000-1
8.6250000000000000+0 2.0000000000000000+1 1.0000000000000000-4
1.0000000000000000-6 1.0000000000000000+0 1.0000000000000000-4
8.3140000000000000+0 2.7315000000000000+2 5.0000000000000000-1
0.0000000000000000+0 5.6705100000000000-8 1.4387690000000000-2
2.9979000000000000+8 1.0000000000000000+30
0.0000000000000000+0 0.0000000000000000+0 1.0000000000000000+2
0.0000000000000000+0 1.0000000000000000+0-2.0000000000000000+0
1.0000000000000000+6
0.0000000000000000+0 0.0000000000000000+0 1.256637061000000-6 8.85418781700000-
12 1.2000000000000000+2
end option
$.....
$....start of loadcase lcase1
title      lcase1
loadcase    lcase1
      4
apply1
apply2
apply3
apply4
control
      99999      10      0      0      0      0      0      0      1      0      0      0
2.0000000000000000+1 1.0000000000000000+2 0.0000000000000000+0
1.0000000000000000+2 1.0000000000000000-1 1.0000000000000000-1 1.0000000000000000-
1 1.0000000000000000+30
parameters
1.0000000000000000+0 1.0000000000000000+9 1.0000000000000000+2
1.0000000000000000+6 2.5000000000000000-1 5.0000000000000000-1
1.5000000000000000+0-5.0000000000000000-1
8.6250000000000000+0 2.0000000000000000+1 1.0000000000000000-4
1.0000000000000000-6 1.0000000000000000+0 1.0000000000000000-4
8.3140000000000000+0 2.7315000000000000+2 5.0000000000000000-1
0.0000000000000000+0 5.6705100000000000-8 1.4387690000000000-2
2.9979000000000000+8 1.0000000000000000+30
0.0000000000000000+0 0.0000000000000000+0 1.0000000000000000+2
0.0000000000000000+0 1.0000000000000000+0-1.0000000000000000+0
1.0000000000000000+6
0.0000000000000000+0 0.0000000000000000+0 1.256637061000000-6 8.85418781700000-
12 1.2000000000000000+2
steady state

```

```

continue
$....end of loadcase lcase1
$.....
$(repeat the previous 31 lines x19)

```

H. Appendix H. for Chapter III: Example Mountain 1 Layer Mechanical dat file

Example: For a 200 km wide mountain with a 600 m initial height and no ocean buoyancy

```

title          job1
$....MARC input file produced by Marc Mentat 2010.2.0 (64bit)
$.....
$....input file using extended precision
extended
$.....
sizing          0  4000  4141  284
alloc          25
elements       10
version        11
table          0  0  2  1  1  0  0  1
processor       1  1  1  0
$no list
constant d
assumed st
large stra      1  0
follow for      1  0  0
creep           0  0  0  0
all points
no echo         1  2  3
setname         41
end
$.....
solver
  8  0  0  0  0  0  0  0  0  0  0  0  0  0  0  0
0
optimize       11
connectivity
  0  0  1
  1 10  5 304 305 106
  2 10 304 306 307 305
$(deleted remaining connectivity array)
coordinates
  3 4141  0  1

```

1-2.5000000000000000+5 0.0000000000000000+0 0.0000000000000000+0
2 6.0000000000000000+2 0.0000000000000000+0 0.0000000000000000+0

\$(deleted remaining coordinates array)

```

define      element      set      icond1_elements
  1      to      4000
define      node      set      apply1_nodes
  1      4      7      8      9      10      11      12      13      14      15      16
17 c
  18      19      20      21      22      23      24      25      26      27      28
29      30 c
  31      32      33      34      35      36      37      38      39      40      41
42      43 c
  44      45      46      47      48      49      50      51      52      53      54
55      56 c
  57      58      59      60      61      62      63      64      65      66      67
68      69 c
  70      71      72      73      74      75      76      77      78      79      80
81      82 c
  83      84      85      86      87      88      89      90      91      92      93
94      95 c
  96      97      98      99      100      101      102      103      104      105
define      node      set      apply2_nodes
  1      2      3      4      5      6      304      306      308      310      312
314      316 c
  318      320      322      324      326      328      330      332      334      336
338      340      2204 c
  2205      2206      2207      2208      2209      2210      2211      2212      2213
2214      2215      2216      2217 c
  2218      2219      2220      2221      2222      2223      2225      2227      2229
2231      2233      2235      2237 c
  2239      2241      2243      2245      2247      2249      2251      2253      2255
2257      2259      4123      4124 c
  4125      4126      4127      4128      4129      4130      4131      4132      4133
4134      4135      4136      4137 c
  4138      4139      4140      4141
define      element      set      apply3_elements
  1      to      4000
isotropic

1elastic      0      0      0      0crust

```



```

7.827000000000000+9 4.999900000000000-1 9.500000000000000+2
0.000000000000000+0 0.000000000000000+0 0.000000000000000+0
0.000000000000000+0 0.000000000000000+0
    0    0    0    0    0    0    0    0
    1      to    2000
creep      data
    0    0    0    0 0.000000000000000000000000000000000+0
0.000000000000000000000000000000000+0 0.000000000000000000000000000000000+0    0    1    0
    0    0    0    0    0
isotropic

    2elastic                                0    0    0    0ocean
7.827000000000000+9 4.999900000000000-1 9.500000000000000+2
0.000000000000000+0 0.000000000000000+0 0.000000000000000+0
0.000000000000000+0 0.000000000000000+0
    0    0    0    0    0    0    0    0
    2001      to    4000
creep      data
    0    0    0    0 0.000000000000000000000000000000000+0
0.000000000000000000000000000000000+0 0.000000000000000000000000000000000+0    0    2    0
    0    0    0    0    0
geometry

0.000000000000000+0 1.000000000000000+0 0.000000000000000+0
0.000000000000000+0 0.000000000000000+0 0.000000000000000+0
0.000000000000000+0
    1      to    4000
fixed disp

    1    0    0    0    1    0apply1
0.000000000000000+0 0.000000000000000+0
    0    0
    1    2
    2
apply1_nodes
    1    0    0    0    1    0apply2
0.000000000000000+0
    0
    2
    2
apply2_nodes
dist loads

```

1 0 0 0 0 0 apply3
-1.3520000000000000+0 0.0000000000000000+0

0 0
0 102
1

apply3_elements
initial state

1 3 1 0 0 0 icond1
loadcase job1

4
icond1
apply1
apply2
apply3
no print
udump

post
10 16 17 0 0 19 20 0 1111111 0 0 0 0
0 0 0
18 0
17 0
18 0
311 0
127 0
411 0
9 0
8 0
-1 0 differential stress
-2 0 Viscosity

parameters
1.0000000000000000+0 1.0000000000000000+9 1.0000000000000000+2
1.0000000000000000+6 2.5000000000000000-1 5.0000000000000000-1
1.5000000000000000+0-5.0000000000000000-1
8.6250000000000000+0 2.0000000000000000+1 1.0000000000000000-4
1.0000000000000000-6 1.0000000000000000+0 1.0000000000000000-4
8.3140000000000000+0 2.7315000000000000+2 5.0000000000000000-1
0.0000000000000000+0 5.6705100000000000-8 1.4387690000000000-2
2.9979000000000000+8 1.0000000000000000+30
0.0000000000000000+0 0.0000000000000000+0 1.0000000000000000+2
0.0000000000000000+0 1.0000000000000000+0-2.0000000000000000+0
1.0000000000000000+6

```

0.0000000000000000+0 0.0000000000000000+0 1.256637061000000-6 8.85418781700000-
12 1.2000000000000000+2
end option
$.....
$....start of loadcase lcase1
title          lcase1
loadcase       lcase1
      3
apply1
apply2
apply3
control
  99999      10      0      0      0      1      0      0      1      0      1      0
1.0000000000000000-1 0.0000000000000000+0 0.0000000000000000+0
0.0000000000000000+0 0.0000000000000000+0 0.0000000000000000+0
0.0000000000000000+0 0.0000000000000000+0
parameters
1.0000000000000000+0 1.0000000000000000+9 1.0000000000000000+2
1.0000000000000000+6 2.5000000000000000-1 5.0000000000000000-1
1.5000000000000000+0-5.0000000000000000-1
8.6250000000000000+0 2.0000000000000000+1 1.0000000000000000-4
1.0000000000000000-6 1.0000000000000000+0 1.0000000000000000-4
8.3140000000000000+0 2.7315000000000000+2 5.0000000000000000-1
0.0000000000000000+0 5.6705100000000000-8 1.4387690000000000-2
2.9979000000000000+8 1.0000000000000000+30
0.0000000000000000+0 0.0000000000000000+0 1.0000000000000000+2
0.0000000000000000+0 1.0000000000000000+0-1.0000000000000000+0
1.0000000000000000+6
0.0000000000000000+0 0.0000000000000000+0 1.256637061000000-6 8.85418781700000-
12 1.2000000000000000+2
continue
$....end of loadcase lcase1
$.....
$....start of loadcase lcase1
title          lcase1
loadcase       lcase1
      3
apply1
apply2
apply3
control
  999999      10      0      0      0      1      0      0      1      0      1      0

```

```

1.0000000000000000-1 0.0000000000000000+0 0.0000000000000000+0
0.0000000000000000+0 0.0000000000000000+0 0.0000000000000000+0
0.0000000000000000+0 0.0000000000000000+0
parameters
1.0000000000000000+0 1.0000000000000000+9 1.0000000000000000+2
1.0000000000000000+6 2.5000000000000000-1 5.0000000000000000-1
1.5000000000000000+0-5.0000000000000000-1
8.6250000000000000+0 2.0000000000000000+1 1.0000000000000000-4
1.0000000000000000-6 1.0000000000000000+0 1.0000000000000000-4
8.3140000000000000+0 2.7315000000000000+2 5.0000000000000000-1
0.0000000000000000+0 5.6705100000000000-8 1.4387690000000000-2
2.9979000000000000+8 1.0000000000000000+30
0.0000000000000000+0 0.0000000000000000+0 1.0000000000000000+2
0.0000000000000000+0 1.0000000000000000+0-1.0000000000000000+0
1.0000000000000000+6
0.0000000000000000+0 0.0000000000000000+0 1.256637061000000-6 8.85418781700000-
12 1.2000000000000000+2
creep increment
0.0000000000000000+0
continue
$....end of loadcase lcase1
$.....
$(repeat the last 31 lines, x19)

```

```

loadcase      lcase1
      3
apply1
apply2
apply3
control
999999      10      0      0      0      1      0      0      1      0      1      0
1.0000000000000000-1 0.0000000000000000+0 0.0000000000000000+0
0.0000000000000000+0 0.0000000000000000+0 0.0000000000000000+0
0.0000000000000000+0 0.0000000000000000+0
parameters
1.0000000000000000+0 1.0000000000000000+9 1.0000000000000000+2
1.0000000000000000+6 2.5000000000000000-1 5.0000000000000000-1
1.5000000000000000+0-5.0000000000000000-1
8.6250000000000000+0 2.0000000000000000+1 1.0000000000000000-4
1.0000000000000000-6 1.0000000000000000+0 1.0000000000000000-4
8.3140000000000000+0 2.7315000000000000+2 5.0000000000000000-1
0.0000000000000000+0 5.6705100000000000-8 1.4387690000000000-2
2.9979000000000000+8 1.0000000000000000+30

```

```

0.0000000000000000+0 0.0000000000000000+0 1.0000000000000000+2
0.0000000000000000+0 1.0000000000000000+0-1.0000000000000000+0
1.0000000000000000+6
0.0000000000000000+0 0.0000000000000000+0 1.256637061000000-6 8.85418781700000-
12 1.2000000000000000+2
post increment
11111111,
creep increment
0.0000000000000000000000000000+0
continue
loadcase      lcase1
      3
apply1
apply2
apply3
control
  999999    10    0    0    0    1    0    0    1    0    1    0
1.0000000000000000-1 0.0000000000000000+0 0.0000000000000000+0
0.0000000000000000+0 0.0000000000000000+0 0.0000000000000000+0
0.0000000000000000+0 0.0000000000000000+0
parameters
1.0000000000000000+0 1.0000000000000000+9 1.0000000000000000+2
1.0000000000000000+6 2.5000000000000000-1 5.0000000000000000-1
1.5000000000000000+0-5.0000000000000000-1
8.6250000000000000+0 2.0000000000000000+1 1.0000000000000000-4
1.0000000000000000-6 1.0000000000000000+0 1.0000000000000000-4
8.3140000000000000+0 2.7315000000000000+2 5.0000000000000000-1
0.0000000000000000+0 5.6705100000000000-8 1.4387690000000000-2
2.9979000000000000+8 1.0000000000000000+30
0.0000000000000000+0 0.0000000000000000+0 1.0000000000000000+2
0.0000000000000000+0 1.0000000000000000+0-1.0000000000000000+0
1.0000000000000000+6
0.0000000000000000+0 0.0000000000000000+0 1.256637061000000-6 8.85418781700000-
12 1.2000000000000000+2
auto creep
3.1557600000000000000000000000+9 3.15576000000000000000000000+10 999999 40
0 0 0.0000000000000000+0
5.0000000000000000-1 1.0000000000000000-1 5.0000000000000001-2 0 0
continue
$(repeat the last 29 lines, editing the auto creep times to desired output times)

```

I. Appendix I. for Chapter III: Example Mountain 2 Layer Thermal dat file

Example: for a 350 km wide mountain with 600 m initial height, and two layers (with buoyancy)

```

title      job1
$....MARC input file produced by Marc Mentat 2010.2.0 (64bit)
$.....
$....input file using extended precision
extended
$.....
sizing      0  4500  4646  202
alloc      25
elements    40
version     11
table       0  0  2  1  1  0  0  1
processor    1  1  1  0
$no list
heat        0  0  1  0  1  1
thermal
all points
no echo     1  2  3
setname     27
end
$.....
solver
  8  0  0  0  0  0  0  0  0  0  0  0  0  0  0
0
optimize    11
connectivity
  0  0  1
  1  40  104  304  305  105
  2  40  304  306  307  305
$(deleted remaining connectivity array)
coordinates
  3  4646  0  1
  1-4.3750000000000001+5 0.0000000000000000+0 0.0000000000000000+0
  2 6.0000000000000000+2 0.0000000000000000+0 0.0000000000000000+0
$(deleted remaining coordinates array)

define      node      set      apply1_nodes
  2  3  205  206  207  208  209  210  211  212
213  214  215 c

```

	216	217	218	219	220	221	222	223	224	225
226	227	228	c							
	229	230	231	232	233	234	235	236	237	238
239	240	241	c							
	242	243	244	245	246	247	248	249	250	251
252	253	254	c							
	255	256	257	258	259	260	261	262	263	264
265	266	267	c							
	268	269	270	271	272	273	274	275	276	277
278	279	280	c							
	281	282	283	284	285	286	287	288	289	290
291	292	293	c							
	294	295	296	297	298	299	300	301	302	303
define		node		set		apply2_nodes				
	104	to	204							
define		edgmt		set		apply3_edges				
	1501:3		1531:3		1561:3		1591:3		1621:3	1651:3
1681:3		1711:3	c							
	1741:3		1771:3		1801:3		1831:3		1861:3	1891:3
1921:3		1951:3	c							
	1981:3		2011:3		2041:3		2071:3		2101:3	2131:3
2161:3		2191:3	c							
	2221:3		2251:3		2281:3		2311:3		2341:3	2371:3
2401:3		2431:3	c							
	2461:3		2491:3		2521:3		2551:3		2581:3	2611:3
2641:3		2671:3	c							
	2701:3		2731:3		2761:3		2791:3		2821:3	2851:3
2881:3		2911:3	c							
	2941:3		2971:3		3001:3		3031:3		3061:3	3091:3
3121:3		3151:3	c							
	3181:3		3211:3		3241:3		3271:3		3301:3	3331:3
3361:3		3391:3	c							
	3421:3		3451:3		3481:3		3511:3		3541:3	3571:3
3601:3		3631:3	c							
	3661:3		3691:3		3721:3		3751:3		3781:3	3811:3
3841:3		3871:3	c							
	3901:3		3931:3		3961:3		3991:3		4021:3	4051:3
4081:3		4111:3	c							
	4141:3		4171:3		4201:3		4231:3		4261:3	4291:3
4321:3		4351:3	c							
	4381:3		4411:3		4441:3		4471:3			
define		node		set		icond1_nodes				
	1	to	4646							

define	edgemt	set	apply4_edges				
1:0	2:0	3:0	4:0	5:0	6:0	7:0	8:0
c	9:0	10:0	11:0	12:0	13:0	14:0	15:0
1486:2 c	1487:2	1488:2	1489:2	1490:2	1491:2	1492:2	
1493:2	1494:2 c						
	1495:2	1496:2	1497:2	1498:2	1499:2	1500:2	
1501:0	1502:0 c						
	1503:0	1504:0	1505:0	1506:0	1507:0	1508:0	
1509:0	1510:0 c						
	1511:0	1512:0	1513:0	1514:0	1515:0	1516:0	
1517:0	1518:0 c						
	1519:0	1520:0	1521:0	1522:0	1523:0	1524:0	
1525:0	1526:0 c						
	1527:0	1528:0	1529:0	1530:0	4471:2	4472:2	
4473:2	4474:2 c						
	4475:2	4476:2	4477:2	4478:2	4479:2	4480:2	
4481:2	4482:2 c						
	4483:2	4484:2	4485:2	4486:2	4487:2	4488:2	
4489:2	4490:2 c						
	4491:2	4492:2	4493:2	4494:2	4495:2	4496:2	
4497:2	4498:2 c						
	4499:2	4500:2					
isotropic							
1	0	0	0	0	0	0	0
9.3000000000000001	+0	1.0000000000000000	+3	9.5000000000000000	+2		
0.0000000000000000	+0	0.0000000000000000	+0	0.0000000000000000	+0		
0.0000000000000000	+0						
0	0	0	0	0	0	0	
1	to	1500					
isotropic							
2	0	0	0	0	0	0	0
9.3000000000000001	+0	1.0000000000000000	+3	1.0500000000000000	+3		
0.0000000000000000	+0	0.0000000000000000	+0	0.0000000000000000	+0		
0.0000000000000000	+0						
0	0	0	0	0	0	0	
1501	to	4500					
geometry							

0.0000000000000000+0 0.0000000000000000+0 0.0000000000000000+0
 1.0000000000000000+0 0.0000000000000000+0 0.0000000000000000+0
 0.0000000000000000+0

1 to 4500							
temperature effects				data			
22	22	0	0	0	0	1	0
9.3000000000000000+0					0.0000000000000000+2		
9.3000000000000000+0					0.7000000000000000+2		
8.1375000000000000+0					0.8000000000000000+2		
7.2333000000000000+0					0.9000000000000000+2		
6.5100000000000000+0					1.0000000000000000+2		
5.918181818181818+0					1.1000000000000000+2		
5.4250000000000000+0					1.2000000000000000+2		
5.0077000000000000+0					1.3000000000000000+2		
4.6500000000000000+0					1.4000000000000000+2		
4.3400000000000000+0					1.5000000000000000+2		
4.0687500000000000+0					1.6000000000000000+2		
3.8294100000000000+0					1.7000000000000000+2		
3.616666666666666+0					1.8000000000000000+2		
3.4263000000000000+0					1.9000000000000000+2		
3.2550000000000000+0					2.0000000000000000+2		
3.1000000000000000+0					2.1000000000000000+2		
2.9591000000000000+0					2.2000000000000000+2		
2.8300000000000000+0					2.3000000000000000+2		
2.7125000000000000+0					2.4000000000000000+2		
2.6040000000000000+0					2.5000000000000000+2		
2.5040000000000000+0					2.6000000000000000+2		
2.5040000000000000+0					2.6000000000000000+4		
6.6320000000000000+3					0.0000000000000000+2		
6.6320000000000000+3					0.7000000000000000+2		
6.6320000000000000+3					0.8000000000000000+2		
6.6320000000000000+3					0.9000000000000000+2		
5.9680000000000000+3					1.0000000000000000+2		
5.4260000000000000+3					1.1000000000000000+2		
4.9740000000000000+3					1.2000000000000000+2		
4.5910000000000000+3					1.3000000000000000+2		
4.2630000000000000+3					1.4000000000000000+2		
3.9790000000000000+3					1.5000000000000000+2		
3.7300000000000000+3					1.6000000000000000+2		
3.5110000000000000+3					1.7000000000000000+2		
3.3160000000000000+3					1.8000000000000000+2		
3.1410000000000000+3					1.9000000000000000+2		
2.9840000000000000+3					2.0000000000000000+2		

2.842000000000000+3	2.100000000000000+2
2.713000000000000+3	2.200000000000000+2
2.595000000000000+3	2.300000000000000+2
2.487000000000000+3	2.400000000000000+2
2.387000000000000+3	2.500000000000000+2
2.296000000000000+3	2.600000000000000+2
2.296000000000000+3	2.600000000000000+4

initial temp

1	0	0	0	0	0	icond1
9.000000000000000+1						
0						
2						

icond1_nodes
fixed temperature

1	0	0	0	0	0	0	apply1
9.400000000000000+1							
0							
1							
2							

apply1_nodes

1	0	0	0	0	0	0	apply2
1.760000000000000+2							
0							
1							
2							

apply2_nodes
dist fluxes

1	0	0	0	0	0	0	apply3
4.000000000000000-3							
0							
0						10	
13							

apply3_edges

1	0	0	0	0	0	0	apply4
0.000000000000000+0							
0							
0						10	
13							

apply4_edges
loadcase job1

```

5
icond1
apply1
apply2
apply3
apply4
no print
post
    1    16    17    0    0    19    20    0    1    0    0    0    0    0
0    0
    180    0
parameters
1.0000000000000000+0 1.0000000000000000+9 1.0000000000000000+2
1.0000000000000000+6 2.5000000000000000-1 5.0000000000000000-1
1.5000000000000000+0-5.0000000000000000-1
8.6250000000000000+0 2.0000000000000000+1 1.0000000000000000-4
1.0000000000000000-6 1.0000000000000000+0 1.0000000000000000-4
8.3140000000000000+0 2.7315000000000000+2 5.0000000000000000-1
0.0000000000000000+0 5.6705100000000000-8 1.4387690000000000-2
2.9979000000000000+8 1.0000000000000000+30
0.0000000000000000+0 0.0000000000000000+0 1.0000000000000000+2
0.0000000000000000+0 1.0000000000000000+0-2.0000000000000000+0
1.0000000000000000+6
0.0000000000000000+0 0.0000000000000000+0 1.256637061000000-6 8.85418781700000-
12 1.2000000000000000+2
end option
$.....
$....start of loadcase lcase1
title          lcase1
loadcase       lcase1
    4
apply1
apply2
apply3
apply4
control
    99999    10    0    0    0    0    0    0    1    0    0    0
2.0000000000000000+1 1.0000000000000000+2 0.0000000000000000+0
1.0000000000000000+2 1.0000000000000000-1 1.0000000000000000-1 1.0000000000000000-
1 1.0000000000000000+30
parameters

```

```

1.0000000000000000+0 1.0000000000000000+9 1.0000000000000000+2
1.0000000000000000+6 2.5000000000000000-1 5.0000000000000000-1
1.5000000000000000+0-5.0000000000000000-1
8.6250000000000000+0 2.0000000000000000+1 1.0000000000000000-4
1.0000000000000000-6 1.0000000000000000+0 1.0000000000000000-4
8.3140000000000000+0 2.7315000000000000+2 5.0000000000000000-1
0.0000000000000000+0 5.6705100000000000-8 1.4387690000000000-2
2.9979000000000000+8 1.0000000000000000+30
0.0000000000000000+0 0.0000000000000000+0 1.0000000000000000+2
0.0000000000000000+0 1.0000000000000000+0-1.0000000000000000+0
1.0000000000000000+6
0.0000000000000000+0 0.0000000000000000+0 1.256637061000000-6 8.85418781700000-
12 1.2000000000000000+2
steady state
continue
$(repeat the previous 29 lines x19)

```

J. Appendix J. for Chapter III: Example Mountain 2 Layer Mechanical dat file

Example: for a 350 km wide mountain with 600 m initial height, and two layers (with buoyancy)

```

title          job1
$....MARC input file produced by Marc Mentat 2010.2.0 (64bit)
$.....
$....input file using extended precision
extended
$.....
sizing          0   4500   4646   294
alloc          25
elements        10
version         11
table           0   0   2   1   1   0   0   1
processor        1   1   1   0
$no list
constant d
assumed st
large stra       1   0
follow for       1   0   0
creep           0   0   0   0
all points
no echo          1   2   3
setname         46

```

```

end
$.....
solver
    8    0    0    0    0    0    0    0    0    0    0    0    0    0    0
0
optimize        11
connectivity
    0    0    1
    1    10   104   304   305   105
    2    10   304   306   307   305
(deleted remaining connectivity array)

coordinates
    3  4646    0    1
    1-4.3750000000000001+5 0.0000000000000000+0 0.0000000000000000+0
    2 6.0000000000000000+2 0.0000000000000000+0 0.0000000000000000+0
(deleted remaining coordinates array)
define        node        set        apply1_nodes
    1         4         5         6         7         8         9        10        11        12        13        14
15 c
    16        17        18        19        20        21        22        23        24        25        26
27   28 c
    29        30        31        32        33        34        35        36        37        38        39
40   41 c
    42        43        44        45        46        47        48        49        50        51        52
53   54 c
    55        56        57        58        59        60        61        62        63        64        65
66   67 c
    68        69        70        71        72        73        74        75        76        77        78
79   80 c
    81        82        83        84        85        86        87        88        89        90        91
92   93 c
    94        95        96        97        98        99       100       101       102       103
define        node        set        apply2_nodes
    1         2         3         4       104       204       304       306       308       310       312
314   316 c
    318       320       322       324       326       328       330       1704       1705       1706
1707   1708   1709 c
    1710      1711      1712      1713      1714      1715      1716      1717      1718
1720   1722   1724   1726 c
    1728      1730      1732      1734      1736      1738      1740      1742      1744
1746   1748   1750   1752 c

```

```

1754 1756 1758 1760 1762 1764 1766 1768 1770
1772 1774 4618 4619 c
4620 4621 4622 4623 4624 4625 4626 4627 4628
4629 4630 4631 4632 c
4633 4634 4635 4636 4637 4638 4639 4640 4641
4642 4643 4644 4645 c
4646
define element set apply3_elements
1 to 4500
define element set icond1_elements
1 to 4500
isotropic

1elastic 0 0 0 0crust
7.827000000000000+9 4.999900000000000-1 9.500000000000000+2
0.000000000000000+0 0.000000000000000+0 0.000000000000000+0
0.000000000000000+0 0.000000000000000+0
0 0 0 0 0 0 0 0
1 to 1500
creep data
0 0 0 0 0.000000000000000000000000+0
0.000000000000000000000000+0 0.000000000000000000000000+0 0 1 0
0 0 0 0 0
isotropic

2elastic 0 0 0 0ocean
7.827000000000000+9 4.999000000000000-1 1.050000000000000+3
0.000000000000000+0 0.000000000000000+0 0.000000000000000+0
0.000000000000000+0 0.000000000000000+0
0 0 0 0 0 0 0 0
1501 to 4500
creep data
0 0 0 0 0.000000000000000000000000+0
0.000000000000000000000000+0 0.000000000000000000000000+0 0 2 0
0 0 0 0 0
geometry

0.000000000000000+0 1.000000000000000+0 0.000000000000000+0
0.000000000000000+0 0.000000000000000+0 0.000000000000000+0
0.000000000000000+0
1 to 4500
fixed disp

```

```

1 0 0 0 1 0apply1
0.0000000000000000+0 0.0000000000000000+0

```

```

0 0
1 2
2

```

apply1_nodes

```

1 0 0 0 1 0apply2
0.0000000000000000+0

```

```

0
2
2

```

apply2_nodes

dist loads

```

1 0 0 0 0 0apply3
-1.3520000000000000+0 0.0000000000000000+0

```

```

0 0
0 102
1

```

apply3_elements

initial state

```

1 3 1 0 0 0icond1
loadcase job1

```

```

4

```

icond1

apply1

apply2

apply3

no print

udump

post

```

10 16 17 0 0 19 20 0 1111111 0 0 0 0
0 0 0
18 0
17 0
18 0
311 0
127 0
411 0
9 0
8 0

```

```

-1      0differential stress
-2      0Viscosity
parameters
1.0000000000000000+0 1.0000000000000000+9 1.0000000000000000+2
1.0000000000000000+6 2.5000000000000000-1 5.0000000000000000-1
1.5000000000000000+0-5.0000000000000000-1
8.6250000000000000+0 2.0000000000000000+1 1.0000000000000000-4
1.0000000000000000-6 1.0000000000000000+0 1.0000000000000000-4
8.3140000000000000+0 2.7315000000000000+2 5.0000000000000000-1
0.0000000000000000+0 5.6705100000000000-8 1.4387690000000000-2
2.9979000000000000+8 1.0000000000000000+30
0.0000000000000000+0 0.0000000000000000+0 1.0000000000000000+2
0.0000000000000000+0 1.0000000000000000+0-2.0000000000000000+0
1.0000000000000000+6
0.0000000000000000+0 0.0000000000000000+0 1.256637061000000-6 8.85418781700000-
12 1.2000000000000000+2
end option
$.....
$....start of loadcase lcase1
title      lcase1
loadcase    lcase1
      3
apply1
apply2
apply3
control
99999      10      0      0      0      1      0      0      1      0      1      0
1.0000000000000000-1 0.0000000000000000+0 0.0000000000000000+0
0.0000000000000000+0 0.0000000000000000+0 0.0000000000000000+0
0.0000000000000000+0 0.0000000000000000+0
parameters
1.0000000000000000+0 1.0000000000000000+9 1.0000000000000000+2
1.0000000000000000+6 2.5000000000000000-1 5.0000000000000000-1
1.5000000000000000+0-5.0000000000000000-1
8.6250000000000000+0 2.0000000000000000+1 1.0000000000000000-4
1.0000000000000000-6 1.0000000000000000+0 1.0000000000000000-4
8.3140000000000000+0 2.7315000000000000+2 5.0000000000000000-1
0.0000000000000000+0 5.6705100000000000-8 1.4387690000000000-2
2.9979000000000000+8 1.0000000000000000+30
0.0000000000000000+0 0.0000000000000000+0 1.0000000000000000+2
0.0000000000000000+0 1.0000000000000000+0-1.0000000000000000+0
1.0000000000000000+6

```



```

0.0000000000000000+0 0.0000000000000000+0 1.256637061000000-6 8.85418781700000-
12 1.2000000000000000+2
continue
$....end of loadcase lcase1
$.....
$....start of loadcase lcase1
title          lcase1
loadcase       lcase1
      3
apply1
apply2
apply3
control
      999999      10      0      0      0      1      0      0      1      0      1      0
1.0000000000000000-1 0.0000000000000000+0 0.0000000000000000+0
0.0000000000000000+0 0.0000000000000000+0 0.0000000000000000+0
0.0000000000000000+0 0.0000000000000000+0
parameters
1.0000000000000000+0 1.0000000000000000+9 1.0000000000000000+2
1.0000000000000000+6 2.5000000000000000-1 5.0000000000000000-1
1.5000000000000000+0-5.0000000000000000-1
8.6250000000000000+0 2.0000000000000000+1 1.0000000000000000-4
1.0000000000000000-6 1.0000000000000000+0 1.0000000000000000-4
8.3140000000000000+0 2.7315000000000000+2 5.0000000000000000-1
0.0000000000000000+0 5.6705100000000000-8 1.4387690000000000-2
2.9979000000000000+8 1.0000000000000000+30
0.0000000000000000+0 0.0000000000000000+0 1.0000000000000000+2
0.0000000000000000+0 1.0000000000000000+0-1.0000000000000000+0
1.0000000000000000+6
0.0000000000000000+0 0.0000000000000000+0 1.256637061000000-6 8.85418781700000-
12 1.2000000000000000+2
creep increment
0.0000000000000000000000000000+0
$(repeat the last 29 lines, x19)

loadcase       lcase1
      3
apply1
apply2
apply3
control
      999999      10      0      0      0      1      0      0      1      0      1      0

```

```

1.0000000000000000-1 0.0000000000000000+0 0.0000000000000000+0
0.0000000000000000+0 0.0000000000000000+0 0.0000000000000000+0
0.0000000000000000+0 0.0000000000000000+0
parameters
1.0000000000000000+0 1.0000000000000000+9 1.0000000000000000+2
1.0000000000000000+6 2.5000000000000000-1 5.0000000000000000-1
1.5000000000000000+0-5.0000000000000000-1
8.6250000000000000+0 2.0000000000000000+1 1.0000000000000000-4
1.0000000000000000-6 1.0000000000000000+0 1.0000000000000000-4
8.3140000000000000+0 2.7315000000000000+2 5.0000000000000000-1
0.0000000000000000+0 5.6705100000000000-8 1.4387690000000000-2
2.9979000000000000+8 1.0000000000000000+30
0.0000000000000000+0 0.0000000000000000+0 1.0000000000000000+2
0.0000000000000000+0 1.0000000000000000+0-1.0000000000000000+0
1.0000000000000000+6
0.0000000000000000+0 0.0000000000000000+0 1.256637061000000-6 8.85418781700000-
12 1.2000000000000000+2
auto creep
3.155760000000000000000000000000+10 3.1557600000000000000000000000+14 999999 40
0 0 0.0000000000000000+0
5.0000000000000000-1 1.0000000000000000-1 5.0000000000000001-2 0 0
continue
$(repeat previous 29 lines, changing auto creep to output desired times)

```

K. Appendix K. for Chapter III: Example Mountain Subroutine File for a 1 Layer Methane Clathrate Hydrate:

This subroutine is written in Fortran by Andrew Dombard and edited by Lauren Schurmeier. Lines starting with C are not read.

Example: for an ice shell that is composed of methane clathrate hydrate.

```

C
      SUBROUTINE CRPLAW(EQCP,EQCPNC,STR,CRPE,T,DT,TIMINC,CPTIM,M,NN,KC,
*          MATS,NDI,NSHEAR)
C
      IMPLICIT REAL*8 (A-H,O-Z)
C
      DIMENSION T(3),DT(1),STR(1),CRPE(1)
C
      GS = 1.d-3
      RT = 8.31451d0*DT(1)
      dis = (2.24d8)*((T(1)/1.0d+6)**(2.2d0))*dexp(-90.d3/RT)
C

```

```

rate = dis
viscmin = 1.d18
if (cptim.gt.3.15576d11) viscmin = 1.d18
if (cptim.gt.3.15576d12) viscmin = 1.d19
if (cptim.gt.3.15576d13) viscmin = 1.d20
if (cptim.gt.3.15576d14) viscmin = 1.d21
if (cptim.gt.3.15576d15) viscmin = 1.d22
eta = T(1)/(3.d0*rate)
if (eta.lt.viscmin) rate = T(1)/(3.d0*viscmin)
EQCPNC = TIMINC*rate
C
RETURN
END
C
C-----
C
SUBROUTINE UINSTR(S,NDI,NSHEAR,NI,NNI,KCI,XINTP,NCRDI,INC,TIME,TIMEINC)
C
IMPLICIT REAL*8 (A-H,O-Z)
C
DIMENSION S(1),XINTP(NCRD),NI(2)
DIMENSION CCNODE(12)
C
parameter(GP = 0.577350269189626d0)
C
include '/opt/msc/marc2010.2/common/lass'
include '/opt/msc/marc2010.2/common/dimen'
include '/opt/msc/marc2010.2/common/space'
include '/opt/msc/marc2010.2/common/blnk'
include '/opt/msc/marc2010.2/common/array2'
include '/opt/msc/marc2010.2/common/spacevec'
include '/opt/msc/marc2010.2/common/strvar'
C
if (nnl.eq.1) then
eta1 = -1.d0*GP
eta2 = -1.d0*GP
endif
if (nnl.eq.2) then
eta1 = 1.d0*GP
eta2 = -1.d0*GP
endif
if (nnl.eq.3) then
eta1 = -1.d0*GP

```

```

    eta2 = 1.d0*GP
endif
if (nnl.eq.4) then
    eta1 = 1.d0*GP
    eta2 = 1.d0*GP
endif
C    Quadralateral Elements
    x = 0.d0
    y = 0.d0
    JRDPRE = 0
C    CALL VECFTC(CCNODE,VARS(IXORD),NCRDMX,NCRD,lm(1),JRDPRE,2,1)
    CALL VECFTC(CCNODE,XORD_D,NCRDMX,NCRD,lm(1),JRDPRE,2,1)
    x = x + (1.d0 - eta1)*(1.d0 - eta2)*ccnode(1)/4.d0
    y = y + (1.d0 - eta1)*(1.d0 - eta2)*ccnode(2)/4.d0
    JRDPRE = 0
C    CALL VECFTC(CCNODE,VARS(IXORD),NCRDMX,NCRD,lm(2),JRDPRE,2,1)
    CALL VECFTC(CCNODE,XORD_D,NCRDMX,NCRD,lm(2),JRDPRE,2,1)
    x = x + (1.d0 + eta1)*(1.d0 - eta2)*ccnode(1)/4.d0
    y = y + (1.d0 + eta1)*(1.d0 - eta2)*ccnode(2)/4.d0
    JRDPRE = 0
C    CALL VECFTC(CCNODE,VARS(IXORD),NCRDMX,NCRD,lm(3),JRDPRE,2,1)
    CALL VECFTC(CCNODE,XORD_D,NCRDMX,NCRD,lm(3),JRDPRE,2,1)
    x = x + (1.d0 + eta1)*(1.d0 + eta2)*ccnode(1)/4.d0
    y = y + (1.d0 + eta1)*(1.d0 + eta2)*ccnode(2)/4.d0
    JRDPRE = 0
C    CALL VECFTC(CCNODE,VARS(IXORD),NCRDMX,NCRD,lm(4),JRDPRE,2,1)
    CALL VECFTC(CCNODE,XORD_D,NCRDMX,NCRD,lm(4),JRDPRE,2,1)
    x = x + (1.d0 - eta1)*(1.d0 + eta2)*ccnode(1)/4.d0
    y = y + (1.d0 - eta1)*(1.d0 + eta2)*ccnode(2)/4.d0
C
C Stress Profile Parameters:
    rho = 950.d0
    g = 1.352d0
C
    S(1) = rho*g*y
    S(2) = rho*g*y
    S(3) = rho*g*y
C
    RETURN
    END
C
C-----
C

```

```

subroutine impd(n,dd,td,xord,f,v,a,nd,ncrd)
C
IMPLICIT REAL*8 (A-H,O-Z)
C
dimension dd(nd),td(nd),xord(ncrd),f(nd),v(nd),a(nd),n(2)
C
include '/opt/msc/marc2010.2/common/creeps'
include '/opt/msc/marc2010.2/common/concom'
C
open(10,file='test.txt',status='unknown')
C
d0 = 600.d0
if (n(1).eq.2) d1 = td(1)
if (n(1).eq.3) then
    d2 = td(1)
    dc = d0 + d1 - d2
C    if (inc.eq.20) de = dc
C    dn = dc/de
C    if (inc.ge.20) write(10,666)inc,cptim/3.15576d7,dc,1.d0 - dn
    if (inc.ge.20) write(10,666)inc,cptim/3.15576d7,dc
endif
C666 format(i6,e13.5,f9.2,2f9.5)
666 format(i6,e13.5,f9.2)
C
return
end
C
C-----
C
subroutine plotv(v,s,sp,etot,eplas,ecreep,t,m,nn,layer,ndi,
* nshear,jpltcd)
C SUBROUTINE PLOTV(V,S,SP,ETOT,EPLAS,ECREEP,T,M,NN,LAYER,NDI,
C * NSHEAR,JPLNCD)
C
include '/opt/msc/marc2010.2/common/implicit'
IMPLICIT REAL*8 (A-H,O-Z)
dimension s(*),etot(*),eplas(*),ecreep(*),sp(*),m(2)
C DIMENSION S(1),SP(1),ETOT(1),EPLAS(1),ECREEP(1),M(2)
C
if (jpltcd.lt.2) then
    V = S(2) - S(1)
else
    smean = (s(1) + s(2) + s(3))/3.d0

```

```

s1 = s(1) - smean
s2 = s(2) - smean
s3 = s(3) - smean
es = dsqrt((s1*s1 + s2*s2 + s3*s3)/2.d0 + s(4)*s(4))
GS = 1.d-3
RT = 8.31451d0*T
dis = (2.24d8)*((es/1.0d+6)**(2.2d0))*dexp(-90.d3/RT)
r = dis
V = dlog10(dabs(es)) - dlog10(dabs(3.d0*r))
endif
C
RETURN
END
C
C=====

```

L. Appendix L. for Chapter IV: Domed Labyrinth Measurements

Table 1: Longest diameter measurement and implied cryovolcanic intrusion depths for each feature.

Feature	Longest Diameter (km)	Implied Depth (km)	Notes
A	137	29	
B	100 +	30 +	Longest diameter may extend out of SAR swath
C	145	30	
E	155	32	
F	128	27	Shortest diameter may extend out of SAR swath
G	150	31	Shortest diameter may extend out of SAR swath
H	142 +	30 +	Longest diameter may extend out of SAR swath
I	155 +	32 +	Longest diameter may extend out of SAR swath

Table 2: Spacing between features within the same SAR swaths and implied rising layer thickness for the diapir hypothesis.

Features	Spacing (km)	Implied Thickness (km)
A - B	230	89
C - F	250	97
E - F	130	51
E - D	160	62
C - D	230	89
G - H	130	51

M. Appendix M. for Chapter IV: Lithospheric Strength Envelope Equations

S = strain rate [s^{-1}]

T = temperature (function of depth) [K]

D = grain size [m]

R = $8.31 [J \text{ mol}^{-1} \text{ K}^{-1}]$

P = pressure (function of depth)

Water Ice:

Dislocation = $[(S/(400000 * 0.4871)) * e^{(60000/(RT))}]^{0.25}$

Diffusion = $TSD^2 / [(3.02 \times 10^{-8} * e^{(-59400/RT)}) + ((\pi * 9.04 \times 10^{-10}/D) * e^{(-60000/RT)})]$

Easy Slip = $[(S/(55000000 * 0.613202)) * e^{(60000/RT)}]^{(1/2.4)}$

Grain Boundary Sliding = $[(SD^{1.4}/(0.0039 * 0.66847)) * e^{(49000/RT)}]^{(1/1.8)}$

Methane Clathrate Hydrate:

Dislocation = $[(S * e^{(90,000+(P*19)/(RT))}) / 2.24 \times 10^8]^{(1/2.2)}$

N. Appendix N. Statements about Permission to Reprint the Previously Published Chapter II

Chapter II has been published in the journal *Icarus* (part of Elsevier) volume 305 pages 314-323 as: "Crater Relaxation on Titan Aided by Low Thermal Conductivity Sand Infill", by Lauren R. Schurmeier, Andrew J. Dombard.

The copyright holder Elsevier do not require reprint permission for an academic thesis, as shown in this screenshot of the Elsevier website guide for authors.



Q SEARCH

- **Multiple, redundant or concurrent publication:** An author should not in general publish manuscripts describing essentially the same research in more than one journal or primary publication. Elsevier does not view the following uses of a work as prior publication: publication in the form of an abstract; publication as an academic thesis; publication as an electronic preprint. Information on prior publication is included within each Elsevier journal's Guide for Authors. Note: *Cell Press*, *The Lancet*, and some society-owned titles have different policies on prior publication. Information on these is available on the journal homepage.

<https://www.elsevier.com/authors/journal-authors/policies-and-ethics>

It says, "Multiple, redundant or concurrent publication: An author should not in general publish manuscripts describing essentially the same research in more than one journal or primary publication. Elsevier does not view the following uses of a work as prior publication: publication in the form of an abstract; publication as an academic thesis; publication as an electronic preprint. Information on prior publication is included within each Elsevier journal's Guide for Authors. Note: Cell Press, The Lancet, and some society-owned titles have different policies on prior publication. Information on these is available on the journal homepage.

The Elsevier website also states in their frequently asked questions:

[Can I include/use my article in my thesis/dissertation? –](#)

Yes. Authors can include their articles in full or in part in a thesis or dissertation for non-commercial purposes.

"Can I include/use my article in my thesis/dissertation? Yes. Authors can include their articles in full or in part in a thesis or dissertation for non-commercial purposes."

<https://www.elsevier.com/about/policies/copyright/permissions>

Lauren Schurmeier

Curriculum Vitae

Earth and Environmental Sciences, University of Illinois at Chicago
845 W. Taylor Street, Chicago IL, 60607

email: lschur2@uic.edu
lschurme@gmail.edu

Education

University of Illinois at Chicago

Ph.D. Earth and Environmental Sciences, 2018

Dissertation: Investigating the Evolution of Surface Features on Saturn's Moon Titan

Advisor: Andrew Dombard

Certificate in College Instruction, 2018

Graduate College, UIC

Certificate in Geospatial Analysis and Visualization, 2017

Urban Planning and Policy Department, UIC

University of California, Santa Cruz

B.S. Earth Science with a concentration in Planetary Science, 2011

Senior Thesis: The Discovery of a Rare Jupiter-Analog Candidate Planet in the Upsilon

Andromedae System

Advisor: Gregory Laughlin

Research Interests

- Using remote sensing of planetary surface processes to infer interior processes
- Planetary geomorphology, lithospheric geodynamics, astrobiology
- Planetary mission planning
- Geoscience education

Publications

L. Schurmeier and A. Dombard 2018 "Crater relaxation aided by low thermal conductivity sand on Titan" *Icarus*, 305, 314 - 323.

J. Heldmann, **L. Schurmeier**, C. Stoker, C. McKay, A. Davila, M. Marinova, M.B. Wilhelm, 2014 "Midlatitude ice-rich ground on Mars as a target in the search for evidence of life and for in situ resource utilization on human missions" *Astrobiology* 14 (2), 102 -118.

L. Schurmeier, A. Dombard, J. Radebaugh. "Investigating the Support of Titan's Large Mountain Plateaus by Airy Isostasy" *Icarus*. *In preparation*.

L. Schurmeier, A. Dombard, M. Malaska, J. Radebaugh. "An Intrusive Cryovolcanic Origin for Radial Labyrinth Terrains on Titan Implies a Water Ice-Rich Crust" *Icarus*. *In preparation*.

Abstracts

Schurmeier, L., Dombard, A., Radebaugh, J., Malaska, M., (2018) "Intrusive and Extrusive Cryovolcanism and the Composition of Titan's Icy Crust" LPSC Abstract # 2934.

Tremblay, S., Dombard, A., **Schurmeier, L.**, (2018) "Global Lacunarity of Planetary Datasets: Methodology" LPSC Abstract #2460.

Castillo, J., Dombard, A., **Schurmeier, L.**, (2018) "Ceres' Largest Craters: Age Analysis of Kerwan and Yalode" LPSC Abstract #2476.

Schurmeier, L., Dombard, A., Malaska, M., Radebaugh, J., (2017). "Are Titan's radial Labyrinth terrains surface expressions of large laccoliths?" AGU Abstract # 227212.

Malaska, M., Lopes-Gautier, R., Solomonido, A., Mitchel, K., Radebaugh, J., **Schurmeier, L.**, Le Gall, A., (2017). "Is there a Laccolith Origin for Titan's Radial Labyrinths?" AOGS Abstract

Schurmeier, L., Dombard, A., Radebaugh, J. (2016) "Titan's Isolated Mountain Plateaus: Investigating Possible Support Mechanisms and Cryovolcanic Origins" Lunar and Planetary Science Conference (LPSC) Abstract # 2197 (Talk).

Schurmeier, L. and Dombard, A. (2014). "Crater Relaxation Aided by Aeolian Infill on Titan" Titan Through Time Workshop (Talk).

Schurmeier, L. and Dombard, A. (2013). "The Effects of Low Thermal Conductivity Sand on the Relaxation of Titan's Impact Craters" LPSC Abstract # 2913.

Schurmeier, L., Heldmann, J., et al. (2013). "Midlatitude Ice-Rich Ground on Mars as a Target in the Search for Evidence of Life and for in situ Resource Utilization on Human Missions" Fall AGU Abstract # P23F-1856.

Khare, B., McKay, C., Kawai, J., Nna Mvondo, D., Jagota, S., Carter, M., **Schurmeier, L.**, Cruikshank, D., (2012). "Organic matter in the Titan lakes, and comparison with primitive Earth" COSPAR Abstract E1.11-23-12 (Talk).

Schurmeier, L., Heldmann, J., et al. (2012). "Characterization of a Mid-Latitude Ice-Rich Landing Site on Mars to Enable In Situ Habitability Studies" LPSC Abstract #1271

Heldmann, J. L., **Schurmeier, L.**, Stoker, C., McKay, C., Davila, A., Marinova, M., Karcz, J., Smith, H. (2012). "Mission Concept to Enable Science and In Situ Resource Utilization of Mid-Latitude Ice on Mars". Concepts and Approaches for Mars Exploration, Houston, Texas. LPI Contribution No. 1679, id. 411 (Talk).

Fellowships & Grants

2016 **Illinois Space Grant Consortium Graduate Fellowship:** \$10,000

2015 **Illinois Space Grant Consortium Graduate Fellowship:** \$10,000

2013 **Illinois Space Grant Consortium Graduate Fellowship:** \$10,000

2017 **Earth Educators Rendezvous Travel Grant:** \$400

2017 **UIC Liberal Arts and Sciences Travel Grant:** \$250

Research Experience

2012 - Present Titan's Radial Labyrinth Terrains - Possible Uplift Mechanisms

Map and classify mountainous Labyrinth Terrains using ArcGIS. Compare with scaling relationships of laccoliths and diapirs. Calculate the brittle-ductile transition (BDT) of Titan's ice shell in water ice and methane clathrate. Labyrinth size may be explained by a laccolith intrusion at the BDT in ice.

The Evolution and Stability of Titan's Large Mountainous Plateaus

I use the Marc-Mentat finite element package to model and compare the stability of various support mechanisms for large topographic loads in ice or methane clathrate ice shells at various basal heat flows.

Relaxation of Impact Craters on Titan

I estimated the thermal conductivity of Titan's organic-rich sand. Model viscoelastic crater relaxation aided by thermally insulating sand infill using Marc-Mentat.

2011 - 2014 Mars Icebreaker Mission Landing Site Selection

Advisors: Jennifer Heldmann & Chris McKay, NASA Ames Research Center

I developed criteria for ranking landing sites based on science objectives (evidence of ice-cemented soil) and landing dangers for the proposed Mars lander mission Icebreaker. I ranked regions of Mars using the HiRISE images in the JMARS remote sensing program and IDL. I found an optimal site.

2010 - 2012 Titan Analog Experiments: Tholin Solubility Experiments

Advisors: Bishun Khare & Chris McKay, NASA Ames Research Center

I helped design and build glass cryogenic chambers to create and analyze laboratory analogs of Titan's atmosphere, haze molecules (tholins), and methane/ethane lakes. We used GC-MS to investigate the solubility of tholins in lake analogs for use in astrobiological studies and future mission planning.

2010 - 2011 Undergraduate Senior Thesis - Exoplanets

I analyzed the UpsAnd planetary system using the Systemic Console and radial velocity data. I confirmed three candidate exoplanets and discovered a fourth. I devised a similarity statistic and found that the fourth was a rare Jupiter analog.

Undergraduate Research Mentoring

2017 - Present Sheri Tremblay, "Lacunarity spatial analysis on global planetary scales: applied to Venus and the Moon"

2017 - Present John Castillo, "Crater counting to establish the ages of large impact craters on dwarf planet Ceres"

Awards

2017 Outstanding Teaching Assistant - National Assoc. of Geoscience Teachers

2015 Department Citizenship Award - UIC Earth and Env. Sciences Dept.

2014 Outstanding Teaching Assistant Award - UIC Earth and Env. Sciences Dept.

Teaching Experience

2011 - Teaching Assistant, University of Illinois at Chicago

Present

EAES 111- Earth, Energy, and the Environment (7 semesters)

EAES 101 - Global Environmental Change (1 semester)

NATS 105 - Physical Systems in Earth and Space Science (2 semesters)

EAES 444 - Geophysics (1 semester)

EAES 470 - Environmental Geomorphology (1 semester)

Independently ran laboratory sections, improved and created new laboratory exercises, developed online pre-lab and homework assignments, graded student work, wrote exam questions, and led field trips. Helped train graduate students.

2013 - Guest Lecturer, University of Illinois at Chicago

Present

Multiple guest lectures for >130 student (EAES 111) and ~60 student (NATS 105) introductory lecture courses and < 20 student senior-level undergraduate courses (EAES 444, 470) using lectures that I developed with a focus on active learning.

2017 - Course Preparation Teaching Assistant, Chicago Geopaths Program

Present

Assisted in the preparation of a new program for high school and community college students. Its intention is to increase the number of students, especially underrepresented minority students, who choose geoscience as a major. I created the website and helped plan the field trip and course activities.

2010, 2011, 2012 Teaching Assistant, UC Santa Cruz COSMOS Summer Program (Astrophysics)

Lectured on astrophysics topics, assisted high school students during remote telescope observing, mentored students, and worked with small groups on their physics and astronomy projects for three summers.

Service

2014 - The Planetary Society - Chicago Chapter

Present

Plan and volunteer at Planetary Society space science outreach and advocacy events. Manage the social media; manage Instagram, co-manage Facebook.

--

Executive Secretary - NASA Mission Data Analysis Proposals Sci. Review Panel

--

Leveler - Science Review Panel for NASA Proposals

2016, 2017 Guest Lecturer / Volunteer Chicago Montessori School

2015 Science Fair Judge, Lincoln Park High School

2013 - 2015 The Terra Society - Earth and Environmental Science Club

Treasurer, head fund raiser, lunch planner and event organizer.

Workshops and Professional Development

2018 NASA Planetary Science Summer Seminar - mission - planning course

2017 AGU - Broadening Participation of Underrepresented Groups in the Geosciences

2017 Earth Educators Rendezvous Workshop - Preparing for an Academic Career Workshop; Flipped Classroom / Active Learning Workshop

2017, 2014 **Titan Through Time Workshop**
2016 **Planetary Surface Processes Field School**
2013 **Sudbury Impact Crater Field School**

Memberships

American Geophysical Union, National Association of Geoscience Teachers, The Planetary Society